Institute of Thermoelectricity, Academy of Sciences and Ministry of Education and Science of Ukraine

Journal of THERMOELECTRICITY

International Research

Founded in December, 1993

published 6 times a year

No. 4 *2016*

Editorial Board

International Editorial Board

Founders – National Academy of Sciences, Ukraine
Institute of Thermoelectricity of National Academy of Sciences and Ministry of Education and Science of Ukraine

Certificate of state registration № КВ 15496-4068 ПР

Editorial office manager Ye. Bryzytska

Approved for printing by the Academic Council of Institute of Thermoelectricity of the National Academy of Sciences and Ministry of Education and Science, Ukraine

Address of editorial office:
Ukraine, 58002, Chernivtsi, General Post Office, P.O. Box 86.
Phone: +(380-372) 90 31 65.
Fax: +(380-3722) 4 19 17.
E-mail: jt@inst.cv.ua
http://www.jt.inst.cv.ua

Signed for publication 23.09.16. Format 70×108/16. Offset paper №1. Offset printing.
Printer's sheet 11.5. Publisher's signature 9.2. Circulation 400 copies. Order 5.

Printed from the layout original made by "Journal of Thermoelectricity" editorial board
in the printing house of "Bukrek" publishers,
10, Radischev Str., Chernivtsi, 58000, Ukraine

CONTENTS

Materials Research

G.P. Gaidar, P.I. Baranskii. Effect of thermal treatment on drag Seebeck coefficient anisotropy parameter of transmutation-doped silicon crystals 5

A. Nikolaeva, L. Konopko, T. Huber, P. Bodiul, I. Popov, E. Moloshnik, I. Gergishan. The impact of dimensions, magnetic field, elastic deformation on the thermoelectric figure of merit of the topological insulator wires based on semiconductor $Bi_{1-x}Sb_x$ wires 13

A.N. Doroshenko, E.I. Rogacheva, A.A. Drozdova, K.V. Martynova, Yu.V. Men'shov. Thermoelectric properties of polycrystalline $Bi_{1-x}Sb_x$ solid solutions in the concentration range $x = 0 – 0.25$ 23

F.F. Aliev, E.R. Yuzbashov, A.B. Maharramov, U.M. Agayeva, M.M. Zarbaliev, B.A. Veliyeva. Thermoelectric figure of merit of $TlIn_{1-x}Yb_xTe_2$ ($0 \le x \le 0.10$) 37

V.A. Romaka, L.P. Romaka, Yu.V. Stadnyk, V.Ya. Krayovskyy, V.V. Romaka, A.M. Horyn. Research on electrical conductivity mechanisms of thermoelectric material based on *n-ZrNiSn* doped with *Ga* 44

Technology

V.P. Shafranyuk. Study of damaged layer depth in thermoelectric materials by X-ray diffraction interferometry 59

Design

R.R. Kobylianskyi. Computer simulation of medical-purpose thermoelectric sensor readings 67

A.V. Prybyla. Thermoelectric conditioner with uniformly distributed modules for a human 75

Thermoelectric products

L.I. Anatychuk, V.Ya. Mykhailovsky, M.V. Maksimuk, I.S. Andrusiak. Experimental research on thermoelectric automobile starting pre-heater operated with diesel fuel 81

G.P. Gaidar[1], P.I. Baranskii[2]

[1]Institute for Nuclear Research, NAS Ukraine
47, Nauky Ave., Kyiv, 03680, Ukraine;
[2]V.E. Lashkaryov Institute of Semiconductor Physics,
NAS Ukraine 45, Nauky Ave., Kyiv, 03028, Ukraine

G.P. Gaidar *P.I. Baranskii*

EFFECT OF THERMAL TREATMENT ON DRAG SEEBECK COEFFICIENT ANISOTROPY PARAMETER OF TRANSMUTATION-DOPED SILICON CRYSTALS

It is shown that under the coincident (within the measurement errors) values of mobility anisotropy parameter $K = \mu_{\perp} / \mu_{\parallel}$ *the values of Seebeck coefficient anisotropy parameter* $M = \alpha_{\parallel}^{ph} / \alpha_{\perp}^{ph}$ *in transmutation-doped n-Si samples are much lower than in n-Si crystals doped with the same phosphorus impurity, but through the melt. It has been established that high-temperature annealing performed on transmutation-doped n-Si crystals at temperature* T_{anneal} *= 1200 ºC, irrespective of the annealing duration (in the range of 2 ÷ 72 h) leads to an increase in the value of parameter M, and this effect was more pronounced at quick cooling (at a rate of ~ 1000 °C/min) from* T_{anneal} *to room temperature.*

Key words: silicon, transmutation doping, thermal annealing, cooling rate, Seebeck coefficient anisotropy parameter.

Introduction

The electrophysical properties of transmutation-doped and conventional *n-Si* crystals, doped with phosphorous impurity through the melt (in the process of crystal growth by the Czochralski method), are compared in a number of works (see, for instance, [1 – 4]). Comparison of thermoelectric characteristics [5] of transmutation-doped and conventional silicon crystals was made in [6 – 9], where it is shown that with a higher homogeneity of impurity distribution in the bulk [10 – 12], as well as higher values of electron mobility measured at 77 K, the transmutation-doped *n-Si* crystals are characterized (all other factors being equal) by lower values of drag Seebeck coefficient anisotropy parameter $M = \alpha_{\parallel}^{ph}/\alpha_{\perp}^{ph}$ as compared to conventional crystals doped with phosphorous impurity through the melt. The latter is due to the fact that residual defects not eliminated from the bulk of transmutation-doped silicon crystals by standard process annealing (performed at 800 ÷ 850 ºC for 1 ÷ 2 h) and having no direct effect on the electron subsystem, introduce significant changes into effects occurring even in electron subsystem with participation of long-wave phonons. However, high-temperature annealing of transmutation-doped crystals can improve considerably their thermoelectric characteristics [8]. There is also a paper [13] where it is shown that thermal treatment of conventional *n-Si* crystals does not result in considerable change of their thermoelectric parameters.

To clarify the reasons for this difference, experiments were performed to study the influence of high-temperature annealing and cooling conditions on the thermoelectric properties of transmutation-doped silicon crystals, and that was the purpose of this work.

Results and discussion

Three types of annealing were used: process annealing (T = 800 °C, t = 2 h); high-temperature

A-type annealing (T_{anneal} = 1200 °C, t = 2 h); high-temperature *B*-type annealing (T_{anneal} = 1200 °C, t = 72 h); cooling rates after high-temperature annealing were υ_{cool} = 1 and 1000 °C/min. The object of study was conventional and transmutation-doped *n-Si* crystals. Conventional crystals were grown by the Czochralski method and were not subject to annealing (initial state). The *n-Si* crystals used later for transmutation doping were grown by zone melting technique. All transmutation-doped crystals (after silicon radiation with thermal neutrons) were first subject to process annealing at 800 °C for 2 hours (the state after such annealing will be considered to be initial for transmutation-doped crystals), and then – either to *A*-type or *B*-type annealing.

The basic parameters of samples under study are given in Table, where n_e and μ are charge carrier concentration and mobility, respectively, found from the Hall measurements; ρ_0 is electric resistivity in the absence of strong uniaxial mechanical stress X; ρ_∞ is resistivity at $X \geq 0.6$ GPa, $\vec{X} \parallel \vec{J} \parallel [001]$, $\vec{J}$ is current density when measuring tensoresistance (characteristic dependences ρ_X/ρ_0 are represented in Fig. 1); α_∞ and α_0 are tensothermopower ($\vec{X} \parallel \nabla T \parallel [001]$) at $X \geq 0.6$ GPa and $X = 0$, respectively (characteristic dependences α_X/α_0 are represented in Fig. 2); $\Delta\alpha = \alpha_{\parallel}^{ph} - \alpha_{\perp}^{ph}$ is thermopower anisotropy; α^e is electron (diffusion) component of thermopower calculated by the Pisarenko formula [14]:

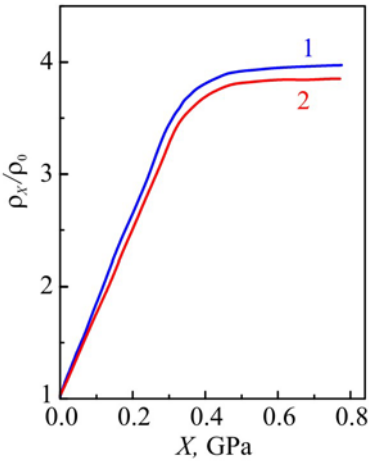

Fig. 1. Typical dependences of tensoresistance ρ_X/ρ_0 on the value of uniaxial mechanical stress $\vec{X}$ // $\vec{J}$ // [001] at T = 85 K for conventional (1) and transmutation-doped (2) n-Si crystals.

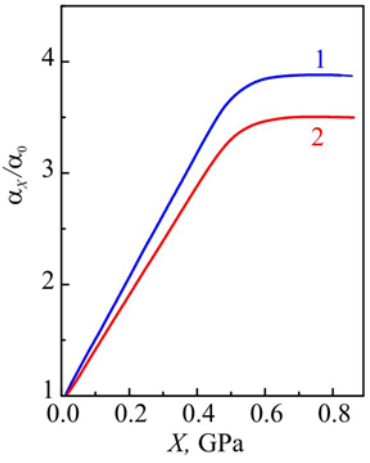

Fig. 2. Typical dependences of tensothermopower α_X/α_0 on the value of uniaxial mechanical stress $\vec{X}$ // ∇T // [001] at T = 85 K for conventional (1) and transmutation-doped (2) n-Si crystals.

Table

The basic parameters of n-Si samples under study

Conventional signs of Si samples; kind of thermal treatment	Symbols in the figures	υ_{cool}, °C/min	$n_e \cdot 10^{13}$, cm^{-3}	$\mu_{77K} \cdot 10^{-4}$, $cm^2/V\,s$	$\frac{\rho_\omega}{\rho_0}$	$\alpha_0 \cdot 10^{-3}$, $\frac{\mu V}{degree}$	$\alpha_\infty \cdot 10^{-4}$, $\frac{\mu V}{degree}$	$\alpha_\parallel^e$, $\frac{\mu V}{degree}$	$\alpha_\parallel^{ph} \cdot 10^{-4}$, $\frac{\mu V}{degree}$	$\alpha_\perp^{ph} \cdot 10^{-3}$, $\frac{\mu V}{degree}$	$\Delta\alpha \cdot 10^{-4}$, $\frac{\mu V}{degree}$	$K = \frac{\mu_\perp}{\mu_\parallel}$	$M = \frac{\alpha_\parallel^{ph}}{\alpha_\perp^{ph}}$
CONV	*a*	–	2.40	1.92	3.90	8.05	3.15	1220	3.03	4.70	2.56	5.35	6.45
CONV	*b*	–	5.50	1.90	3.82	7.90	3.03	1135	2.92	4.63	2.46	5.23	6.30
TD	1	–	2.90	2.22	3.86	8.00	2.85	1215	2.73	4.87	2.24	5.29	5.60
TD; 1200 °C, 2 h	1''	1000	2.40	2.00	3.87	10.2	4.90	1225	4.87	5.32	4.25	5.31	8.98
TD; 1200 °C, 2 h	1'	1	2.60	2.08	4.00	8.50	3.62	1217	3.51	4.84	3.03	5.50	7.20
TD	2	–	5.70	2.09	3.93	7.30	2.35	1132	2.24	4.66	1.77	5.40	4.90
TD; 1200 °C, 2 h	2'	1	5.50	2.14	3.95	8.40	3.57	1135	3.46	4.74	2.99	5.43	7.30
TD	3	–	5.73	2.14	3.84	7.50	2.66	1130	2.49	4.62	2.03	5.25	5.40
TD; 1200 °C, 2 h	3'	1	5.10	2.00	4.00	8.50	3.62	1140	3.51	4.84	3.03	5.50	7.20
TD	4	–	5.65	2.12	3.89	7.40	2.51	1131	2.36	4.64	1.90	5.33	5.40
TD; 1200 °C, 72 h	4''	1000	1.68	1.73	3.66	8.50	3.96	1230	3.84	4.14	3.43	5.00	9.30
TD; 1200 °C, 72 h	4'	1	3.00	2.08	3.54	8.50	3.50	1190	3.38	4.54	2.93	4.80	7.40

$$\alpha^e = \frac{k}{e}\left[2 + \ln\frac{2\left(2\pi m^* k T\right)^{3/2}}{n_0 h^3}\right], \quad (1)$$

where n_0 is charge carrier concentration; e is electron charge; k is the Boltzmann constant; T is temperature; h is the Planck constant; $m^* = N^{3/2}\sqrt[3]{m_{\parallel} m_{\perp}^2}$ is density-of-state effective mass; N is the number of isoenergetic ellipsoids; $m_{\parallel}$ and $m_{\perp}$ are effective masses of charge carriers lengthwise and crosswise the long axis of isoenergetic ellipsoid, respectively.

The value of mobility anisotropy parameter K is known to be experimentally obtained (see, for instance, [15]) from the data on tensoresistance with the use of relationship

$$K = \frac{\mu_{\perp}}{\mu_{\parallel}} = \frac{3}{2}\frac{\rho_{\infty}^{[001]}}{\rho_0} - \frac{1}{2}, \quad (2)$$

where $\mu_{\parallel}$ and $\mu_{\perp}$ are charge carrier mobilities lengthwise and crosswise the long axis of isoenergetic ellipsoid, respectively.

The phonon drag thermopower anisotropy parameter will be found through use of the following expression [8]:

$$M = \frac{\alpha_{\parallel}^{ph}}{\alpha_{\perp}^{ph}} = \frac{2K}{\left(2K+1\right)\dfrac{\alpha_0 - \alpha^e}{\alpha_{\infty} - \alpha^e} - 1} = \frac{2K}{\left(2K+1\right)\dfrac{\alpha_0^{ph}}{\alpha_{\infty}^{ph}} - 1}, \quad (3)$$

where $\alpha_{\parallel}^{ph}$ and $\alpha_{\perp}^{ph}$ are phonon components of thermopower lengthwise and crosswise the long axis of isoenergetic ellipsoid found from the formulae

$$\alpha_{\infty}^{ph} \equiv \alpha_{\infty} - \alpha^e = \alpha_{\parallel}^{ph}, \quad (4)$$

$$\alpha_0^{ph} = \alpha_0 - \alpha^e, \quad (5)$$

$$\alpha_{\perp}^{ph} = \alpha_{\parallel}^{ph} / M. \quad (6)$$

For the interpretation of the results we used the concentration dependence of drag thermopower anisotropy parameter M (Fig. 3, curve L), borrowed from [16].

Anisotropy parameters K and M, measured on silicon single crystals doped with phosphorous impurity by nuclear transmutation and in the process of growth by the Czochralski method were compared. It turned out that the values of drag thermopower anisotropy parameter M of crystals doped with phosphorous impurity through the melt (Fig. 3, dots *a* and *b*) obtained in this paper for comparison with transmutation-doped crystals of similar concentration exactly fall on curve L. And the values of parameter M for transmutation-doped crystals (with about the same carrier concentration n_e) are arranged much lower of this curve (Fig. 3, dots 1 – 4).

It can be assumed that substantial underrating of the values of parameter M for transmutation-doped crystals (as compared to standard curve obtained in the experiments with conventional crystals) is related to the emergence of lattice violations, i.e. residual defects. Such defects arise in huge concentrations in the process of transmutation doping and are not eliminated completely under conditions of relatively low-temperature (800 ^{o}C) process annealing of relatively short duration (2 h).

It should be noted that process annealing is a final and absolutely necessary stage of transmutation doping process. Silicon radiation with thermal neutrons is also accompanied by radiation with fast neutrons and γ - component of reactor spectrum. This results in silicon single

crystals saturated with all currently known radiation defects, which is promoted by extremely intensive integral neutron fluxes ($\sim 10^{18} \div 10^{19}$ n/cm^2) in nuclear reactor channels. Therefore, irrespective of the initial material type and its parameters, the as-irradiated transmutation-doped silicon is characterized by *p*-type conductivity with resistivity $\rho \approx 10^5 \div 10^6$ Ω·cm and very low lifetime of minor carriers. Moreover, after silicon irradiation with nuclear reactor neutrons the ^{31}Si atoms (which spontaneously go into ^{31}P according to nuclear reaction $^{30}Si\,(n,\gamma)\,^{31}Si \xrightarrow{\beta^-} {}^{31}P$) are as a rule found in the interstitial position. Such position corresponds to electrically inactive state. Therefore, for annealing of radiation defects and for activation of phosphorous atoms ^{31}P showing donor properties in the bulk of silicon only in lattice nodes, the transmutation-doped silicon must be subject to thermal treatment.

As shown by experiment, residual defects that were not eliminated during process annealing did not demonstrate marked influence on the electron subsystem of samples under study (mobility anisotropy parameter *K* remained practically unchanged), but changed essentially the effects occurring with participation of long-wave phonons.

Therefore, one could try to eliminate the underrating of parameter *M* values relative to standard curve *L* (Fig. 3) observed in the experiments with transmutation-doped silicon by annealing these crystals at higher temperatures than those (800 °C) used for process annealing. In all probability, annealing at higher temperatures will be able to transform, at least partially, the residual defects into such (point) defects on which phonons will be scattered less efficiently. Such process should have been accompanied by increase in parameter *M*, which was confirmed experimentally.

From Table it is seen that mobility anisotropy *K* is practically independent (within measurement error) of doping method or the employed thermal treatment modes, whereas drag Seebeck coefficient anisotropy parameter *M* is essentially responsive to annealing with subsequent cooling.

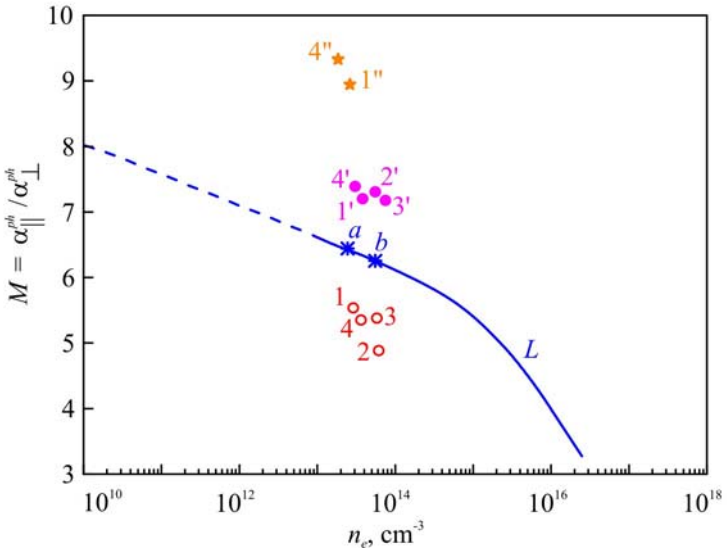

Fig. 3. Dependence of drag Seebeck coefficient anisotropy parameter $M = \alpha_{||}^{ph}/\alpha_{\perp}^{ph}$ on electron concentration n_e: 1) in conventional (doped with phosphorous impurity from the melt) n-Si crystals at T = 85 K: solid curve L; 2) in transmutation-doped crystals, subject to low-temperature process annealing at 800 ºC for 2 h: dots 1 – 4; 3) in transmutation-doped crystals, annealed at high temperature (1200 ºC) and cooled at different rates (1 and 1000 ºC/min): dots 1' – 4' and 1", 4", respectively.

In Fig. 3, dots 1' – 4' and 1", 4" represent the data of experiments (see also Table) performed on transmutation-doped crystals annealed at 1200 °C. The results (irrespective of annealing duration

in the range of $2 \div 72$ h) exceeded expectations, since the values of parameter M measured on annealed crystals not just "moved up" to position of curve L (as might be expected), but all without exception were well above this curve. In so doing, the values obtained with fast (υ_{cool} = 1000 °C/min) cooling of transmutation-doped crystals after annealing at 1200 °C proved to be so large (dots 1" and 4") that even with conditionally accepted linear change of function $M = M(n_e)$ (along a line segment in the form of strokes) they could be observed only at such values of $n_e \le 10^8$ cm^{-3} which in the framework of existing technology of fabrication (and doping) of conventional silicon crystals are certainly unattainable.

What critical weaknesses of the method for growing (and doping) conventional crystals prevent from obtaining on them so high values of thermopower anisotropy parameter (and other thermoelectric characteristics) which are relatively easily obtained at comparable n_e on transmutation-doped silicon crystals annealed at higher temperatures?

The reason is probably as follows. In transmutation-doped crystals, the values of parameter M are transferred from positions $1 - 4$ to positions $1' - 4'$ (and 1", 4") only due to high-temperature annealing, exempting the annealed crystal from the defects on which long-wave phonons are scattered that are responsible for the appearance of drag thermopower. Therefore, it is natural to believe that the process of conventional crystals growth and their doping with phosphorous impurity through the melt is accompanied by the emergence of stable and rather efficient scatterers for long-wave phonons in the form of impurity clusters which satisfy the condition $d_{clust} \sim \lambda_{ph}/4$, which inevitably complicates formation of drag thermopower in such crystals. Indeed, under conditions of growth (and doping) of conventional crystals the emergence of small-size impurity clusters [17] is promoted by high temperature $T_{cryst}^{Si} \approx 1400$ °C strongly violating mutual correlation of impurity centres [18]. At such temperature, impurity atoms are introduced into silicon lattice, whereas under conditions of neutron transmutation the atoms of doping impurity will only statistically uniformly appear in lattice nodes in the entire volume of irradiated crystal.

By the example of obtaining a material with high thermoelectric figures (M, $\Delta\alpha$, α_∞ and others; see Table) through high-temperature annealing of transmutation-doped silicon crystals one can make certain in the relative character of what is often called the quality of semiconductor material. Indeed, seeking to improve by this method the thermoelectric characteristics of transmutation-doped silicon crystals, we inevitably get in these crystals sufficiently low lifetime values of minor carriers τ (within several units or tens of microseconds). Resting upon low-temperature process annealing, i.e. showing proper care about lifetime, we, naturally, will not be able to obtain on the basis of transmutation-doped silicon crystals high-quality material designed for thermoelectric applications. Similar statements remain correct regarding other characteristics of semiconductor materials (such as the dislocation density, the content of related impurities, etc.).

For these reasons, the quality of semiconductor materials should be considered as intimately linked with the specific tasks that must be solved, using these or other materials, showing special care about parameters governing realization of functional capabilities of specific semiconductor instruments and devices.

Conclusions

1. It was discovered that for silicon samples doped with phosphorous by nuclear transmutation the thermopower anisotropy parameter is considerably lower than for the samples doped through the melt in the process of growth by the Czochralski method, with practically coincident values of

mobility anisotropy parameter K. It was concluded that these changes are caused by residual defects on which long-wave phonons are strongly scattered, producing no effect on electron subsystem.

2. It was established that high-temperature annealing ($T_{anneal} = 1200\ ^{o}C$; $t = 2 \div 72$ h) in transmutation-doped *n-Si* crystals increases Seebeck coefficient anisotropy parameter, this effect being more pronounced at quick cooling of samples. It was revealed that mobility anisotropy parameter K is practically independent either of doping method or of thermal treatment used.

References

1. G.P. Gaidar, *Kinetics of Electron Processes in Si and Ge in Externally Applied Fields. Monograph* (Saarbrücken, Deutschland: LAP LAMBERT Academic Publishing, 2015), 268 p.
2. P.I. Baranskii, A.A. Buhai, V.M. Maksimenko, V.V. Saviak, and V.P. Shapovalov, Effect of Thermal Treatment on EPR and Electric Activity of Phosphorous Impurity in Conventional and Neutron-Doped Silicon Crystals, *Semiconductors* **14**(7), 1438 – 1441 (1980).
3. A.P. Dolgolenko, P.G. Litovchenko, M.D. Varentsov, V.F. Lasovetsky, G.P. Haidar, and A.P. Litovchenko, Effect of Growth and Doping Methods on the Radiation Resistance of *n-Si* Radiated with Fast Reactor Neutrons, *Voprosy Atomnoi Nauki i Tekhniki. Ser: Physics of Radiation Damages and Radiation Materials Science* 4, 175 – 181 (2006).
4. G.P. Haidar, P.I. Baranskii, Peculiarities of Electrophysical Parameters of NTD-*Si* under Different Thermal Treatment Modes, *Semiconductors* **50**(6), 751 – 756(2016).
5. L.I. Anatychuk, *Thermoelements and Thermoelectric Devices. Reference Book* (Kyiv: Naukova Dumka, 1979), 767 p.
6. P.I. Baranskii, V.V. Saviak, and L.I. Shcherbina, Study of Phonon-Phonon Relaxation in Neutron-Doped and Ordinary Silicon Crystals, *Semiconductors* **14**(2), 302 – 305 (1980).
7. P.I. Baranskii, G.P. Haidar, Some Thermoelectric Peculiarities of Conventional and Transmutation-Doped Silicon Crystals, *J.Thermoelectricity* 1, 5 – 12 (2012).
8. G.P. Gaidar, P.I. Baranskii, Thermoelectric Properties of Transmutation-Doped Silicon Crystals, *Physica B* 441, 80 – 88 (2014).
9. G. Gaidar, P. Baranskii, Optimization of the Thermoelectric Figure of Merit in the Transmutation-Doped and Ordinary *n*-Si Crystals, *Phys. Status Solidi A* **212**(10), 2146 – 2153 (2015).
10. L.S. Smirnov, S.P. Solovyov, V.F. Stas', V.A. Kharchenko, Ed. by L.S.Smirnov, *Doping of Semiconductors by Nuclear Reactions Method. Monograph* (Novosibirsk: Nauka, 1981), 184 p
11. W.E.Haas, M.S. Schnöller, Silicon Doping by Nuclear Transmutation, *Journal of Electronic Materials* **5**(1), 57 – 68 (1976).
12. J. Miz, *Neutron Transmutation Doping Processes – a New Reactor Technology*. In: Neutron Transmutation Doping of Semiconductors. News of Solid State Physics. Issue 11. Ed. by J.Miz (Transl. from English. Ed. by V.N.Mordkovich) (Moscow: Mir, 1982).
13. P.I. Baranskii, Saviak, and Shapovalov, Influence of Thermal Annealing and Cooling Conditions on the Electrophysical Properties of *n-Si* with Phosphorous Impurity, *Semiconductors* **15**(8), 1531 – 1534 (1981).
14. V.L. Bonch-Bruevich, S.G. Kalashnikov, *Physics of Semiconductors* (Moscow: Nauka, 1977), 672 p.
15. P.I. Baranskii, A.V. Fedosov and G.P. Gaidar, *Physical Properties of Silicon and Germanium Crystals in the Fields of Effective External Influence* (Nadstyria, Lviv, 2000).

16. P.I. Baranskii, V.V. Savyak, L.A. Scherbina, Determination of Drag ThermoEMF Anisotropy Parameters in n-Silicon, *Semiconductors* **13** (6), 1219 – 1221 (1979).
17. S. Maekawa, N. Kinoshita, Electron Spin Resonance in Phosphorus Doped Silicon at Low Temperatures, *Journal of the Physical Society of Japan* **20**(8), 1447 – 1457 (1965).
18. I.V. Dakhovsky, T.A. Polianskaya, A.G. Samoilovich, and Yu.V. Shmartsev, On the Mobility of Electrons in Heavily Doped Semiconductors, *Semiconductors* **4**(11), 2165 – 2171 (1970).

Submitted 08.09.2016

A. Nikolaeva[1,2], L. Konopko[1,2], T. Huber[3], P. Bodiul[1,4], I. Popov[1], E. Moloshnik[1], I. Gergishan[1]

[1]D.Gitsu Institute of Electronic Engineering and Nanotechnologies
of the Academy of Sciences of Moldova, Academiei str., 3/3,
Kishinev, MD-2028, Republic of Moldova;
[2]International Laboratory of High Magnetic Fields and Low Temperatures,
ul. Gajowicka 95, Wroclaw, 53-421, Poland;
[3]Howard University, 500 College St. NW, Washington, USA
[4]Technical University of Moldova, 168, Stefan cel Mare blvd., Kishinev,
MD-2004, Republic of Moldova

THE IMPACT OF DIMENSIONS, MAGNETIC FIELD, ELASTIC DEFORMATION ON THE THERMOELECTRIC FIGURE OF MERIT OF THE TOPOLOGICAL INSULATOR WIRES BASED ON SEMICONDUCTOR $Bi_{1-x}Sb_x$ WIRES

This paper presents the experimental results of a study of thermoelectric properties of the topological insulator (TI) wires based on semiconductor $Bi_{1-x}Sb_x$ wires. Glass-coated semiconductor Bi-17 at % Sb wires prepared by the Ulitovsky liquid phase casting method were single crystals strictly of cylindrical shape with diameters ranging from 100 nm to 1000 nm and crystallographic orientation (1011) along the wire axis. It has been found that the energy gap ΔE_g in the Bi-17 at % Sb wires increases with decreasing wire diameter as 1/d, which is a manifestation of the quantum size effect. At low temperatures, a deviation from the exponential temperature dependence of the resistance $R \sim \exp(E/2k_BT)$ is observed; the conductivity of the wires increases with decreasing diameter which is most pronounced at T = 4.2 K due to the TI properties, in particular, the presence of surface states with high conductivity. The effect of temperature, magnetic field, elastic deformation, and the diameter of the Bi-17 at % Sb wires on power factor P.f. = $\alpha^2\sigma$ in the temperature range of 4.2 – 300 K has been studied. It has been shown that the maximum P.f. value is achieved at T = 300 K for wires with d = 100 nm and P.f. decreases with increasing diameter d. It has been found that both the magnetic field (H // I) and the elastic deformation of the wires lead to increase in the power factor by 35 – 40 % at T > 150 K; this finding opens up the possibility of optimizing the thermoelectric parameters of $Bi_{1-x}Sb_x$ TI based wires for use in thermoelectric energy converters.

Key words: thermoelectricity, semiconductor nanowires, topological insulator, quantum size effect, deformation.

Introduction

It is known that $Bi_{1-x}Sb_x$ alloys in the semiconductor concentration range for many years have been the best magnetothermoelectric material in the intrinsic region and have been widely used as *n*-legs in thermoelectric power converters at low temperatures ($40 < T < 150$ K) [1 – 6]. $Bi_{1-x}Sb_x$ ($0 \le x \le 1$) alloys form a continuous series of solid solutions. With a change in *Sb* concentration from 0 to 1, the energy spectrum of *Bi* is being constantly rearranged into *Sb* spectrum, forming in the concentration range ($0.08 < x < 0.25$) a semiconductor phase with maximum gap 25 meV (Fig. 1) [7].

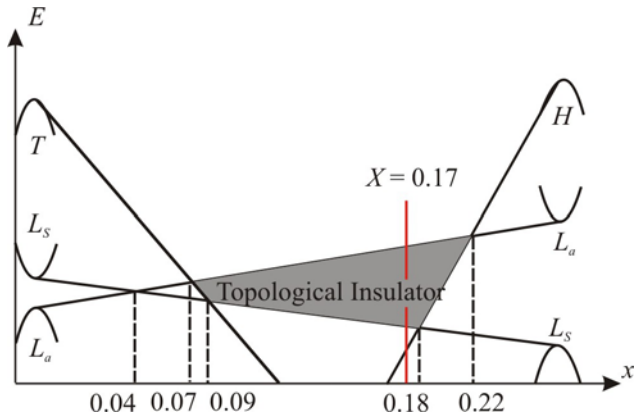

Fig. 1. Schematic of energy spectrum rearrangement in $Bi_{1-x}Sb_x$ alloys versus the concentration of Sb (0 < x < 0.25 Sb).

Optimization of thermoelectric materials includes three parameters - thermopower α (the Seebeck coefficient), electric conductivity of material σ and thermal conductivity $\chi = (\chi_e + \chi_p)$, where χ_e is electron thermal conductivity and χ_p is lattice thermal conductivity. The thermoelectric figure of merit $Z = \alpha^2\sigma/\chi_e + \chi_p$ [2].

Long-term manipulation of these parameters has not resulted in the improvement of thermoelectric figure of merit ($Z > 1$), the reasons for which have been considered in detail in papers and reviews [3 – 9].

A new impetus to development of thermoelectric materials was given by theoretical works of M.S. Dresselhaus with co-authors [10 – 13] dedicated to low-dimensional quantum systems (wires, films, quantum dots) based on *Bi* and $Bi_{1-x}Sb_x$ materials in which quantum size effects are most pronounced and in which considerable improvement of thermoelectric figure of merit *ZT* was predicted. It was shown that sample dimensions (thickness or diameter *d*) become an additional parameter affecting the thermoelectric figure of merit of material, when at least one of sample dimensions *d* is commensurate to the Broglie wavelength $\lambda = \frac{h}{p}$.

The reason for this is increase in the density of states of charge carriers $g(E)$ leading in quantum systems to increase of thermopower α, as well as decrease in thermal conductivity χ due to reduction of the mean free path of carriers and phonons because of additional scattering on the boundaries. Rapid development of nanotechnologies promoted experimental development of thermoelectric nanomaterials. However, experimental results obtained during recent 15 – 20 years are more modest than theoretical. Several papers [14, 15] reported on obtaining $ZT = 2$ at $T = 300$ K in Bi_2Te_3/Sb_2Te_3 superlattices and $ZT = 3$ at $T = 450$ K in quantum dot *PbTe/PbSeTe* superlattices. The thermoelectric achievements in low-dimensional semiconductors are most fully covered in the paper by J.P. Heremans [16]. A particularly complex issue is reproducibility of results and their real use in thermoelectricity.

In recent years much attention has been given to a new class of materials – topological insulators [17 – 19] which include $Bi_{1-x}Sb_x$ alloys in semiconductor region (Fig. 1). In [20] it was shown that the state of topological insulator is realized in semiconductors with inverted spectrum.

It was long believed that in the semimetal $Bi_{1-x}Sb_x$ alloys with $x < 0.04$ the energy spectrum at point *L* is inverted and in the alloys with $x > 0.04$ it is direct, since in the electron and hole spectrum at point *L* the ”saddle point” was not found. However, in 1998 the authors of [21] discovered the “saddle point” in the electron and hole spectra at point *L* of the Brillouin zone, at $x \approx 0.15$, so with increase in *k*,

the $E(k)$ relationship acquires a double-humped shape. Thus, the spectrum of *Bi* at point *L* is direct, and the spectrum of $Bi_{1-x}Sb_x$ ($0.04 < x < 1$) alloys is inverted, and so in these alloys in semiconductor region one should expect manifestation of TI properties, particularly in low-dimensional systems. Semiconductor $Bi_{1-x}Sb_x$ alloys were the first open thee-dimensional TI with five intersected Fermi levels of surface band [22, 23]. Studies by means of angle-resolved photoemission spectroscopy (ARPES) have proved the existence of surface states in the semiconductor $Bi_{1-x}Sb_x$ alloys with the dispersion law which enables one to refer these alloys to the class of topological insulators [24].

High carrier mobilities from the surface states were found in $Bi_{0.9}Sb_{0.1}$ TI [25]. Thermoelectric figure of merit improvement in topological insulators was predicted in [14, 19, 26].

To understand macroscopic properties of TI surface state and study the opportunities of their practical use, it is necessary to perform transport studies. The purpose of the present paper was to study manifestation of TI properties and to investigate the thermoelectric properties of *Bi*-17 at % *Sb* TI wires depending on diameter, temperature, magnetic field and elastic deformation.

Samples and experimental procedure

Thin single crystal wires were prepared by the Ulitovsky liquid phase casting method [27, 28]. Single crystal *Bi*-17 at % *Sb* ingot, prepared by zone recrystallization method, was used as the initial material.

Crystallization of microwire core of bismuth and $Bi_{1-x}Sb_x$ alloys proceeds with strong overcooling of melt at the crystallization front. For bismuth, ultimate overcooling depth occurs at casting rate 10 m/s and reaches 40 – 50 °C. Strong overcooling and high crystallization rates contribute to growth of single crystal core and retention of stoichiometric composition of *Bi*-17 at % *Sb* alloy.

Wire diameter was measured by optical microscope Biolam with magnification 1350. Test diameter measurements were made on scanning electron microscope (SEM) Vega Tescan 5130 MM.

Monocrystallicity of *Bi*-17 at % *Sb* wires and their crystallographic orientation was established by means of rotation X-ray diagrams. Samples of all diameters had orientation (1011) along the wire axis. In so doing, like in the wires of pure *Bi* [29], the trigonal C_3 axis is inclined to the wire axis at an angle of ~ 20º, and the C_3 axis is normal to that axis.

Glass-coated wires were arranged on a plate of copper-clad paper-based laminate with the cut-out copper contact stripes onto which *InGa* eutectics was deposited which at 300 K was in liquid state. A contact was created due to wetting of *InGa* wire ends with eutectics, to provide contact ohmicity. The length of the sample was 1 ÷ 3 mm. The plate with the wire was placed into a special holder which was immersed into cryostat for low-temperature measurements. A differential thermocouple *Cu*-*Cu*(0.05 *Fe*) having thermal contact with the cold and heated wire ends was used for measuring temperature difference on sample ends. Temperature gradient was created from 0.5 K to 2 K depending on the measurement temperature.

The resistance was measured by two-contact method with the error not more than 1 %, and total error of thermopower measurement was ~ 10 %.

The arrangement of principal crystallographic axes and monocrystallicity of the wires of all diameters have been confirmed by investigation of angle rotation diagrams of transverse magnetoresistance $R(\theta)$ ($H \perp I$) in various magnetic fields (0.5 ÷ 14 T) at T = 300 K, 150 K, 80 K, 4.2 K.

Example of recording angle rotation diagrams $\Delta R/R(\theta)$ of *Bi*-17 at % *Sb* wire with d = 200 nm at 150 K and different values of magnetic field H is represented in Fig. 2.

Angular dependences of transverse magnetoresistance are symmetrical with respect to direction $\theta = 0$ and $\theta = 90^0$, which fully corresponds to phenomenological expressions [30]. It should be noted that unlike rotation diagrams of transverse magnetoresistance, on the wires and single crystals of *Bi* and semi-metal $Bi_{1-x}Sb_x$ alloys in high magnetic fields minimum is formed at $H \parallel C_3$, and maximum – at $H \parallel C_2$.

This data is in good agreement with the results of [24] obtained on the bulk single crystals of corresponding composition and orientation.

Deformation dependences of resistance $R(\xi)$ and thermopower $\alpha(\xi)$, where $\xi = l - l_0/l_0$, l_0 is sample length without tensile load were measured to 1.5 – 2 % of relative elongation, as described in [31, 32]. Particular attention was focused on deformation elasticity condition which was estimated by the reproducibility of results at numerous stretching cycles for each temperature.

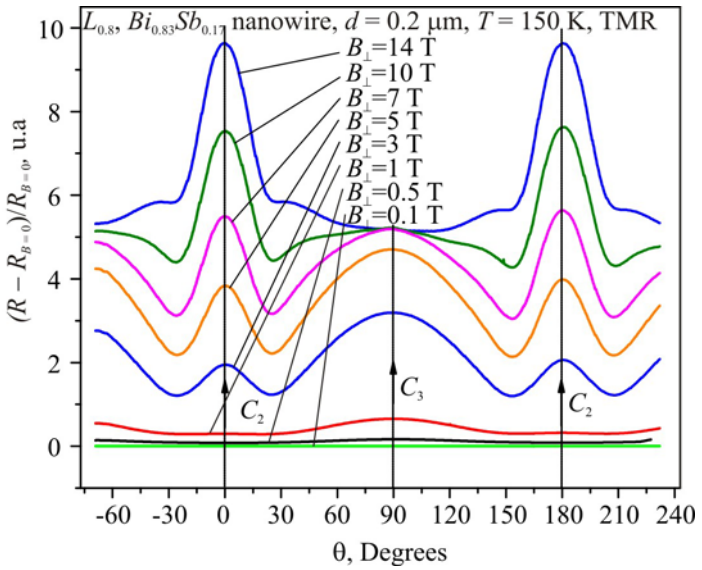

Fig. 2. Transverse magnetoresistance rotation diagrams of Bi-17 at % Sb wire, T = 150 K, d = 200 nm, for different magnetic field values.

Measurements in a magnetic field were performed in a longitudinal configuration $H \parallel I$, $H \parallel \Delta T$) in the region of magnetic fields up to 14 T in the Bitter-magnet field at temperatures 2 – 300 K in the International Laboratory of High Magnetic Fields and Low Temperatures (Wroclaw, Poland).

Discussion of the results

Fig. 3 shows temperature dependences of relative resistance $\Delta R/R(T)$, where $\Delta R = R_T - R_{300}$, for semiconductor *Bi*-17 at % *Sb* wires of different diameters, in the temperature range of 1.5 – 300 K. At 300 K relative resistance ρ is practically independent of wire diameter *d*. With decrease in temperature, resistance grows for the wires of all diameters under study, and exponential areas, $R \sim \exp(\Delta E/2k_BT)$, appear on the $R(T)$ dependences.

The slope of exponential areas and the area of their existence depend on the wire diameter *d*. With decreasing wire diameter *d*, the area of linear dependence $\rho(10^3/T)$ is displaced toward higher temperatures (Fig. 3, inset). From the linear dependences $\rho(10^3/T)$ it follows that thermal gap essentially depends on the wire diameter *d*, increasing from the value 20 – 22 meV, for the wire with d = 1100 nm, typical for the bulk samples of similar composition, to the value ΔE = 42 meV for the wire with d = 100 nm.

Such dependence on the wire diameter d is a manifestation of quantum size effect leading to semimetal-semiconductor transition in semimetal wires of pure Bi and $Bi_{1-x}Sb_x$ ($x < 0.04$), and in semiconductor $Bi_{1-x}Sb_x$ wires [33, 34] – to gap increase with decreasing wire diameter d [12, 27, 28, 33, 34].

It should be noted that in $Bi_{1-x}Sb_x$ alloys c $0.15 < x < 0.22$ the thermal gap found from the experimental dependences of resistivity on temperature, is indirect gap ΔE_{LH}, equal to the distance between the bottom of conduction band and the ceiling of valence band in H (Fig. 1). However, in the general case from the $\rho(T)$ dependences of semiconductor $Bi_{1-x}Sb_x$ alloys the "effective" thermal gap ΔE_T is determined which is observed as a result of thermal generation of carriers both through ΔEg_L gap and through ΔE_{LT} or ΔE_{LH}. According to Fig. 3 (inset below) the energy gap exponentially grows with decreasing diameter $\Delta E \sim \exp(d)$.

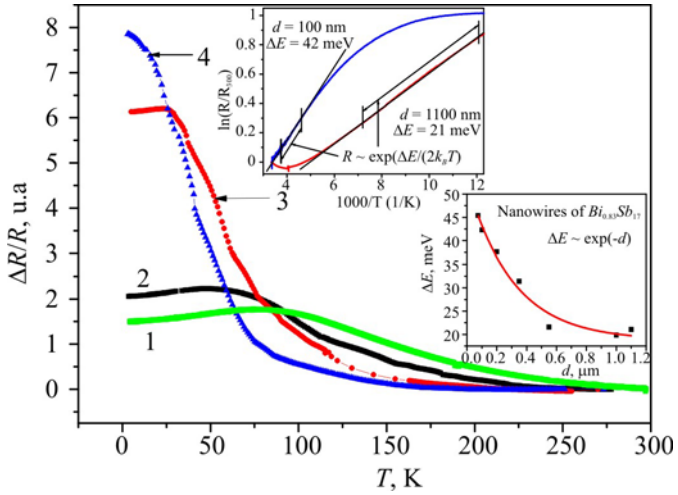

Fig. 3. Temperature dependences of reduced resistance ΔR/R(T) in the Bi-17 % Sb wires of different diameters: 1. d = 100 nm, 2. d = 200 nm, 3. d = 600 nm, 4. d = 900 nm. On the inset above: $R(10^3/T)$ dependences for the wires with d = 200 nm and d = 1100 nm; below - dependences of ΔEg gap on the wire diameter d.

In low-temperature region $T < 100$ K there is major change in the temperature dependences $R(T)$ (Fig. 3) with decreasing wire diameter d. There was a deviation from the exponential growth of $R(T)$ with decrease in temperature and plateau formation at $T \to 4.2$ K. The temperature whereby this deviation occurs is displaced toward higher temperatures with decreasing wire diameter d. In fact, at 4.2 K there is an increase in the conductivity of semiconductor Bi-17 at % Sb wires by a factor of ≈ 5, with increasing diameter from 1000 nm to 100 nm (Fig. 3).

Such $R(T)$ behaviour in low-temperature region can be explained from the standpoint of manifestation of TI properties, namely the emergence of high-conductivity surface states the contribution of which increases with decreasing wire diameter and the resistance drops. In TI, conductive surface properties result from strong spin-orbit interaction which leads to the emergence of spin-split topological surface states with the Dirac type of dispersion, i.e. linear dependence of energy on pulse [35].

There were also investigated temperature dependences of thermopower $\alpha(T)$ in the temperature range of 4.2 – 300 K for the wires of different diameters (Fig. 4).

For the wires of all investigated diameters the thermopower is negative in the entire temperature range. With decreasing temperature, the thermopower increases in the absolute value

reaching -150 μV/K in the region of 30 – 50 K. With decrease in temperature to 4.2 K, the thermopower decreased to -20 μV/K for the wires of all investigated diameters.

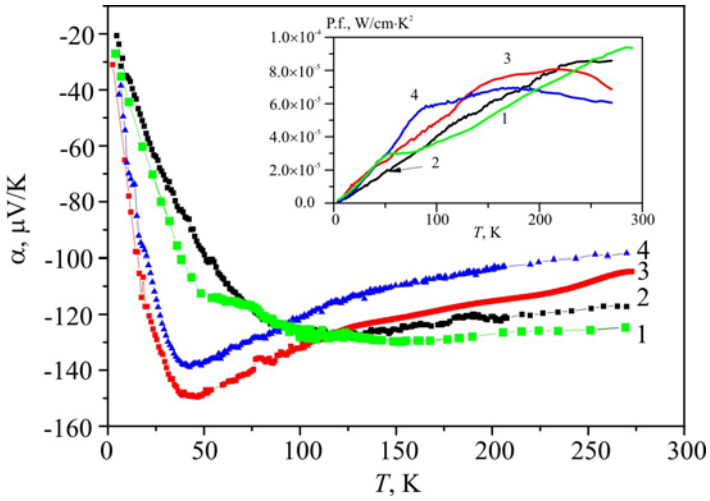

Fig. 4. Temperature dependences of thermopower α(T) of $Bi_{1-x}Sb_x$ wires of different diameters: 1. d = 100 nm, 2. d = 200 nm, 3. d = 600 nm, 4. d = 900 nm. In the inset: temperature dependences of power factor P.f. = $\alpha^2\sigma(T)$.

With decreasing wire diameter, maximum thermopower value is reduced and the peak is displaced toward higher temperatures. Thermopower decrease in the thin wires of semiconductor $Bi_{1-x}Sb_x$ alloys is due to the effect of surface scattering on the mean free path of electrons determining at $T < 100$ K the sign and value of thermopower. The drop in the effective mean free path of electrons with decreasing wire diameter results in the reduction of their contribution to thermopower, which is the consequence of classical size effect manifestation.

Dependences of power parameter P.f. = $\alpha^2\sigma$ on the temperature and wire diameter d were determined according to thermopower $\alpha(T)$ and resistance $R(T)$ data and represented in the inset of Fig. 4. Maximum value P.f. = 8 10^{-5} W/cm K^2 is achieved at 300 K in the wires with the minimum diameter d = 100 nm (Fig. 4, curve 1).

The effect of magnetic field $H \parallel I$, $\|\Delta T$ and elastic tensile deformation on the thermoelectric figure of merit of the *Bi*-17 at % *Sb* wires was investigated at different temperatures.

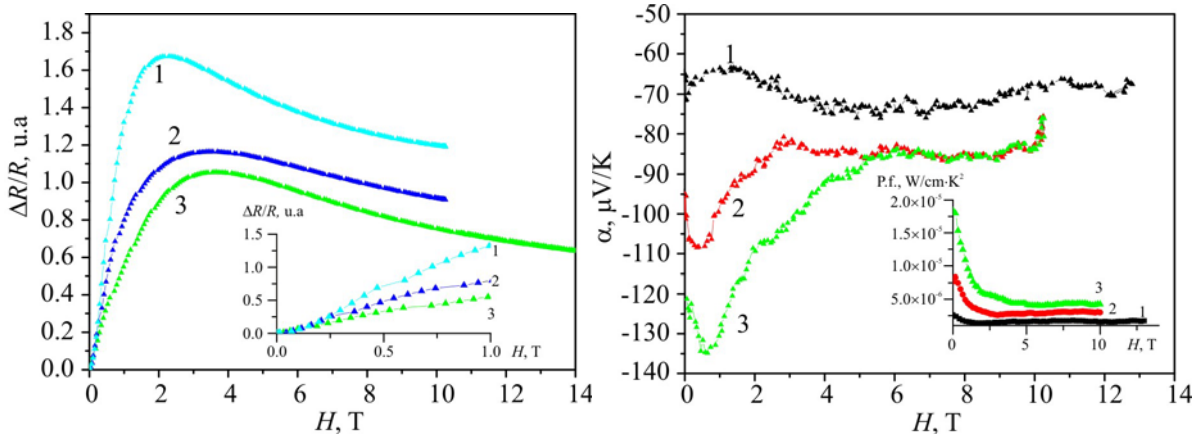

a) *b*)

Fig. 5. Field dependences of relative resistance ΔR/R(H) (a) and thermopower α(H) (b) of Bi – 17% Sb wire, d = 200 nm at different temperatures: 1. T = 17 K, 2. T = 38 K, 3. T = 64 K. In the inset (a) initial sections (up to 1 T) of the field dependences of ΔR/R(H). In the inset (b): field dependence of power factor P.f.(H), at different temperatures: 1. T = 17 K, 2. T = 38 K, 3. T = 64 K.

Fig. 5 and 6 represent the magnetic field dependences of resistance (*a*) $\Delta R/R(H)$ ($H \parallel I$) and thermopower (*b*) $\alpha(H)$ ($H \parallel \Delta T$) at fixed temperature values of the *Bi*-17 at % *Sb* wires, $d = 200$ nm (Fig. 5) and $d = 100$ nm (Fig. 6).

With increasing magnetic field, the resistance grows at all temperatures, however, in weak magnetic fields with a rise in temperature resistance growth is decelerated (insets in Fig. 5*a* and Fig. 6*a*), whereas increase in thermopower $\alpha(H)$ is enhanced (Fig. 5*b*, 6*b*).

In the *Bi*-17 at % *Sb* wires with $d = 200$ nm resistance growth versus magnetic field ($H = 2$ T) is 80 % at $T = 64$ K, and in the wires with $d = 100$ nm resistance increases by 18 % at $T = 52$ K. Weak thermopower increase in magnetic fields up to 2 *T* leads to reduction of power factor in the wires with $d = 200$ nm (curve 3 in the inset of Fig. 5*b*) and stabilization of P.f. for the wires with $d = 100$ nm (curve 2 Fig. 7*a*).

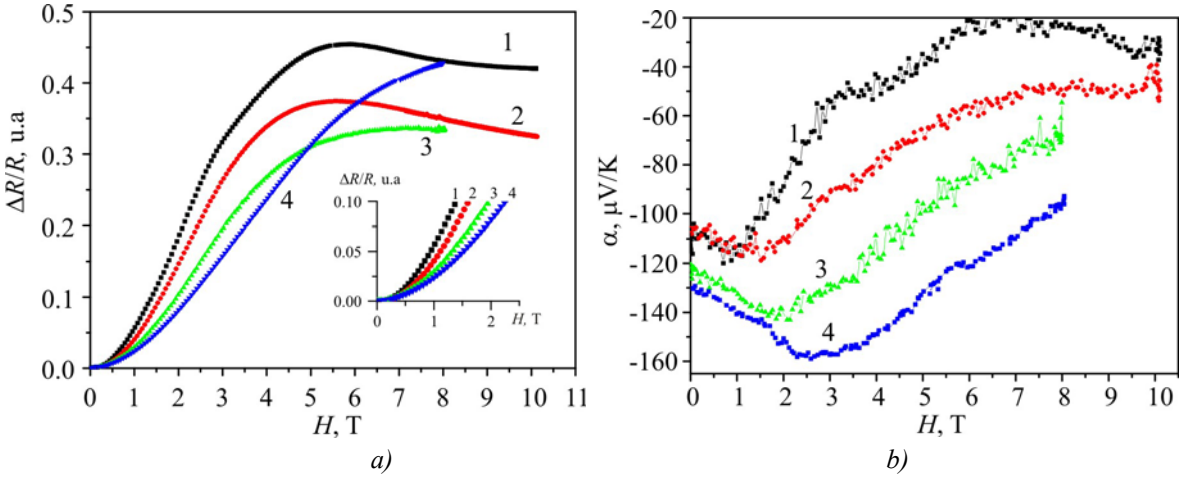

Fig. 6. Field dependences of relative resistance ΔR/R(H) (a) and thermopower α(H) (b) of the Bi-17 at % Sb wire, d = 100 nm, at different temperatures: 1. T = 7 K, 2. T = 52 K, 3. T = 100 K, 4. T = 145 K. In the inset (a) the initial sections of the field dependences of ΔR/R(H).

At higher temperatures the situation is different. As is seen from Fig. 6*b*, at $T = 143$ K for the wires with $d = 100$ nm, the thermopower increases in magnetic fields 2.5 *T* by ~ 20 % (curve 4), whereas the resistance increases by ~ 10 % under the same conditions. The calculated value of power factor P.f. = $\alpha^2\sigma$ versus a magnetic field points to P.f. increase by ~ 40 % in a magnetic field 2.5 *T* (Fig. 7*a*, curve 4).

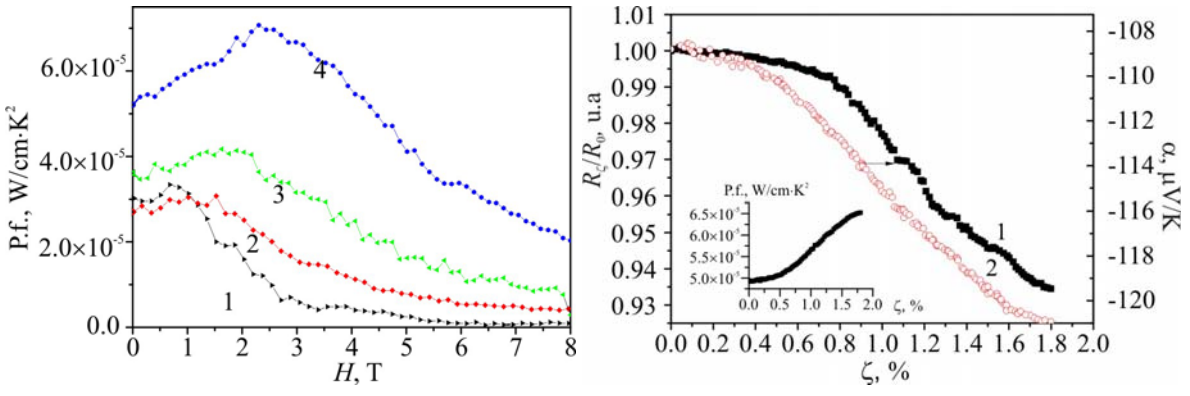

Fig. 7. (a) Field dependences of power factor P.f. of the Bi-17 at % Sb wire, d = 100 nm, at different temperatures: 1. T = 7 K, 2. T = 52 K, 3. T = 100 K, 4. T = 145 K. (b) Deformation dependences of relative resistance $R_\xi/R_0(H)$ - curve 1, and thermopower $\alpha(\xi)$ - curve 2, the Bi-17 at % Sb wires, d = 100 nm at T = 146 K. Inset: deformation dependence of power factor P.f. (ξ).

There were also investigated deformation dependences (tensile deformation) of resistance $R(\xi)$ and thermopower $\alpha(\xi)$ at different temperatures. Fig. 7*b* shows deformation dependences of resistance $R_\xi/R_0(H)$ -1 and thermopower $\alpha(\xi)$ – 2 at $T = 146$ K, ($\xi = l\text{-}l_0/l_0$, where l_0 is wire tension length).

As can be seen from Fig. 7*b*, elastic tensile deformation of thin wires ($d = 100$ nm) to 1.8 % of relative elongation leads to resistance decrease and increase of thermopower absolute value, which results in P.f. increase by ~ 30 % at 146 K.

Thus, magnetic field and elastic deformation lead to an increase in thermoelectric figure of merit of the semiconductor *Bi*-17 % *Sb* wires with $d = 100$ nm, which opens up the possibility of purposeful control over thermoelectric parameters of nanowires based on the semiconductor $Bi_{1-x}Sb_x$ alloys. It is interesting to study the thermoelectric figure of merit with a simultaneous impact of a weak magnetic field and deformation in high-temperature region 200 – 300 K.

Conclusions

Studies of magnetothermoelectric properties of single-crystal *Bi*-17 at % *Sb* TI wires with diameters from 100 nm to 1000 nm have shown that, on the one hand, manifestation of quantum size effect leads to increase in the energy gap *Eg* with decreasing wire diameter: $\Delta Eg \sim 1/d$, and, on the other hand, manifestation of TI properties in low-temperature region (4.2 K) leads to increase in conductivity σ with decreasing wire diameter due to formation of high-conductivity surface states of TI.

It was established that both a weak magnetic field and elastic tensile deformation lead to power factor increase by $\approx$ 30 – 40 % in the wires with a minimum diameter 100 nm at temperatures $\geq$ 140 K.

Decreasing diameter d of the wires and study of their thermoelectric parameters at $T > 150$ K with a simultaneous impact of deformation and magnetic field will enable one to optimize magnetothermoelectric parameters of $Bi_{1-x}Sb_x$ wires for their use in thermoelectric power converters.

This work was performed with support of STCU grant # 5986.

References

1. A.F. Ioffe, *Physics of Semiconductors* (Academic Press Inc, New York, 1960), 178 – 179p.
2. H.J. Goldsmid, *Applications of Thermoelectricity* (London: Methuen & Co. Ltd., 1960).
3. W.M. Yim, A. Amith, Alloys for Magneto-Thermoelectric and Thermomagnetic Cooling. *Solid-State Electronics* **15**(10), 1141 – 1165 (1972).
4. G.A. Ivanov, V.A. Kulikova, V.L. Naletov, A.F. Panarin, and A.R. Regel, Thermoelectric Figure of Merit of Pure and Doped Bismuth-Antimony Alloys in a Magnetic Field, *Semiconductors* **6**(7), 1296 – 1299 (1972).
5. L.I. Anatychuk, *Thermoelements and Thermoelectric Devices: Reference Book* (Kyiv: Naukova Dumka, 1979), 768 p.
6. N.A. Rodionov, G.A. Ivanov, and N.A. Redko, Thermoelectric Figure of Merit of *p*-type $Bi_{1-x}Sb_x$ ($0.12 < x < 0.14$) Alloys at Low Temperatures, *Physics of the Solid State* **24**(6), 1881 – 1884 (1982).
7. S. Golin, Band Model for Bismuth-Antimony Alloys, *Phys. Rev*. **176** (3), 830 (1968).
8. B. Lenoir, M. Cassart, J.-P. Michenaud, H. Scherrer, and S. Scherrer, Transport Properties of *Bi*-rich *Bi-Sb* Alloys, *J.Physics and Chemistry of Solids* **57** (1), 89 – 99 (1998).

9. B. Lenoir, A. Dauscher, M. Cassat, Yu. Ravich, and H. Sherrer, Effect of Antimony Content on the Thermoelectric Figure of Merit of $Bi_{1-x}Sb_x$ Alloys, *J. Phys. Chem. Sol*. 59, 129 (1998).
10. L.D. Hicks, M.S. Dresselhaus, Effect of Quantum-Well Structures on the Thermoelectric Figure of Merit, *Phys. Rev. B* 47, 12727-31 (1993).
11. O. Rabin, Y.-M. Lin, and. M. Dresselhaus, Anomalously High Thermoelectric Figure of Merit in $Bi_{1-x}Sb_x$ Nanowires by Carrier Pocket Alignment, *Appl. Phys. Lett.* **79**(1), 81 – 83 (2001).
12. J. Heremans, C.M. Thrush, Yu-Ming Lin, S. Cronin, Z. Zhang, M.S. Dresselhaus, and J.F. Mansfield, Bismuth Nanowire Arrays: Synthesis and Galvanomagnetic Properties, *Phys. Rev. B* 61, 2921 (2000).
13. Shuang Tang and Mildred S. Dresselhaus, Electronic Phases, Band Gaps, and Band Overlaps of Bismuth Antimony Nanowires, *Phys. Rev. B* 89, 045424 (2014).
14. R. Venkatasubramanian, E. Siivola, T. Colpitts, and B. O'Quinn, Thin-Film Thermoelectric Devices with High Room-Temperature Figures of Merit, *Nature* **413**(6856), 597 – 602 (2001).
15. T.C. Harman, P.J. Taylor, M.P. Walsh, and B.E. LaForge, Quantum Dot Superlattice Thermoelectric Materials and Devices, *Science* **297**(5590), 2229-32 (2002).
16. J.P.Heremans, Low-Dimensional Thermoelectricity, *Acta Physica Polonica A* **108**(4), 609 – 634 (2005).
17. Liang Fu, C.L. Kane, and E.J. Mele, Topological Insulators in Three Dimensions, *Phys. Rev. Let.* 98, 106803 (2007).
18. A.A. Taskin, Kouji Segawa, and Yoichi Ando, Oscillatory Angular Dependence of the Magnetoresistance in a Topological Insulator $Bi_{1-x}Sb_x$, *Phys. Rev. B* 82, 121302(R) (2010).
19. Ryuji Takahashi and Shuichi Murakami, Thermoelectric Transport in Topological Insulators, *Semiconductor Science and Technology* **27**(12), 124500 (2012).
20. Liang Fu, C.L. Kane, Topological Insulators with Inversion Symmetry, *Phys. Rev. B* 76, 045302 (2007).
21. N.B. Brandt, G.I. Golysheva, Nguyen Minh Thu, M.V. Sudakova, and Ya.G. Ponomarev, Origination of Saddle Point in the Energy Spectrum $Bi_{1-x}Sb_x$ Alloys at Inversion of Bands with a Change in Composition *x*, *Low Temperature Physics* **13**(11), 1209 – 1212 (1987).
22. D. Hsieh et al., Observation of Unconventional Quantum Spin Textures in Topological Insulators, *Science* 323(5916), 919 – 922 (2009).
23. Akinori Nishide, Alexey A. Taskin, et al. Direct Mapping of the Spin-Filtered Surface Bands of a Three-Dimensional Quantum Spin Hall Insulator, *Phys. Rev. B* 81, 041309(R) (2010).
24. D. Hsieh, D. Qian, L. Wray, Y. Xia, Y.S. Hor, R.J. Cava, and M.Z. Hasan, A Topological Dirac Insulator in a Quantum Spin Hall Phase, *Nature* **452**(7190), 970 – 974 (2008).
25. Dong-Xia Qu, Sarah K. Roberts, and George F. Chapline, Observation of Huge Surface Hole Mobility in the Topological Insulator $Bi_{0.91}Sb_{0.09}$ (111), *Phys. Rev. Lett*. 111, 176801 (2013).
26. T.H. Wang, H.T. Jeng, Enhanced Thermoelectric Performance in Thin Films of Three-Dimensional Topological Insulators, *arXiv:1608.00348* [cond-mat.mes-hall], 2016.
27. A. Nikolaeva, T.E. Huber, D. Gitsu, and L. Konopko, Diameter Dependent Thermopower of Bismuth Nanowires, *Phys. Rev. B* 77, 035422 (2008).
28. Albina A. Nikolaeva, Leonid A. Konopko, Tito E. Huber, Pavel P.Bodiul, and Ivan A.Popov, Prospects of Nanostructures $Bi_{1-x}Sb_x$ for Thermoelectricity, *J.Solid State Chemistry* 193, 71 – 75 (2012).
29. N.B. Brandt, D.V. Gitsu, A.A. Nikolaeva, and Ya.G. Ponomarev, Investigation of Size Effects in Thin Cylindrical Bismuth Single Crystals in a Magnetic Field, *Sov. Phys. JETP* **45**(6) 1226 (1977).

30. D.V. Gitsu, I.M. Golban, V.G. Kantser, and F.M. Muntiany, *Transport Phenomena in Bismuth and its Alloys* (Kishinev: Stiinţa, 1983), 266 p.
31. A. Nikolaeva, T. Huber, L. Konopko, and A. Tsurkan, Observation of the Semiconductor-Semimetal and Semimetal-Semiconductor Transitions in *Bi* QuantumWires Induced by Anisotropic Deformation and Magnetic Field, *Low Temp Phys* 158, 530 – 535 (2010).
32. D. Gitsu, L. Konopko, A. Nikolaeva, and T. Huber, Pressure Dependent Thermopower of Individual *Bi* Nanowires, *J. Applied Physics Letters* 86, 10210 (2005).
33. T.W. Cornelius, M.E. Toimil-Molares, R. Neumann, G. Fahsold, R. Lovrincic, A. Pucci, and S. Karim, Quantum Size Effects Manifest in Infrared Spectra of Single Bismuth Nanowires, *Appl. Phys. Lett.* 88, 103114 (2006).
34. Jane E. Cornett and Oded Rabin, Thermoelectric Figure of Merit Calculations for Semiconducting Nanowires, *Appl. Phys. Lett*. 98, 182104 (2011).
35. Shuang Tang and Mildred S.Dresselhaus, Constructing Anisotropic Single-Dirac-Cones in $Bi_{1-x}Sb_x$ Thin Films, *Nano Lett.* **12**(4), 2021 – 2026 (2012).

Submitted 10.08.2016

A.N. Doroshenko, E.I. Rogacheva, A.A. Drozdova,
K.V. Martynova, Yu.V. Men'shov

National Technical University "Kharkiv Polytechnic Institute",
21 Frunze str, Kharkiv 61002, Ukraine

THERMOELECTRIC PROPERTIES OF POLYCRYSTALLINE $Bi_{1-x}Sb_x$ SOLID SOLUTIONS IN THE CONCENTRATION RANGE $x = 0 – 0.25$

A detailed investigation of the dependence of thermoelectric properties of polycrystalline $Bi_{1-x}Sb_x$ solid solutions on composition in a wide concentration range ($x = 0 – 0.25$) was performed at room temperature. The objects of study were cast samples of various composition obtained by ampoule method in one technological cycle consisting in cooling of ampoules with melts in the air and subsequent long homogenizing annealing at temperature (520 ± 5) K for 720 hours. It was shown that the composition dependences of properties are of clearly expressed non-monotonic type. The presence of concentration anomalies of thermoelectric properties was confirmed that had been earlier observed in the range $x = 0 – 0.1$ on cast samples after different kinds of thermal treatment and interpreted as manifestation of electron phase transitions. A complicated nature of dependences at $x > 0.1$ is attributable to qualitative changes in $Bi_{1-x}Sb_x$ band structure at certain critical compositions, a change in relative contribution to conductivity of charge carriers from different energy bands with a change in antimony concentration and high sensitivity of energy spectrum and physical properties of $Bi_{1-x}Sb_x$ κ to external effects.

Key words: bismuth-antimony solid solution, composition, thermoelectric properties, electronic transition, critical phenomena.

Introduction

Solid solutions formed by *Bi* and *Sb* semimetals are known as the best thermoelectric (TE) materials of *n*-type and promising thermomagnetic materials for temperatures below ~ 150 K [1 – 4]. Only in these materials the highest values of TE figure of merit $Z = (S^2 \sigma) / \lambda$ are achieved, where S is the Seebeck coefficient, σ is electric conductivity and λ is thermal conductivity ($Z = (6 \div 7) \cdot 10^{-3}$ K^{-1}). Recently there has been a surge of interest in studying the properties of $Bi_{1-x}Sb_x$ crystals and thin films due to observation in $Bi_{1-x}Sb_x$ of peculiar properties typic al of 3D-topological insulators [5, 6] and suggested proposals on the possibility of using these properties when creating high-performance TE materials [7].

Possessing close values of atomic radii, crystalline structures and electronic configurations of the same type, *Bi* and *Sb* semimetals form a continuous series of solid solutions whose band structure with a change of composition is varied in a complicated way [1 – 4, 8]. Fig. 1 schematically represents the accepted structure of energy bands of $Bi_{1-x}Sb_x$ solid solutions at 0 K. In pure *Bi* there is a band of "light" (L_a) and "heavy" (T) holes, and as a result of overlapping the hole T and electron L_s bands, bismuth demonstrates semimetal properties. Similar band structure is inherent in antimony where the band of "heavy" holes H and electron band L_a overlap. Adding of antimony to bismuth causes approach of bands L_s and L_a, at $x = 0.03 \div 0.04$ the energy gap between them E_g vanishes, the gapless state is realized, the bands L_s and L_a are inverted, and with a further increase of x the gap between them again increases. Simultaneously with increase in *Sb* concentration, the top of valence

band T shifts down the energy with respect to the bottom of conduction band L_s, leading to reduced overlapping of T and L_s bands, and with concentration $x = 0.06 \div 0.07$ the overlapping of bands disappears and semimetal-indirect-gap semiconductor transition takes place whose energy gap is determined by the position of T and L_a bands. As long as with further increase of x the top of T bands continues shifting down the energy, at $x = 0.08 \div 0.09$ the tops of T and L_s valence bands coincide and in the concentration range $x \cong 0.09 – 0.15$ the energy gap is determined by the distance between bands L_s and L_a i.e. it becomes a direct-gap semiconductor. At $x = 0.15 \div 0.17$ the tops of bands L_s and H coincide, and with subsequent growth of Sb concentration (up to $x \sim 0.22$) the energy gap is determined by the distance between L_a and H bands, and it again becomes an indirect-gap semiconductor. Maximum value of the energy gap in semiconductor region ($E_g \sim 0.025$ eV) is achieved near $x = 0.15 \div 0.17$, when the tops of L_s and H-bands coincide, following which the energy gap is reduced, i.e. $Bi_{1-x}Sb_x$ solid solutions in semiconductor region refer to narrow-gap semiconductors. At $x \sim 0.22$ the tops of H and L_a bands are set on the same level, semiconductor-semimetal transition is realized and at $x > 0.22$ $Bi_{1-x}Sb_x$ solid solutions acquire semimetallic properties. Their band structure is qualitatively similar to the band structure of pure antimony with localization of charge carriers at points L (electrons) and H (holes) of the Brillouin zone [1 – 4, 8]. High nonparabolicity of electron L – bands, strong temperature dependences of band parameters (finally not reliably established to date) largely complicate the interpretation of kinetic properties even at sufficiently low temperatures.

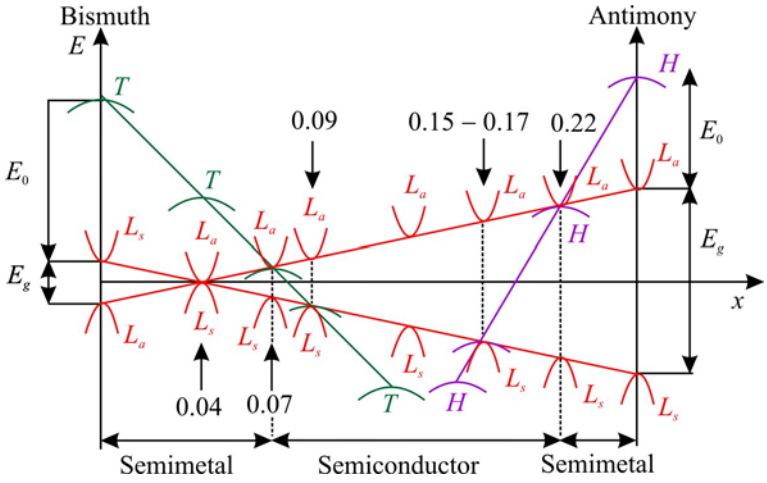

Fig. 1. Schematic of arrangement of energy bands in $Bi_{1-x}Sb_x$ solid solutions at 0 K [2].

The majority of studies on TE properties of $Bi_{1-x}Sb_x$ were performed on single-crystal samples [9 – 25] with a large concentration step. It was established that the dependences of electric conductivity $\sigma(x)$ and thermal conductivity $\lambda(x)$ are curves with a minimum in semiconductor region [9 – 20], and the dependences of the Hall coefficient $R_H(x)$ and the Seebeck coefficient $S(x)$ are curves with a maximum at the largest values of E_g [8, 9, 12 – 15, 17 – 20]. The authors of [24] on the dependence $\sigma(x)$ for $Bi_{1-x}Sb_x$ single crystals discovered an abnormal reduction of σ close to $x \sim 0.03$. According to different authors, the type of dependence of charge carriers on composition $\mu(x)$ is different. For instance, in conformity with [9, 22, 23], with increase in Sb concentration to $x = 0.3$, the value of μ is decreased for single crystals, and according to [26, 27] it is also observed for polycrystals. At the same time, for single crystals [13] and polycrystals [28, 29] mobility growth was discovered in the concentration ranges $x = 0 – 0.08$ [13], $x = 0 – 0.10$ [28] and $x = 0.08 – 0.10$ [29].

The authors of [21, 25] reported on having discovered for two $Bi_{1-x}Sb_x$ single crystals two maxima on the dependence $Z(x)$ at $T \sim 70$ K [21], ~ 82 K and ~ 95 K [25] close to compositions $x = 0.09$ and 0.16, whereby the peaks of T and H bands are on the same level with L bands. The authors of [21, 25] made an assumption that the observed dependence $Z(x)$ is caused by interband scattering of holes that takes place at transitions between the bands of "light" and "heavy" holes. Within the interval $x = 0.09 – 0.16$ the interband scattering is maximum, when the band extrema of "heavy" holes (T and H) coincide with the band extremum of "light" holes, which takes place close to compositions $x = 0.09$ and 0.16. It was noted that at higher temperatures maxima are not seen, and at room temperature a very weak dependence $Z(x)$ is observed.

The works dedicated to studying TE properties of $Bi_{1-x}Sb_x$ polycrystals mostly investigated pressed samples, and the object of study were either individual compositions [35 – 45] or alloys in the narrow range of compositions [31 – 34], or $Bi_{1-x}Sb_x$ solid solutions with a large step of Sb concentration [26 – 30]. It was established that the type of concentration and temperature dependences of TE properties of $Bi_{1-x}Sb_x$ polycrystals and single crystals is mainly similar [26 – 34], though the properties of polycrystals are essentially affected by grain size d: with a decrease in d the values of σ and λ are reduced, and the values of S are increased [37 – 45]. The latter fact was attributed [40] to reduction of relaxation time of charge carriers due to additional scattering at grain boundaries. In [37 – 39] it was shown that at $d > 200$ μm the values of σ and λ of $Bi_{1-x}Sb_x$ polycrystals approach the values of σ and λ for single crystals measured along the direction perpendicular to trigonal axis, and the values of the Seebeck coefficient are less than the values corresponding to S of single crystals. At grain size $d \sim 2.5$ μm [38, 39], ~ 10 μm [40] and ~ 0.05 μm [45] in $Bi_{1-x}Sb_x$ polycrystals in the range of compositions $x = 0.12 – 0.15$ the values of $Z = (0.9 – 1.1) \cdot 10^{-3}$ K^{-1} are achieved at 300 K. Maximum value of $Z = 1.5$ 10^{-3} K^{-1} at room temperature was obtained for $Bi_{85}Sb_{15}$ polycrystals with grain size $d \sim 0.04$ μm, made by pressing method at 523 K for 20 min under pressure 6 GPa [44, 45].

In [46 – 55] we studied $Bi_{1-x}Sb_x$ polycrystals with antimony content not exceeding $x = 0.12$, obtained by melting Bi and Sb in evacuated quartz ampoules with subsequent annealing at temperature 520 K. In addition to cast samples, we also prepared cold pressed samples under pressure 400 MPa, which after pressing were annealed for 250 hours [49 – 51]. It was shown [49] that the time of annealing of cast samples, as well as transition from cast to pressed samples practically does not affect the values of S and that annealing of both cast and pressed samples leads to electric conductivity and charge carrier increase, defining Z increase. On the dependences of unit cell parameters [47, 53], microhardness [48, 49, 54], thermal conductivity [52], heat capacity [55], TE and galvanomagnetic properties [46 – 51] on Sb concentration close to compositions $x = 0.01$, 0.03 and 0.06 we discovered anomalous areas which we attributed to critical phenomena accompanying percolation-type transition from diluted to concentrated solid solutions, transition to gapless state and semimetal-semiconductor transition, respectively. The dependences $Z(x)$ also were of non-monotonic type. It was established that a change in sample preparation technology does not affect the existence of concentration anomalies of TE and galvanomagnetic properties.

However, in [46 – 53] $Bi_{1-x}Sb_x$ polycrystals were studied in different concentration ranges: $x < 0.02$ [51], $x < 0.05$ [48], $x = 0.01 – 0.05$ [49], $x < 0.09$ [47, 50, 52, 53], $x < 0.12$ [46, 54], and cast samples were distinct in annealing times after synthesis: ~ 100 h [48], ~ 200 h [46 – 48, 50, 51], ~ 1200 h [49, 50, 51], 720 h [52 – 54]. Moreover, said publications studied various properties which further complicates comparing the results of different works. As regards the values of TE figure of merit, the values of Z were generally estimated in these works with the use of thermal conductivity

values obtained for single crystals; only in [52] the values of λ were measured for polycrystalline pressed samples in the composition range $x = 0 – 0.09$ and it was shown that these values are close to those obtained by averaging λ values of single crystals measured along the trigonal axis and perpendicular to this direction.

In connection with the above it is interesting to study TE properties depending on the composition of $Bi_{1-x}Sb_x$ polycrystals prepared over a wide concentration range and under identical technological conditions.

It determined the main tasks set in the present paper: 1) to increase the number of various investigated compositions of $Bi_{1-x}Sb_x$ for greater probability of revealing the specific features on the concentration dependences of properties; 2) to get samples of various composition not just under strictly identical conditions (like, for instance, growing single crystals of various composition), but in one technological cycle; 3) to study a wide composition range ($x = 0 – 0.25$) covering semimetallic and semiconductor areas and allowing to trace the influence of qualitative change of electronic structure with a change in composition on the properties; 4) to use cast polycrystalline samples as the objects for study, unlike the majority of works which studied either single crystals or pressed samples.

From the results obtained in this paper it follows that with a detailed investigation of TE properties of polycrystalline $Bi_{1-x}Sb_x$ cast samples even at room temperature, apart from the concentration anomalies of TE properties in the range $x = 0 – 0.1$ that we had discovered earlier, one can reveal a non-monotonic type of TE properties variation with composition in the concentration range $x > 0.1$ related to peculiarities of variation in the band structure of $Bi_{1-x}Sb_x$ solid solutions with a change in composition (redistribution of charge carriers in different energy bands (*L*, *T*, *H*), interband scattering, etc).

Experimental procedure

Polycrystalline cast samples of $Bi_{1-x}Sb_x$ ($x = 0 – 0.25$) solid solutions were obtained from high-purity (not less than 99.999 % of the basic component) *Bi* and *Sb* elements by melting them in evacuated quartz ampoules at temperature (1020 ± 10) K, holding in the melt for 5 hours with the use of vibratory agitation. With a view to obtain samples with small grain size (to accelerate diffusion processes in solid state), the melt was subject to quenching in the air, following which the samples were again placed into furnace and annealed for 720 hours at temperature (520 ± 5) K for homogenization of alloys and to obtain compositionally uniform ingots. In one technological process there were simultaneously synthesized and thermally treated 30 samples of various composition with concentration step from $\Delta x = 0.0025$ to $\Delta x = 0.02$. In [52], we used a similar thermal treatment in the preparation of cast $Bi_{1-x}Sb_x$ alloys in the concentration range $x < 0.1$, however, synthesized samples were then subject to cold pressing under 400 MPa and subsequent annealing for 250 hours, and on these samples measurements of thermal conductivity and other TE properties were made.

In the present paper, measurements of TE and galvanomagnetic properties were made on the cast samples. For this purpose, samples in the shape of parallelepipeds of size 10 × 3 × 2 mm were cut from the resulting ingots to measure σ and R_H, and in the shape of cylinders of height 5 mm and diameter 15 mm to measure λ and *S*. The Seebeck coefficient *S* was measured by compensation method with respect to copper electrodes with an accuracy of ± 3 %, and R_H and σ were measured by standard *dc* method in a magnetic field $B = 0.05$ T, which for $Bi_{1-x}Sb_x$ solid solutions at 300 K is a weak magnetic field [55], with an accuracy not more than 5 %. Thermal conductivity λ was measured by dynamic calorimeter method on the IT – λ - 400 installation in the temperature range 170 – 520 K [56]. The technique for measurement of λ is described in detail in [52]. For each sample

the temperature dependences λ(*T*) were obtained at least twice, and the difference between the resulting values of λ did not exceed 5 %, which corresponded to thermal conductivity measurement error. By the results of measuring λ a dependence λ(*x*) was constructed at *T* = 300 K. The resulting values of σ, *S* and λ were used to calculate the values of TE figure of merit *Z*.

Experimental results

Fig. 2*a* – fig. 2*c* represent the dependences *S*(*x*), $R_H(x)$ and σ(*x*) obtained for $Bi_{1-x}Sb_x$ alloys and having, as we can see, a non-monotonic nature, uncommon for continuous solid solution.

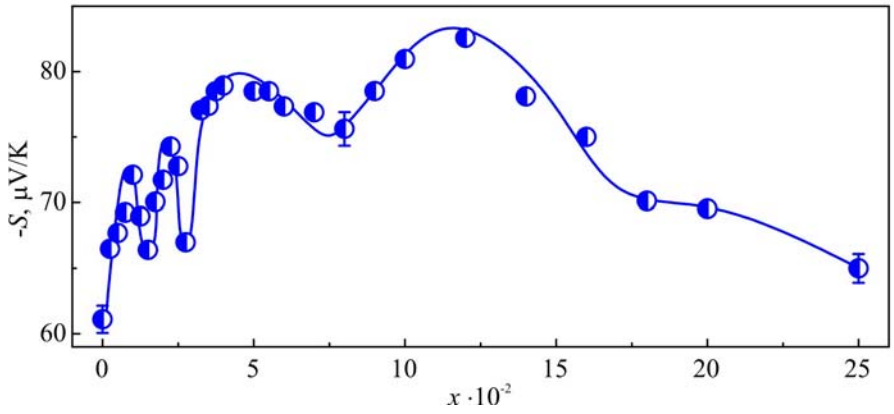

a)

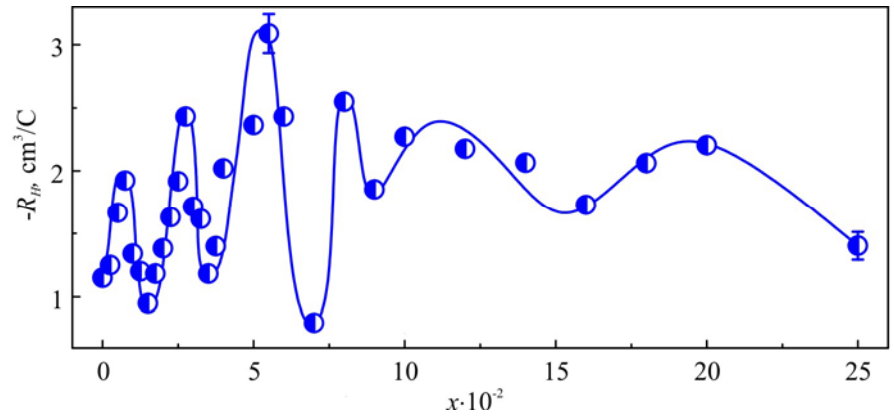

b)

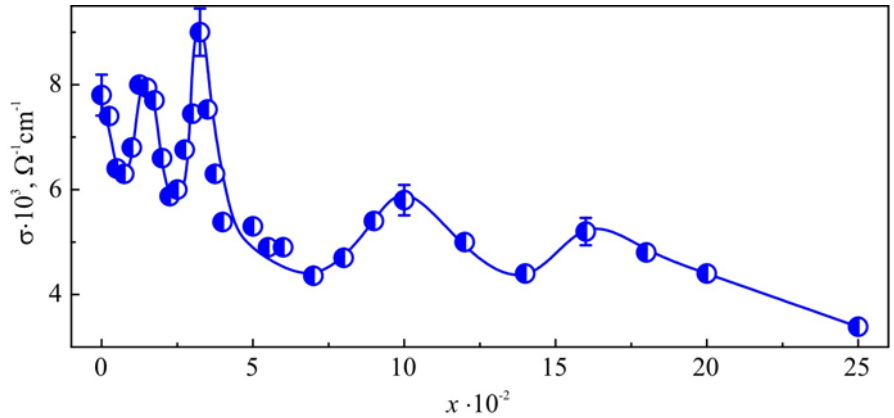

c)

Fig. 2. Dependences of the Seebeck coefficient S (a), the Hall coefficient R_H (b) and electric conductivity σ (c) on the composition x of polycrystalline $Bi_{1-x}Sb_x$ solid solutions at temperature 300 K.

Note first of all the observed similarity between the dependences $S(x)$ and $R_H(x)$. Firstly, up to $x \sim 0.12$, despite the non-monotonic oscillating behaviour of these curves, there is a tendency to growth of S and R_H with increase in x. Secondly, in both cases in the concentration ranges $x = 0.01 \div 0.015$, $x = 0.025 \div 0.035$ and $x \sim 0.05 \div 0.10$ on the dependences $S(x)$ and $R_H(x)$ there is an anomalous reduction of S and R_H with increase in antimony content. We have observed such concentration anomalies earlier [46 – 55] in the investigation of cast $Bi_{1-x}Sb_x$ samples obtained with the use of other kinds of thermal treatment, as well as pressed samples prepared therefrom. We attributed the presence of anomalies to manifestation of critical phenomena accompanying electron phase transitions occurring in $Bi_{1-x}Sb_x$ solid solutions with increase in antimony concentration. Thirdly, positions of maxima and minima on the dependences $S(x)$ and $R_H(x)$ practically coincide for the concentration ranges $x = 0.01 – 0.015$ and $x = 0.025 – 0.035$ (though S and R_H were measured independently), but differ for the range $x \sim 0.05 – 0.10$: on the dependence $R_H(x)$ in the composition range $x = 0.05 – 0.10$ there are two areas of anomalous reduction of R_H in contrast to S, where one minimum is observed close to $x \sim 0.07$.

From the dependence $\sigma(x)$ it is seen (Fig. 2*c*) that over the entire investigated composition range ($x = 0 – 0.25$) with a general non-monotonic behaviour of the curve there is a tendency to electric conductivity drop with increase in x. In the composition area $x = 0 – 0.1$, like in the case of S and R_H, there are concentration anomalies (growth of σ with increase in x), and maxima on the curves S and R_H are matched by minima on the curve $\sigma(x)$, which is easy to explain by different dependence of these kinetic coefficients on charge carrier concentration.

As regards thermal conductivity of $Bi_{1-x}Sb_x$, there is a tendency to reduction of λ with increase in *Sb* concentration to $x \sim 0.16$, following which λ increases slightly (Fig. 3). Like in the case of other kinetic coefficients, on the curve $\lambda(x)$ there are areas of anomalous change (growth) of thermal conductivity with increase in *Sb* concentration, though the anomalies corresponding to transition to gapless state and semimetal-semiconductor transition are not so distinctly divided in concentration, as in the case of curves $\sigma(x)$, $S(x)$ and $R_H(x)$, and partially overlap. It should be also noted that the values of λ obtained here for cast samples practically coincide with the values of λ reported in [52], where λ was measured for pressed samples ($x < 0.1$) prepared prior to pressing by the same technique as cast samples in the present work.

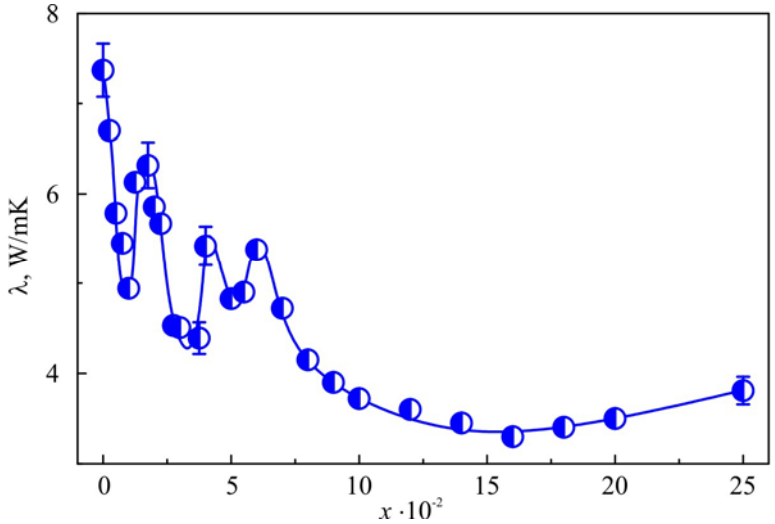

Fig. 3. Dependence of thermal conductivity λ on the composition x of polycrystalline $Bi_{1-x}Sb_x$ solid solutions at temperature 300 K.

At $x > 0.1$ such pronounced extrema on the dependences $\sigma(x)$, $S(x)$ and $R_H(x)$ are not observed. It can be seen that on the curve $S(x)$ close to composition $x = 0.12$ there is a maximum, following which S is monotonically reduced with increase in x and some inflection in the vicinity of $x = 0.15$. As regards electric conductivity, after the composition $x = 0.1$ the electric conductivity drops to $x \sim 0.14$, then slightly increases to $x \sim 0.16$ and again decreases (Fig. 2*c*). Thus, in the vicinity of composition $x = 0.15$ there are minima on the dependences $\lambda(x)$ and $R_H(x)$, a maximum on the dependence $\sigma(x)$ and an inflection on the curve $S(x)$.

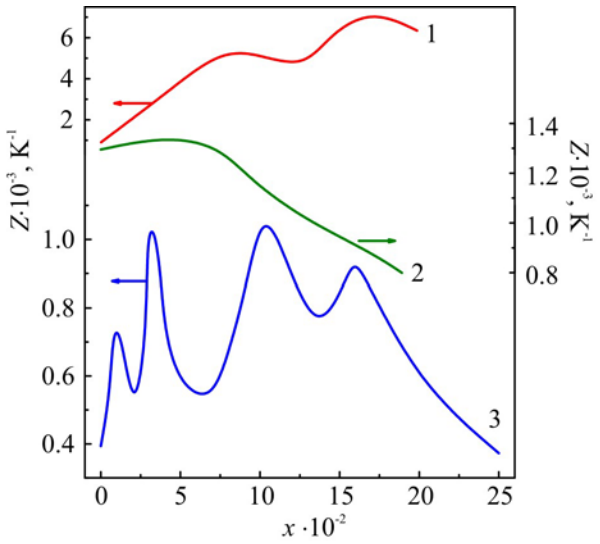

Fig. 4. Dependences of thermoelectric figure of merit Z on the composition x of single crystals (curves 1 and 2) and polycrystals (curve 3) of $Bi_{1-x}Sb_x$ solid solutions at temperatures 300 K (curves 2 and 3) and 60 K (curve 1). Curves 1 u 2 – the results of work [21], curve 3 – the results of the present work.

Based on the resulting values of σ, S and λ, the values of TE figure of merit were calculated. Fig. 4 represents the dependence $Z(x)$ obtained in the present paper for room temperature from which it is seen that in the investigated concentration range on the curve $Z(x)$ one can see four maxima corresponding to compositions $x \cong 0.01$, 0.03, 0.1 and 0.16. Maximum value of Z corresponds to compositions $x = 0.03$ and $x = 0.1$ ($Z = 1.05 \pm 0.05$). For comparison, Fig. 4 shows the dependences $Z(x)$ obtained in [19] for single crystals at temperatures 60 K and 300 K.

Discussion of the results

1. If we mentally draw monotonic components of the dependences $S(x)$, $R_H(x)$, $\sigma(x)$ and $\lambda(x)$, it can be said that the dependences $S(x)$ and $R_H(x)$ are curves with a maximum in the vicinity of composition $x = 0.12$, and curves $\sigma(x)$ and $\lambda(x)$ show that with a growth of antimony content, σ and λ drop. Such type of the dependence of various properties on the composition of $Bi_{1-x}Sb_x$ solid solutions basically agrees with the data reported in the literature (see above).

As regards the drop of σ and λ with increase in x, similar type of the dependences is typical of solid solutions and can be easily explained by the fact that introduction of impurity component to matrix results in distortions of crystal lattice and chemical bonds and, accordingly, in the emergence of additional centres of electron and phonon scattering, reduction of charge carrier mobility and phonon mean free path length.

On the other hand, with increase in *Sb* content, the value of overlap of the hole *T* and electron L_s bands is reduced, which leads to a reduction of charge carrier concentration, hence, to growth of *S* and R_H. After semimetal-narrow-gap semiconductor transition, growth of energy gap width with increase of *x* to $x \sim 0.12 – 0.15$ also results in the drop of charge carrier concentration, hence, in the growth of *S* and R_H. With increasing concentration $x > 0.12 – 0.15$, the energy gap is reduced, charge carrier concentration grows and a drop of *S* and R_H is observed.

2. Considering the obtained dependences of kinetic coefficients on the composition of $Bi_{1-x}Sb_x$ solid solution in a wide concentration range ($x = 0 – 0.25$) and taking into account our data obtained earlier, it can be seen that the basic difference between these results and the numerous works of other authors studying concentration dependences of properties in $Bi_{1-x}Sb_x$ system is a complicated, oscillating type of dependences $\sigma(x)$, $S(x)$, $R_H(x)$ and $\lambda(x)$ that we noticed for the first time. It was difficult to predict a priori such behaviour of property isotherms with regard to the fact that bismuth and antimony, similar in structure, chemical bond and energy spectrum construction, form a continuous series of solid solutions at all temperatures. Nevertheless, such type of dependences can be explained, at least qualitatively, based on the experimental data, repeatedly confirmed, taking into account the specificity of initial components and the data established today on the character of reconstruction of electron energy spectrum with a change in the composition of $Bi_{1-x}Sb_x$ solid solution. According to [46 – 55], the observed concentration anomalies of kinetic coefficients point to the existence in $Bi_{1-x}Sb_x$ solid solutions at certain *Sb* concentrations of phase transitions accompanied by critical phenomena: percolation-type transition from dilute to concentrated solid solutions, transition to gapless state and semimetal-semiconductor transition.

The type of the dependences $\sigma(x)$, $S(x)$, $R_H(x)$ and $\lambda(x)$ at room temperature in the composition range $x < 0.1$ – the presence of pronounced extrema at certain compositions – coincides with what we have seen earlier [46 – 55] for cast and pressed samples, prepared by different techniques (mainly different time of post-synthesis annealing).

From the obtained results it follows that both a more detailed investigation of the dependences of properties on the composition (the use of a large number of alloys of various composition) and the use of cast polycrystalline samples prepared under strictly identical conditions as the objects of study confirms the presence of three concentration anomalies which we attribute to electronic phase transitions.

However, the presence of a greater number of alloys with different compositions made it possible to discover on the dependence $R_H(x)$, apart from the peak close to $x = 0.06$, an additional peak close to $x = 0.08$, the presence of which can be explained, taking into account the peculiarities of $Bi_{1-x}Sb_x$ band structure and, in particular, the existence of "light" and "heavy" holes (Fig. 1).

Indeed, when with increasing concentration of *Sb* the top of valence *T*-band and the bottom of *L* conduction band are set on the same level, an electronic semimetal-indirect-gap semiconductor transition takes place. With further increase of *x*, as the top of *T*-band drops in energy, the situation is achieved when the top of *T*-band is set on the same level with the top of valence *L*-band, and the semiconductor becomes direct-gap. The character of change in kinetic properties, including thermoelectric, in the area of transition from indirect-gap to direct-gap semiconductor ($x = 0.06 – 0.09$) is rather complicated, being accompanied by a change in the contribution of "light" *L* and "heavy" *T* holes to kinetic coefficients, a change in the energy gap, effective mass, the Hall factor and other parameters. With increase in *x* and further reduction of *T* band in the energy, the contribution to kinetic coefficients of "light" holes increases and the

contribution of "heavy" holes decreases. At the same time, the energy gap increases which must lead to a reduction of charge carrier concentration, i.e. to growth of R_H. The influence of these factors on different kinetic coefficients will not be identical. One should also point to strong nonparabolicity of light holes band and the related strong dependence of band parameters at *L*-points of the Brillouin zone on the temperature, composition and technology of samples manufacturing technique. All these peculiarities of $Bi_{1-x}Sb_x$ band structure complicate analysis of transport properties and determination of electronic parameters by the kinetic properties.

The Hall coefficient is very sensitive to a change in the type and concentration of charge carriers. The presence of sharp peaks of R_H at compositions corresponding to system transition to gapless state and semimetal-indirect-gap semiconductor (Fig. 2*b*) testifies to high sensitivity of this kinetic coefficient to qualitative changes in the band structure. Obviously, a change in R_H will not be so considerable, when the band structure does not change so radically, for instance, in the situation when transition from indirect-gap to direct-gap semiconductor occurs, as it takes place at $x \sim 0.08 – 0.09$. The complicated character of dependence $R_H(x)$ in the composition range $x = 0.05 – 0.1$, where we observe two areas of the abnormal reduction of R_H, is attributed to the presence of two electronic transitions in this composition range: a semimetal-indirect-gap semiconductor transition (the energy gap appears between *T* and L_s bands) at $x \sim 0.06 – 0.07$ and an indirect-gap to direct-gap semiconductor transition (the energy gap appears between L_s and L_a gaps) at $x \sim 0.08 – 0.09$ (Fig. 1). On the dependences $\sigma(x)$ and $S(x)$ these two transitions cannot be "allowed" in concentration in view of lower sensitivity of σ and *S* (as compared to R_H) to changes in the relative contribution of various types of carriers to kinetic coefficients, as well as in view of proximity of concentrations whereby these transitions occur, which leads to overlap of abnormal areas on the dependences $\sigma(x)$ and $S(x)$ in the concentration range $x = 0.05 – 0.10$.

3. In conformity with the band structure of $Bi_{1-x}Sb_x$ solid solutions at 0 K (Fig. 1), in the range $x = 0.1 \div 0.25$ the presence of peculiarities on the dependences $\sigma(x)$, $S(x)$, $R_H(x)$ and $\lambda(x)$ might have been expected at critical compositions corresponding to establishment on the same level of the tops of "heavy" *H* and "light" L_s valence bands, when the energy gap is maximal ($x = 0.15 – 0.17$), as to touching the top of "heavy" *H*-band and the bottom of L_a-band (at $x = 0.22$). With a rise in temperature, critical compositions can shift to either side depending on the temperature dependences of kinetic coefficients, the energy gap, effective masses, etc. Based on the obtained dependences $\sigma(x)$, $S(x)$, $R_H(x)$ and $\lambda(x)$ one can suggest that the anomalies on these curves in the region of compositions close to $x = 0.14 – 0.16$ are related to touching the tops of "heavy" *H* and "light" L_s valence bands, when maximum value of the energy gap is achieved and a transition from direct-gap to indirect-gap semiconductors takes place, with redistribution of charge carriers from L_s valence band to *H*-band. Small number of investigated compositions in the range $x = 0.16 \div 0.25$ does not allow to fix semiconductor-semimetal transition.

4. As mentioned above, the authors of [21, 25] reported on having observed at low temperatures in the undoped $Bi_{1-x}Sb_x$ solid solutions two maxima on the dependence $Z(x)$ close to compositions $x = 0.09$ and $x = 0.16$, having attributed their presence to the coincidence at above compositions of the extrema of "heavy" *T* and *H* valence bands with the maxima of "light" hole *L* bands. The reduction of *Z* beyond the concentration range $x = 0.09 \div 0.16$ was treated as the result of thermal gap reduction. From the figure given in [21] it is seen that with a rise in temperature to 120 K, on the dependence $Z(x)$ there is one diffuse maximum close to $x = 0.12$, and at room temperature $Z = 1.3\ 10^{-3}\ K^{-1}$ up to $x \sim 0.07$, and then with increase in *x* it is reduced to $Z = 0.8\ 10^{-3}\ K^{-1}$ at $x = 0.2$.

The authors of [21, 25] surmised that in the range $x = 0.09 \div 0.16$ the top of the valence band consists of "light" mobile holes the presence of which has a negative influence on the value of Z. As long as "heavy" holes corresponding to additional band maxima have considerably lower mobilities, approach of one of these maxima to the main L-extremum reduces the concentration of "light" holes, increasing simultaneously electron concentration. If concentration is not optimal, it may result in Z increase. On the other hand, another factor contributing to growth of Z can be interband scattering due to transitions between the bands of "light" and "heavy" holes that can reduce considerably the mobility of "light" holes and, consequently, increase Z in n-type semiconductors. According to the authors of [21, 25], the minimum between two maxima close to compositions $x = 0.09$ and $x = 0.16$ can disappear at higher temperatures, as long as with a rise in temperature the value of kT quickly approaches the value of energy gap between two valence bands.

However, as it follows from Fig. 4, we managed even at room temperature to reveal on the dependence $Z(x)$ four maxima close to compositions corresponding to $x = 0.01$, 0.03, 0.1 and 0.16. The authors of [21, 25] reported only on the presence of the two last extrema that had been observed by them only at low temperatures. Note also that the values of Z obtained in our paper for cast polycrystalline samples and corresponding to extrema close to compositions $x = 0.1$ and 0.16 practically coincide with the values of Z obtained by the authors of [21, 25] for single-crystal samples at room temperature.

Conclusion

A detailed investigation was performed at room temperature of the concentration dependences of galvanomagnetic and TE properties of polycrystalline cast $Bi_{1-x}Sb_x$ ($x = 0 – 0.25$) samples prepared by melt quenching in the air and subsequent homogenizing annealing for 720 hours at temperature (520 ± 5) K. The analysis of the results allowed formulating the following conclusions.

1. The presence of anomalies was confirmed on the dependences of electric conductivity, the Seebeck coefficient, the Hall coefficient and thermal conductivity on the composition of $Bi_{1-x}Sb_x$ alloys that we had observed earlier close to $x = 0.01$; $x = 0.03$ and $x = 0.07$ on the cast samples after different kinds of thermal treatment and on pressed samples, and was attributable to manifestation of critical phenomena at phase transition of percolation type, transition to gapless state and semimetal-semiconductor transition, respectively.
2. For the first time the complicated type of dependence $R_H(x)$ was revealed in the composition range $x = 0.05 – 0.1$, manifested in the presence of two areas of abnormal reduction of R_H. The observed effect is interpreted as a consecutive manifestation of semimetal-indirect-gap semiconductor and indirect-gap semiconductor-direct-gap semiconductor transitions.
3. It was shown that at $x > 0.1$ the concentration dependences of properties are also of non-monotonic nature. The complicated type of dependences at $x > 0.1$ is attributable to qualitative changes in the structure of $Bi_{1-x}Sb_x$ energy spectrum at certain critical compositions, a change in the relative contribution to conductivity of charge carriers from various energy bands with a change in antimony concentration, as well as to high sensitivity of electron spectrum and physical properties of $Bi_{1-x}Sb_x$ to external effects.
4. On the dependence of TE figure of merit Z on the composition of $Bi_{1-x}Sb_x$ solid solutions at room temperature there were revealed four maxima close to compositions corresponding to $x = 0.01$, 0.03, 0.1 and 0.16. The presence of extrema on the curve $Z(x)$ is related to qualitative

changes in the energy spectrum of charge carriers at some critical compositions in $Bi_{1-x}Sb_x$ system determining the existence of electron concentration phase transitions accompanied by critical phenomena.

5. It was shown that at room temperature on the cast polycrystalline samples prepared by quenching in the air and subsequent annealing for 720 hours at (520 ± 10) K one can achieve the values of TE figure of merit Z that are not inferior to the values of Z obtained on polycrystals subject to a longer annealing, as well as on single-crystal samples.

References

1. L.I. Anatychuk, *Thermoelements and Thermoelectric Devices: Reference Book* (Kyiv: Naukova Dumka, 1979), 768 p.
2. B. Lenoir, H. Scherrer, and T. Caillat, An. Overview of Recent Developments for *BiSb* Alloys, Chapter 4, In: *Tritt T.M. (ed.) Semiconductors and Semimetals: Recent Trends in Thermoelectric Materials Research I, Vol. 69* (San Diego, Academic Press, 2001), p. 101 –137.
3. V.M. Grabov and O.N. Uryupin, *Bi-Sb* Alloys: Thermopower in Magnetic Field, Chapter 28. *In: Rowe D.M. (Ed.) Thermoelectrics Handbook: Macro To Nano* (Boca Raton, CRC Press), 2006.
4. Ya.A. Ugay, Ye.G. Goncharov, G.V. Semenova, and V.B. Lazarev, *Phase Equilibria Between Phosphorus, Arsenic and Bismuth* (Moscow: Nauka, 1989), 233 p.
5. L. Fu, C.L. Kane, and E.J. Mele, Topological Insulators in Three Dimensions, *Phys. Rev. Lett*. 98, 106803 (2007).
6. D. Hsieh, D. Qian, L. Wray, Y. Xia, Y.S. Hor, R.J. Cava, and M.Z. Hasan, A Topological Dirac Insulator in a Quantum Spin Hall Phase, *Nature* 452, 970 – 974 (2008).
7. P. Ghaemi, R.S.K. Mong, and J. Moore, In-Plane Transport and Enhanced Thermoelectric Performance in Thin Films of the Topological Insulators Bi_2Te_3 and Bi_2Se_3, *Phys. Rev. Lett.* 105, 166603 (2010).
8. N.B. Brandt, R. Hermann, G.I. Golysheva, L.I. Devyatkova, D. Kusnik, D. Kraak, and Ya.G.Ponomarev, Electron Fermi Surface of Semimetallic Alloy $Bi_{1-x}Sb_x$, *Sov. Phys. JEPT* **56** (6), 1247 – 1256 (1982).
9. A.L. Jain, Temperature Dependence of the Electrical Properties of Bismuth-Antimony Alloys, Phys. Rev., 114 (6). – 1959. - p. 1518-1528.
10. T. Yazaki, Thermal Conductivity of Bismuth-Antimony Alloy Single Crystals, *J. Phys. Soc. Jpn.* **25** (4), 1054 – 1060. (1968)
11. T. Yasaki and Y. Abe, Galvanomagnetic Investigations of the $Bi_{1-x}Sb_x$ ($0 < x < 0.15$) System at 77 K, *J. Phys. Soc. Jpn*. **24** (2), 290 – 295 (1968). Electrical Properties of Bismuth-Antimony Alloys, *Phys. Rev*. **114** (6), 1518 – 1528 (1959).
12. G.A. Ivanov and A.R. Regel, Electrical Properties of Bismuth Alloys. Solubility of Impurities and the Character of their Impact on the Electrical Properties of Bismuth, *Technical Physics* **25** (1), 39 – 48 (1955).
13. G.A. Ivanov and A.M. Popov, Electrical Properties of Bismuth-Antimony Alloys, *Physics of the Solid State* **5**(9), 2409 – 2419 (1863).
14. G.A. Ivanov, G.N. Kolpachnikov, V.L. Naletov, and T.A. Yakovleva, Electrical and Galvanomagnetic Properties of *Bi-Sb* Alloys in the Temperature Range of 77 – 293 K, Semimetals: *Proceedings of Leningrad Polytechnic Institute* **384** (4), 39 – 47 (1968).

15. V.L. Naletov, G.A. Ivanov, T.A. Yakovleva, and V.I. Nikolaev, On Transport Phenomena in *Bi-Sb* Alloys, *Izvestiya of USSR Academy of Sciences. Inorganic Materials* **7**(8), 1321 – 1324 (1971).
16. N. Wagner, O. Brümmer, and H.R. Prietzsch, Untersuchungen zur Wär-meleitfähigkeit von *Bi-Sb*-einkristallen, *Kristall und Technik* **9**(10), 1153 – 1165 (1974).
17. W.M. Yim and A. Asmith, *Bi-Sb* Alloys for Magneto-Thermoelectric and Thermomagnetic Cooling, *Solid State Electronics* **15**(10), 1141 – 1165 (1972).
18. S.D. Probert and C.B. Thomas, Transport Properties of Some Bismuth-Antimony Alloys, *Applied Energy* **5**(2), 127 – 140 (1979).
19. B. Lenoir, M. Cassart, Yu. Ravich, and H. Scherrer, Highest Figure of Merit in Undoped $Bi_{1-x}Sb_x$ Alloys, *Proc. 15th Int. Conf. on Thermoelectrics (St. Petersburg, 1995)*, p.96 – 99.
20. B. Lenoir, M. Cassart, J.-P. Michenaud, H. Scherrer, and S. Scherrer, Transport Properties of *Bi*-rich *Bi-Sb* Alloys, *J. Phys. Solids* **57**(1), 89 – 99 (1996).
21. B. Lenoir, A. Dauscher, M. Cassart, Y.I. Ravich, and H. Scherrer, Effect of Antimony Content on the Thermoelectric Figure of Merit of $Bi_{1-x}Sb_x$ Alloys, *J. Phys. Chem. Solids* **59**(1), 129 – 134 (1998).
22. L.A. Kirakozova, A. Krapf, W. Kraak, M.Yu. Lavrenyuk, and N.Ya. Minin, Energy Gap Structure in Semiconducting $Bi_{1-x}Sb_x$ Alloys, *Phys. Stat. Sol. (b)* 169, 417 – 427 (1992).
23. V.S. Zemskov, A.D. Belaya, U.S. Beluy, and G.N. Kozhemyakin, Growth and Investigation of Thermoelectric Properties of *Bi-Sb* Alloy Single Crystals, *J.Crys. Grown* 212, 161 – 166 (2000).
24. Yu.M. Bondarev, E.G. Goncharov, and I.V. Miller, Extremums of Properties in Bismuth-Antimony System, *Bulletin of Voronezh State University: Chemistry, Biology, Pharmacy* 1, 16 – 20 (2004).
25. V.M. Grabov, G.A. Ivanov, V.L. Naliorov, and A.F. Panarin, Interband Scattering of Charge Carriers and Thermoelectric Figure of Merit of Bismuth-Antimony Alloys, *Soviet Seminar of Semiconductor Materials for Thermoelectric Conversion (Leningrad, 1985)*, p. 30 – 31.
26. G.A. Ivanov, A.M. Popov, and B.I. Chistyakov, Electric Properties of Double Bismuth Alloys in a Wide Temperature Range. I Solid Solutions of *Sn*, *Sb* and *Te* in Bismuth (Polycrystals), *The Physics of Metals and Metallography* **16**(2), 184 – 192(1963).
27. S. Tanuma, Semiconducting Properties of *Bi-Sb* Alloys, *J. Phys. Soc. Jpn*. 14, 1246 (1959).
28. S. Tanuma, Concentration Dependence of Electrical Properties of Bismuth-Antimony Alloys, *J. Phys. Soc. Jpn.* 16, 2349 (1961).
29. S. Tanuma, Thermoelectric Power of Bismuth-Antimony Alloys, *J. Phys. Soc. Jpn.* 16, 2354 –2355 (1961).
30. V.M. Grabov, O.N. Uryupin, and V.A. Komarov, Thermoelectric Properties of Polycrystalline *Bi* and *Bi-Sb* Alloys, *Proc. 17th Int. Conf on Thermoelectrics (Nagoya, Japan, 1998)*, p. 78 –81.
31. T.K. Dey and S.K. Ghatak, Temperature Dependence of Electrical Conductivity and Thermoelectric Power of *Bi-Sb* Tapes Prepared by Liquid Quenching, *J. Phys*. **32**(2), 161 – 166 (1989).
32. H. Kitagawa, H. Noguchi, M. Itoh, and Y. Noda, Thermoelectric Properties of Semiconducting *Bi*-rich *Bi-Sb* Alloys, *Proc. 22nd Int. Conf. on Thermoelectrics*, 2003, 290 – 293.
33. H. Kitagawa, H. Noguchi, T. Kiyabu, M. Itoh, and Y. Noda, Thermoelectric Properties of *Bi – Sb* Semiconducting Alloys Prepared by Quenching and Annealing, *J. Phys. Chem. Solids* 65, 1223 –1227 (2004).

34. K. Malik, D. Das, D. Mondal, D. Chattopadhyay, A.K. Deb, S. Bandyopadhyay, and A. Banerjee, *Sb* Concentration Dependent Structural and Resistive Properties of Polycrystalline *Bi-Sb* Alloys, *J. Appl. Phys*. **112**(12), 083706 (2012).
35. S. Dutta, V. Shubha, T.G. Ramesh, and F. D'Sa, Thermal and Electronic Properties of $Bi_{1-x}Sb_x$ Alloys, *J. Alloy Compd*. 467, 305 – 309 (2009).
36. S. Dutta, V. Shubha, and T.G. Ramesh, Effect of Pressure and Temperature on Thermopower of *Bi – Sb* Alloys, *Physica B* **405**(5), 1239 – 1243 (2010).
37. G.A. Ivanov, V.L. Naletov, I.I. Fadeeva, and T.A. Yakovleva, Some Properties of Polycrystalline Samples of Bismuth and its Alloys with Antimony, Semimetals: *Proc. of Leningrad State Polytechnic Institute* 384(4), 21 – 29 (1968).
38. X. Devaux, F. Brochin, A. Dauscher, B. Lenoir, R. Martin-Lopez, H. Scherrer, and S. Scherrer, Observation of the Grain Size Influence on the Thermoelectric Properties of Polycrystalline Bismuth-Antimony Alloys, *Proc. 16th Int. Conf on Thermoelectrics*, 199 – 201 (1997).
39. X. Devaux, F. Brochin, R. Martin-Lopez, and H. Scherrer, Study of the Microstructure Influence on the Transport Properties of $Bi_{86.5}Sb_{13.5}$ Polycrystalline Alloy, *J. Phys. Chem. Solids* 62, 119 – 125 (2002).
40. R. Martin-Lopez, A. Dauscher, H. Scherrer, J. Hejtmanek, H. Kenzari, and B. Lenoir, Thermoelectric Properties of Mechanically Alloyed *Bi-Sb* Alloys, *Appl. Phys. A* 68, 597 – 602 (1999).
41. G. Cochrane and W.V. Youdelis, Transport and Thermoelectric Properties of Bismuth and *Bi*-12 at.pct *Sb* Alloy Powder Compacts, *Metal. Trans*. 3, 2843 – 2850 (1972).
42. D. Cadavid and J.E. Rodrigues, Thermoelectric Properties of *Bi-Sb* Samples Grown by Mechanical Alloy, *Phys. Stat. Sol. (c)* **2**(10), 3677 – 3680 (2005).
43. H.J. Liu and L.F. Li, Thermoelectric Properties of $Bi_{0.85}Sb_{0.15}$ Alloys Prepared by High Press Method, *AIP Conf. Proc*. 824, 43 – 50 (2006).
44. H.J. Liu, Y.L. Wu, R.J. Huang, Ch. Song and L.F. Li, Thermoelectric Properties of $Bi_{0.9}Sb_{0.1}$ Prepared by High Pressure, *J. Phys. Chem. Solids* **67**(7), 1492 – 1495 (2006).
45. H.J. Liu, Ch.M. Song, S.T. Wu, and L.F. Li, Processing Method Dependency of Thermoelectric Properties of $Bi_{85}Sb_{15}$ Alloys in Low Temperature, *Cryogenics* **47**(1), 56 – 60 (2007).
46. E.I. Rogacheva, A.A. Drozdova, and M.S. Dresselhaus, Anomalies in the Isotherms of the Thermoelectric Properties of *Bi-Sb* Solid Solutions, *Proc. 25th Int. Conf. on Thermoelectrics, 2006* (p. 107 – 110).
47. E.I. Rogacheva and A.A. Drozdova, Thermoelectric Properties of Polycrystalline Bismuth-Antimony Solid Solutions, *J. Thermoelectricity* 2, 22 – 28 (2006).
48. E.I. Rogacheva, A.A. Yakovleva (A.A. Drozdova), V.I. Pinegin, and M.S. Dresselhaus, Concentration Anomalies of Properties in *Bi-Sb* Semimetallic Solid Solutions, *J. Phys. Chem. Solids* **69**(2 – 3), 580 – 584 (2008).
49. E.I. Rogacheva, A.A. Drozdova, O.N. Nashchekina, M.S. Dresselhaus, and G. Dresselhaus, Transition into a Gapless State and Concentration Anomalies in the Properties of $Bi_{1-x}Sb_x$ Solid Solutions, *Appl. Phys. Lett*. **94**(20), 202111 (2009).
50. A.A. Drozdova, E.I. Rogacheva, M.V. Dobrotvorskaya, and P.V. Mateichenko, Influence of Specimen Preparation Technique on Isotherms of Properties in Bismuth-Antimony Solid Solutions, *J. Thermoelectricity* 2, 76 – 83 (2009).

51. E.I. Rogacheva, A.A. Drozdova, and O.N. Nashchekina, Percolation Effects in Semimetallic *Bi-Sb* Solid Solutions, *Phys. Stat. Sol. (a)* **207**(2), 344 – 347 (2010).
52. E.I. Rogacheva, A.N. Doroshenko, O.N. Nashchekina, and Yu.V. Men′shov, Thermal Conductivity in $Bi_{1-x}Sb_x$ Solid Solutions, *J. Electron. Mater*. **42**(7), 2098 – 2102 (2013).
53. E.I. Rogacheva, A.N. Doroshenko, V.I. Pinegin, and M.S. Dresselhaus, Electronic Phase Transitions and Structural Instability in $Bi_{1-x}Sb_x$ Solid Solutions, *J. Thermoelectricity* 6, 13 – 20 (2013).
54. E.I. Rogacheva, A.N. Doroshenko, O.N. Nashchekina, and M.S. Dresselhaus, Specific Heat Critical Behavior in $Bi_{1-x}Sb_x$ Solid Solutions, *Appl. Phys. Lett*. 109(13), 131906 (2016).
55. E.I. Rogacheva, A.A. Drozdova, I.I. Izhnin, and M.S. Dresselhaus, Magnetic Field Dependences of Galvanomagnetic Properties of Polycrystalline *Bi-Sb* Solid Solutions, *Phys. Stat. Sol. (a)* **206** (2), 298 – 302 (2009).
56. E.S. Platunov, *Thermophysical Measurements in Monotonous Mode* (Leningrad: Energiya, 1973), 143 p.

Submitted 10.09.2016

F.F. Aliev[1], E.R. Yuzbashov[1], A.B. Maharramov[1], U.M. Agayeva[2], M.M. Zarbaliev[2], B.A. Veliyeva[2]

[1]Institute of Physics of ANAS, Baku, av. H. Javid 131, AZ1143, Azerbaijan
[2]Sumgayit State University, Mahalla 43, Sumgait, AZ5008, Azerbaijan

THERMOELECTRIC FIGURE OF MERIT OF $TlIn_{1-x}Yb_xTe_2$ ($0 \le x \le 0.10$)

On the basis of the temperature dependences of the electrical conductivity σ, the Seebeck coefficient α and total thermal conductivity χ_{tot} in the solid solutions $TlIn_{1-x}Yb_xTe_2$ ($0 \le x \le 0.10$) thermoelectric figure of merit Z have been calculated in the temperature range of 80 – 1000 K. It was established that the maximum thermoelectric figure of merit $Z \approx 3\ K^{-1}$ reaches at 800 K for the solid solution of $TlIn_{0.9}Yb_{0.1}Te_2$. It is shown that the growth of Z is mainly due to increasing of the hole mobility and concentration of defects in the samples.

Key words: thermoelectric figure of merit, thermopower, solid solution, thermoelectric efficiency, thermal conductivity.

Introduction

Sufficiently intensive studies of electrical and thermoelectric properties of $TlIn_{1-x}Yb_xTe_2$ solid solutions [1 – 6] are connected primarily with the use of these materials in a variety of energy converters and, particularly in the manufacture of thermoelectric transducers operating at high temperatures.

According to [1] the solubility region of $TlYbTe_2$ in $TlInTe_2$ at room temperature is up to 10 %. Transition from $TlInTe_2$ to $TlIn_{1-x}Yb_xTe_2$ is accompanied by the increasing of hole concentration. The increasing of hole concentration is connected with arising of various structural imperfections, vacancies and anti-structure defects in these alloys; emerging intrinsic defects, mainly vacancies, are electroactive.

Synthesis of Samples

The synthesis of $TlInTe_2 - TlYbTe_2$ solid solutions was conducted by fusing the initial components taken in stoichiometric ratio. For the synthesis high purity materials (99.999 – 99.992 %) were used. According to the constitution diagram [1], a minor deviation from stoichiometry in any direction may result in heterophase samples. Therefore, the batch was added up to 0.05 mass % of tellurium over the stoichiometric requirement. The synthesis was carried out in the evacuated to 10^{-2} Pa, and sealed quartz ampoules in the following way: the temperature of the heater with quartz ampoules containing substance, was raised at a rate of 20 – 25 K/h up to 750 K. The samples were kept for 3 – 4 hours at this temperature and then were heated to 1100 K and kept for another 4 hours. After homogenization lasting for 20 – 25 hours at 1250 K the ampoule was moved with the speed of 2 – 3 mm/h through the zone with a temperature gradient of 50 K/cm.

The obtained ingots were cooled slowly (2 K/hr) to 1000 K and then down to 500 K at a rate of 4 K/h, following which the furnace was turned off. As a result, single crystals and large-block polycrystalline p-$TlIn_{1-x}Yb_xTe_2$ were obtained. The measurements were performed on polycrystalline samples.

Results and discussion

According to A.Ioffe [7], increasing the value of μ / χ_{ph} (χ_{ph} – phonon part of the heat conductivity, mobility of charge carriers) leads to an increase in Z. It means that a quantitative decrease in phonon scattering is fully compensated by an increase in scattering by defects [8]. As the wavelength of electrons is greater than that of phonons, it leads to total increase in μ / χ_{ph}. The thermoelectric peculiarities of the $TlIn_{1-x}Yb_xTe_2$ solid solutions show that these materials can provide rather high thermoelectric figure of merit.

It is known that the efficiency of a thermoelectric transducer is determined by the following formula:

$$Z = \alpha^2\sigma/\chi_{tot}, \quad (1)$$

here $\alpha^2\sigma$ – thermoelectric power, χ_{tot} – total heat conductivity.

The temperature dependences of the measured electrical conductivity σ and thermopower coefficient α for $TlIn_{1-x}Yb_xTe_2$ ($0 \le x \le 0.10$) solid solutions in the temperature range of 80 – 1000 K are shown in Fig. 1 and 2, respectively.

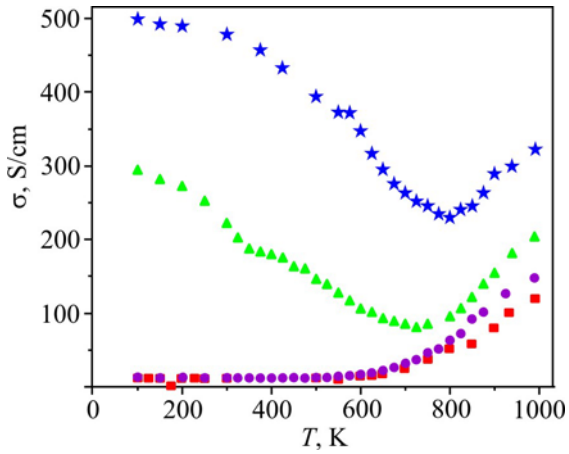

Fig. 1. Temperature dependences of electrical conduction in $TlIn_{1-x}Yb_xTe_2$;
■ – (x = 0), ● – (x = 0.02), ▲ – (x = 0.05), ★ – (x = 0.10).

As seen from Fig. 1, the $\sigma(T)$ dependences for different compositions of the solid solutions are essentially unlike. The region of intrinsic conduction for the initial compound $TlInTe_2$ begins at the temperature ~ 700K while the intrinsic region shifts towards higher temperatures with increase in relative content of ytterbium in $TlIn_{1-x}Yb_xTe_2$ solid solutions.

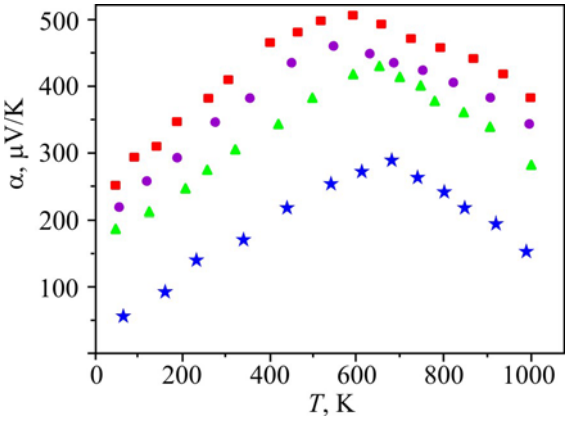

Fig. 2. Temperature dependences of thermopower coefficient in $TlIn_{1-x}Yb_xTe_2$. Markers describing experimental points correspond to the values of x as in Fig. 1.

As seen from Fig. 2, the $\alpha(T)$ dependences have similar character – $\alpha(T)$ grows linearly up to $T \sim 650$ K and then decreases in the intrinsic region – for all compositions and the sign of thermopower coefficients in the investigated temperature range is positive that proves that conduction occurs by holes in $TlIn_{1-x}Yb_xTe_2$ solid solutions.

Total heat conductivity is determined as the sum of phonon χ_{ph} and hole χ_h heat conductivities. Taking into account that $\chi_h = L_0\sigma T$, where $L_0 = (\pi^2/3)\cdot(k/e)^2 = 2.44\cdot10^{-8}$ W·Ω/K (we assume elastic scattering of holes [9]), we get

$$\chi_{tot} = \chi_{ph} + L_0\sigma T. \tag{2}$$

According to the theoretical calculations of G.I.Leibfried and E.Schlömann [10], at temperatures $T > \theta$ phonon conductivity is determined as

$$\chi_{ph} = \frac{12}{5}\cdot\left(\frac{k}{h}\right)^3\cdot\frac{\bar{M}\delta\theta^3}{\gamma_0^2 T} = 5,7\frac{\bar{M}\delta\theta^3}{\gamma_0^2 T} \tag{3}$$

here γ_0 is Grüneisen constant; it is usually on the order of 2 for the most solid state materials; θ is the Debye temperature, $\bar{M}$ is the average mass of the compound atoms, δ is cube root of the volume per atom. For the solid solutions of $TlIn_{1-x}Yb_xTe_2$ $\bar{M}$ can be calculated from $\bar{M} = \left[(1-x)\bar{M}_{TlInTe_2} + x\bar{M}_{TlInTe_2}\right]/2$, where $\bar{M}_{TlInTe_2} = 143.60$, $\bar{M}_{TlInTe_2} = 158.15$; $\theta = 200$K [11]; $\delta = \sqrt[3]{\Omega_0 / N}$, where $\Omega_0 = a^2c$ is the volume of the tetragonal unit cell, N is the number of atoms per unit volume [12]. By substituting the data into Eq. (3), we get the values for χ_{ph}, which are presented in the Table. The values of χ_{tot}, calculated on the basis of Eq. (2) are also given in the Table. Having the values of χ_{tot}, the values of Z can be calculated according to Eq. (1) (see the Table).

Table

Main parameters influencing the figure of merit for $TlIn_{1-x}Yb_xTe_2$ solid solutions

Samples	T	m_n^*	m_p^*	χ_{ph}	χ_{tot}	ΔW_i	Γ
$x = 0$	100	0.040	0.55	0.98	0.98		
	300	0.040	0.53	0.95	0.95		
	500	0.040	0.53	0.79	0.80		
	600	0.039	0.52	0.73	0.78		
	700	0.038	0.51	0,68	0.75		
	800	0.037	0.51	0.62	0.76		
	900	0.036	0.50	0.60	0.78		
$x = 0.02$	100	0.036	0.52	0.86	0.87	14	2.9
	300	0.036	0.52	0.82	0.83	16	
	500	0.035	0.51	0.64	0.67	29	
	600	0.035	0.51	0.60	0.66	50	
	700	0.034	0.50	0.58	0.68	58	
	800	0.033	0.49	0.54	0.70	69	
	900	0.032	0.48	0.47	0.74	78	
$x = 0.05$	100	0.034	0.48	0.76	0.83	29	7.1
	300	0.034	0.47	0.63	0.78	35	
	500	0.033	0.47	0.58	0.72	49	

Table (continued)

Samples	T	m_n^*	m_p^*	χ_{ph}	χ_{tot}	ΔW_i	Γ
	600	0.032	0.46	0.56	0.70	58	
	700	0.031	0.45	0.55	0.72	69	
	800	0.030	0.45	0.51	0.74	76	
	900	0.029	0.44	0.46	0.78	84	
$x = 0.10$	100	0.031	0.47	0.66	0.78	49	12.3
	300	0.031	0.47	0.42	0.75	133	
	500	0.030	0.46	0.37	0.76	143	
	600	0.029	0.46	0.32	0.78	183	
	700	0.028	0.46	0.30	0.85	200	
	800	0.027	0.45	0.29	0.88	237	
	900	0.026	0.45	0.24	0.94	255	

Here, m_n^* and m_p^* are effective masses of electrons and holes, correspondingly [16]; χ_{ph} 10^{-2} ($W \cdot cm^{-1} \cdot K^{-1}$) is coefficient of phonon thermal conductivity; $\chi_{tot} \cdot 10^{-2}$ ($W \cdot cm^{-1} \cdot K^{-1}$) is coefficient of total thermal conductivity; ΔW_i ($cm \cdot K \cdot W^{-1}$) is coefficient of thermal resistance; $\Gamma \cdot 10^3$ is parameter of disorder.

For taking into consideration the influence of disorders in the lattice thermal conduction we used the theory of Klemens [13], which takes into account scattering phonons by point defects in addition to the Umklapp scattering processes.

$$\chi_{ph} = \chi(\omega_0 / \omega_d)\text{arctg}(\omega_d / \omega_0), \tag{4}$$

where, $(\omega_0 / \omega_d) = k / (2\pi^2 \chi_V \omega_d A)$ and $A = (1/4V^2 N)\Gamma$. Here, χ_V is heat conductance of the stoichiometric compound in the absence of defects influence, $\omega_d = \theta \cdot k/\hbar$ is maximum frequency in the Debye model (Debye frequency), ω_0 is the frequency at which the value of relaxation times due to U-processes and scattering on defects are equal, v is average sound velocity in the crystal, N is the number of atoms in a unit volume, Γ is the parameter of disorder which is equal to

$$\Gamma = x(1-x)\left[(\Delta\overline{M} / \overline{M})^2 + \varepsilon(\Delta\delta/\delta)^2\right], \tag{5}$$

and takes into consideration simultaneous influence of a local change in density and elastic properties, ε – characterizes elastic properties of medium and $\Delta\overline{M} / \overline{M}$ is a relative change in mass when basic atoms are replaced by impurity atoms, which can be expressed as:

$$\Delta\overline{M}/\overline{M} = \frac{\overline{M}_{TlYbTe_2} - \overline{M}_{TlInTe_2}}{(1-x)\overline{M}_{TlInTe_2} + x\overline{M}_{TlYbTe_2}}$$

According to [14] a value of $\Delta\delta/\delta$ can be computed from the difference of parameters of elementary cell of matrix a_{mat} and impurity a_{imp} as:

$$\frac{\Delta\delta}{\delta} = \left(\frac{a_{TlInTe_2} - a_{TlYbTe_2}}{a_{TlInTe_2}}\right)\frac{\eta}{1+\eta}, \tag{6}$$

where, $\eta = (1+\nu)/\left[2(1-2\nu)\right]$, ν is Poisson`s ratio. All parameters necessary for calculations (v, ε, ν, θ, N etc.) were taken from [5, 11 – 12; 15] and linearly extrapolated for $TlIn_{1-x}Yb_xTe_2$ solid solutions as $P = (1-x)P_{TlInTe_2} + xP_{TlYbTe_2}$, where P is the necessary parameter for calculation thermal conductivity of the solid solutions.

It should be noted that the values of $\chi_{ph}(T)$ calculated by expressions (3) and (4) insignificantly differ. The values of the Γ parameter for various x in the $TlIn_{1-x}Yb_xTe_2$ are presented in the Table. From the comparison of stoichiometric compound $TlInTe_2$ with the solid solutions of $TlIn_{1-x}Yb_xTe_2$ it is clear that the parameter of disorder Γ changes by nearly 4.3 times at room temperature. It means that for other parameters being equal, thermal resistance arising in the solid solutions due to disorder must be much more than in $TlInTe_2$. It gives a reason that the determined values of Γ are true reflection of real relation of the basic factors responsible for additional scattering of phonons by point defects. It leads to the additional thermal resistance as in [14]:

$$\Delta W_i = 1/\chi_{ph} - 1/\chi_{\nu}.$$

Calculated data for ΔW_i are also presented in the Table.

Having all necessary data set in the Table allows us to analyze the thermoelectric peculiarities of the $TlIn_{1-x}Yb_xTe_2$ solid solutions more precisely for getting rather high thermoelectric figure of merit. The dependence of Z on the content of Yb in $TlIn_{1-x}Yb_xTe_2$ solid solutions for fixed temperatures 300, 500 and 800 K is described in Fig. 3. As is seen from the figure, Z increases both with temperature and the content of Yb in the solid solutions; Z has its minimal value for $x = 0$ at $T = 300$ K and maximal value for $x = 0.1$ at 800 K.

It is clear that increasing α, σ and decreasing χ_{lot} lead to an increase in the values of thermoelectric power ($\alpha^2\sigma$) and thermoelectric figure of merit (Z). Strong influence of the content of Yb atoms on Z in the investigated solid solutions is connected with high content of intrinsic defects in the materials [8].

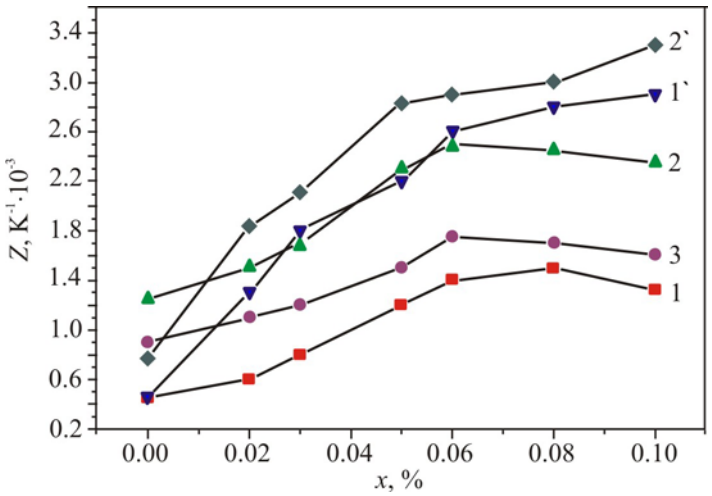

Fig. 3. The dependence of the thermoelectric figure of merit on the content of Yb in $TlIn_{1-x}Yb_xTe_2$ solid solutions at the temperatures ■ – 300 K, ● – 500 K and ▲ – 800 K.

The peculiarities of temperature dependence of χ_{ph} also may be explained by high concentration of defects in the materials [8]. It should be noted that for the $TlIn_{1-x}Yb_xTe_2$ solid solutions always $\chi_{ph} > \chi_h$, in spite of χ_h rising, but χ_{ph} decreasing with temperature in the temperature range where the material keeps its solid state.

As seen from Fig. 1 and 2, σ is decreasing, but α increasing in the temperature range of 300 – 700 K. Therefore the decreasing of σ with temperature in the abovementioned temperature range is connected to decreasing mobility of holes. The decreasing of hole mobility with temperature occurs mainly due to scattering of holes on thermal lattice vibrations and on defects according to $\mu_h \sim T^{-0.7}$ [1, 4]. The defects arise in the $TlIn_{1-x}Yb_xTe_2$ solid solutions mainly due to vacancies of In and *Yb*, and *Yb* atoms vacancies have more effect than In ones. The latter is connected with the large value of screening of *Yb* atoms ("crystal" ionic radii of $R(Yb^{3+}) = 100.8$ pm, $R(In^{3+}) = 94$ pm [16]) in the $TlIn_{1-x}Yb_xTe_2$. At the same time phonon-phonon and phonon-defect scattering effects bring to decreasing of χ_{ph} with temperature as $\chi_{ph} \sim T^{-1.2}$. With increasing of *Yb* atoms content in the solid solutions the values of χ_{ph} and index n in the expression of $\chi_{ph} \sim T^{-n}$ also decreases. As a result, for $x \ge 0.05$ we have the following relation $\mu_h/\chi_{ph} \sim T^{0.5}$. Thus, the increasing of Z up to ~ 700 K is due to linear increasing of $\alpha(T)$ (Fig. 2).

As seen from the Table, for the temperatures $T > 700$ K the rise in x leads to increasing of $\chi_{tot}(T)$. It is connected with high contribution of bipolar thermal conductivity (χ') into the total heat conductivity. So, for the temperatures $T > 700$ K its contribution to the total heat conductance is more than 40 %. Thus, at that case the expression (2) may be rewritten as $\chi_{tot} = \chi_{ph} + \chi'$, where $\chi' = (\sigma_n + \sigma_h) L_0 \cdot T$.

Conclusion

It is shown that the solid solutions of $TlIn_{1-x}Yb_xTe_2$ at $x \ge 0.05$ are promising materials for practical use in the thermoelectric transducers operating at high temperatures. The following features of those materials have been established:

- the wavelength of holes is greater than wavelength of phonons and this fact leads to higher values of Z;
- due to the peculiar defect structure of the $TlIn_{1-x}Yb_xTe_2$ solid solutions, the condition of $\mu_h / \chi_{ph} >> 1$ for the charge carriers and phonons is fulfilled, which resultы in gaining higher values for Z;
- the increasing of the level of submission of In atoms with *Yb* ones leads to an increase in the values of thermoelectric power ($\alpha^2\sigma$) and thermoelectric figure of merit (Z);
- the maximum thermoelectric figure of merit $Z \approx 3$ K^{-1} is reached at 800 K for the solid solution of $TlIn_{0.9}Yb_{0.1}Te_2$.

References

1. M.M. Zarbaliev, Substitutional Solid Solutions in the $TlInTe_2 - TlYbTe_2$ System, *Inorqanic Mater*. **35**, 560 – 564 (1999).
2. G.S. Orudzhev, E.M. Godzhaev, R.A. Kerimova, E.A. Allakhyarov, Band Structure and Optical Properties of Chain Compound $TlInTe_2$, *Physics of the Solid State* **48**(1), 40 – 43 (2006).
3. L.D. Ivanova, L.I. Petrova, Yu.V. Granatkina, T.E. Svechnikova, M.A. Korzhuev, and V.S. Zemskov, Graded Carrier Concentration Materials for Thermoelectric Coolers, *Inorganic Materials* **43** (12), 1291 – 1296 (2007).
4. M.M. Zarbaliev, Thermal Conductivity of Solid Solutions $TlInTe_2 - TlNdTe_2$ System, *Izv. NAN Azerb. Repub. " Fizika"* **3** (3), 35 – 38 (1997).
5. E.M. Godzhaev, R.A. Kerimova, Thermoelectric Properties of $TlIn_{1-x}Yb_xTe_2$ ($0.01 \le x \le 0.09$)

Crystals, *Inorganic Materials* **40** (11), 1153 – 1155 (2004).
6. M.M. Zarbaliev, A.M. Akhmedova, and U.M. Zarbaliyeva, Thermoelements on the Basis of Solid Solutions $TlIn_{1-x}Yb_xTe_2$, *Vestnik Baku.Gos.Univer*. **1**, 176 – 181 (2011).
7. A.F. Ioffe, *Semiconductor Thermoelements* (Moscow: AS USSR Publishing House, 1960), 188 p.
8. V.S. Oskotskiy, I.I. Smirnov, *Defects in Crystals and Heat Conductivity* (Leningrad, Nauka, 1972), 160 p.
9. F.F. Aliev, M.B. Dzafarov, A.A. Saddiniva, and E.M. Godzhaev, Increasing Thermoelectric Figure of Merit by Adding *Ag* and *Se* into Ag_2Se, *J. Thermoelectricity* 2, 42 – 48 (2010)
10. G.I. Leibfried, and E. Schlömann, Wärmeleitung in elektrisch isolierenden Kristallen. *Nachr. Akad. Wiss. Göttingen, Math. Physik. Klasse* **II a** (4), 71 – 74 (1954).
11. E.M. Godzayev, M.M. Zarbaliev. M.M. Kurbanov, A.B. Naqiev, and D.D. Bayramov, *Izv. AN SSSR ser. Neorgan. Mater*. **23**, 163 – 166 (1987).
12. V.A. Hajiyev, M.M. Kurbanov et al., *Inorganic Materials* **26** (6), 1325 – 1328 (1990)
13. P.G. Klemens, Thermal Resistance due to Point Defects at High Temperatures, *Phys. Rev*. **119** (2), 507 – 509 (1960).
14. B. Abeles, Lattice Thermal Conductivity of Disordered Semiconductor Alloys at High Temperatures, *Phys. Rev*. **131** (5), 1906 – 1911 (1963).
15. E.M. Kerimova, *Kristallofizika nizkorazmernix xalkogenidov* (Baku: Elm, 2012), 708 pp.
16. R.D. Shannon, Revised Effective Ionic Radii and Systematic Studies of Interatomic Distances in Halides and Halcogenides, *Acta Cryst.* **A32**, 751 – 767 (1976).

Submitted 22.08.2016

V.A. Romaka[1,2], L.P. Romaka[3], Yu.V. Stadnyk[3],
V.Ya. Krayovskyy[2], V.V. Romaka[2], A.M. Horyn[3]

[1]Ya. Pidstryhach Institute for Applied Problems of Mechanics and Mathematics, the National Academy of Sciences of Ukraine, 3-b, Naukova Str., Lviv, 79060, Ukraine;
[2]National University "Lvivska Polytechnika", 12, S. Bandera Str., Lviv, 79013, Ukraine;
[3]Ivan Franko National University of Lviv, 6, Kyryla and Mefodiya Str., Lviv, 79005, Ukraine

RESEARCH ON ELECTRICAL CONDUCTIVITY MECHANISMS OF THERMOELECTRIC MATERIAL BASED ON *n-ZrNiSn* DOPED WITH *Ga*

The crystalline and electronic structures, the temperature and concentration dependences of resistivity, the Seebeck coefficient and magnetic susceptibility of $ZrNiSn_{1-x}Ga_x$ thermoelectric material were investigated in the ranges: T = 80 – 400 K, x = 0.01 – 0.15. The electrical conductivity mechanisms of $ZrNiSn_{1-x}Ga_x$, were established which determine the simultaneously generated structural defects of both donor and acceptor nature (donor-acceptor pairs) in 4b crystallographic position of Sn atoms. The simultaneous generation of donor-acceptor pairs assures electrical neutrality and structural stability of thermoelectric material, as well as stability and reproducibility of its characteristics.
Key words: electronic structure, resistivity, Seebeck coefficient.

Introduction

Thermoelectric materials obtained by heavy doping of *n-TiNiSn, n-ZrNiSn* and *n-HfNiSn* intermetallic semiconductors with acceptor and/or donor impurities, demonstrate high values of thermoelectric figure of merit, possess high efficiency of thermal into electric energy conversion and are among the most studied today. Specifically, in $Ti_{1-x-y}Zr_xHf_yNiSn$ $(0 \le x \le 1;\ 0 \le y \le 1)$ [1] та $Ti_{0.5}Zr_{0.25}Hf_{0.25}Ti_{0.5}NiSn_{0.998}Sb_{0.002}$ materials [2] the value of *ZT* at temperature *T* = 800 K is ~ 1.4, which corresponds to the best performance of materials based on tellurides, clathrates, skutterudites, etc.

However, widespread introduction of these materials is prevented by incompletely studied transformation processes of crystalline and electronic structures at performance optimization by doping of the basic semiconductor which is accompanied with unpredicted generation of structural defects changing the electronic structure of material and its properties. Thus, donors of unknown origin appear on doping of *n-ZrNiSn* with acceptor impurities *M* = *Cr*, *Mn*, *Fe*, *Co* introduced into the structure by substitution of *Ni* atoms [3 – 5]. Generation in $ZrNi_{1-x}M_xSn$ of only structural acceptor defects looked logical, since the number of 3*d*-electrons in *Ni* exceeds that in *Cr*, *Mn*, *Fe* and *Co*. However, electrokinetic and galvanomagnetic investigations revealed the emergence of a large number of donors whose concentration grows with increasing the number of acceptors. In $TiNiSn_{1-x}Ga_x$ thermoelectric material obtained by doping of *n-TiNiSn* with *Ga* ($4s^24p^1$) atoms by substitution of *Sn* ($5s^25p^2$) there was also discovered a *simultaneous* generation of both acceptor defects (*Ga* possesses a smaller number of *p*-electrons than *Sn*) and donor defects of unknown origin whose concentration grows with increasing *Ga* content [6].

As is known, thermoelectric materials based on intermetallic semiconductors are synthesized by melting the batch of the source components with subsequent cooling of the melt, and this,

according to H. Mott [7], is one of the ways of obtaining amorphous solids and generates essential structural defects. Moreover, performance optimization by controlled doping of a semiconductor additionally generates defects of donor, acceptor or neutral nature, and in the energy gap there appear the respective energy states which determine its properties. Hence, according to fabrication technique, such thermoelectric material is a heavily doped and strongly compensated semiconductor (HDSC) [8]. Unpredicted emergence in materials of donor and/or acceptor defects both during synthesis and in the process of performance optimization causes an uncontrolled change in compensation ratio (the ratio between donors and acceptors), complicating technology for obtaining materials with specified characteristics.

B. Shklovsky and A. Efros showed that in the presence in semiconductor of a large number of unlike charged defects whose arrangement is of fluctuation nature, its electron structure is radically changed leading to fluctuation of potential relief and modulation of continuous energy bands [9, 10]. At low temperatures, a heavily doped crystalline semiconductor is a disordered system that reminds amorphous systems. Moreover, the authors of [10] proposed a scheme of a completely compensated semiconductor as a model of amorphous semiconductor (Fig. 1). The electron is regarded not in a periodic crystal field, but in a chaotic field of defects, and the potential energy of such a field cannot be considered small.

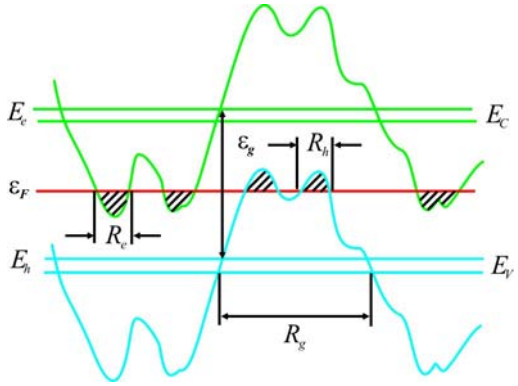

Fig. 1. Energy scheme of a completely compensated semiconductor [10]. The upper and lower lines – unperturbed states of conduction band bottom E_C and valence band peak E_V, the middle line – the Fermi level ε_F, E_e and E_h – percolation levels of conduction band and valence band. Wavy lines – the edge of bands modulated with electrostatic potential of charged defects. Occupied areas (drops) are shaded. R_e, R_h and R_g are the size of electron, hole drops and fluctuation.

Using approaches [9, 10] for the description of disordered systems, such as thermoelectric materials based on intermetallic semiconductors, an attempt was made to study the mechanisms of generation of donors in $ZrNiSn_{1-x}Ga_x$ thermoelectric material obtained by doping of *n-ZrNiSn* with *Ga* atoms by substitution of *Sn*, which makes semiconductor material HDSC. The results obtained will allow control of performance optimization of thermoelectric materials through adequate doping [11].

Investigation procedures

The object to be investigated included crystalline structure, electronic density distribution (DOS), electrokinetic, energy and magnetic characteristics of $ZrNiSn_{1-x}Ga_x$. The samples were synthesized in the laboratory of Institute for Physical Chemistry, Vienna University. The X-ray structural analysis (powder method) was used to obtain the data arrays (diffractometer Guinier-Huber image plate system, $CuK\alpha_1$), and Fullprof program [12] was employed for the calculation of

structural characteristics. The chemical and phase compositions of the samples were controlled by microprobe analyzer (EPMA, energy-dispersive X-ray analyzer). The electronic structure calculations were performed by the Korringa-Kohn-Rostoker (KKR) method in coherent potential approximation (CPA) and local density approximation (LDA) [13] with the use of Moruzzi-Janak-Williams exchange-correlation potential [14]. The accuracy of calculating the position of the Fermi level ε_F is ± 8 meV. The temperature and concentration dependences of the electrical resistivity (ρ) and the Seebeck coefficient (α) were measured with respect to copper and magnetic susceptibility (χ) (Faraday's method) of $ZrNiSn_{1-x}Ga_x$ samples in the ranges: $T = 80 – 400$ K, $N_A^{Ga} \approx 1.9 \cdot 10^{20}$ cm^{-3} ($x = 0.01$) – $2.9 \cdot 10^{21}$ cm^{-3} ($x = 0.15$) and magnetic field strength $H \leq 10$ кЕ.

Research on structural features of $ZrNiSn_{1-x}Ga_x$

A microprobe analysis of the concentration of atoms on the surface of $ZrNiSn_{1-x}Ga_x$ samples has established their conformity to the initial batch compositions, and X-ray phase and structural analyses have shown that X-ray diffraction patterns of samples up to composition $x = 0 – 0.15$ are indexed in structural type *MgAgAs* (spatial group [15]) and have no traces of other phases.

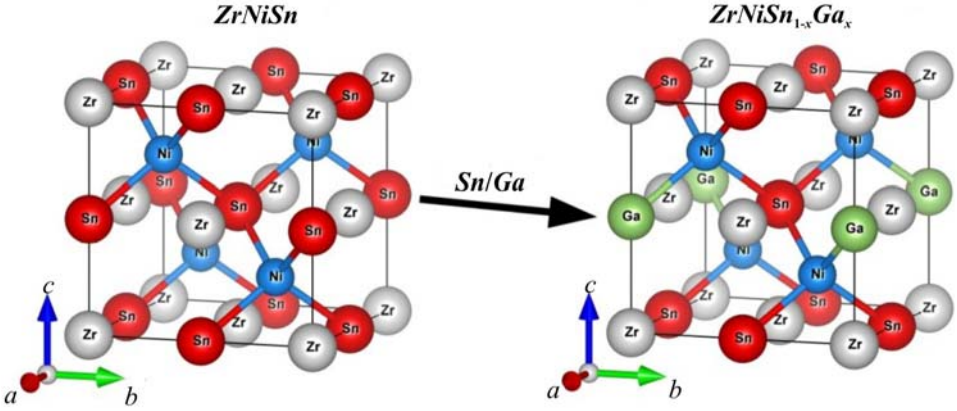

Fig. 2. Unit cell model of ZrNiSn compound (structural type MgAgAs, spatial group).

Thermodynamic calculations in the approximation of harmonic vibrations of atoms in the framework of density functional theory (DFT) have shown that a change in the values of free energy $\Delta G(x)$ (Helmholtz potential) passes through the minimum in the range of concentration $x \approx 0.4$ at the temperature of homogenizing annealing of samples $T = 1073$ K (Fig. 3*a*), pointing to solubility limit of *Ga* atoms in the structure of *ZrNiSn* compound. Thus, the compositions of studied samples $ZrNiSn_{1-x}Ga_x$, $x = 0 – 0.15$, are within the solubility limits, which is also evidenced by the absence of foreign phases in them.

In [16] it is shown that crystalline structure of *ZrNiSn* is disordered (local amorphization) due to partial, up to ~ 1 % ($z \approx 0.01$), occupancy by *Ni* ($3d^8 4s^2$) atoms of 4*a* position of *Zr* ($4d^2 5s^2$) atoms, which generates in a semiconductor structural defects of donor nature ("a priori doping"), as long as *Ni* has more *d*-electrons, and donor states ε_D[1] appear in the energy gap. The compound formula takes on the form $(Zr_{1-z}Ni_z)NiSn$. Structural investigations also showed that introduction of *Ga* atoms puts into order crystalline structure ("heals" structural defects): *Ni* atoms leave 4*a* position of *Zr* atoms, and the value $z \to 0$.

Taking into account smaller atomic radius of *Ga* ($r_{Ga} = 0.141$ nm) as compared to *Sn* ($r_{Sn} = 0.162$ nm), it would be logical to expect a reduction in the values of unit cell period $a(x)$ $ZrNiSn_{1-x}Ga_x$. However, as is seen in Fig. 3*b*, a change in $a(x)$ values is not monotonous, reflecting the processes of structural transformations caused by impurity atoms of *Ga*. Consider in detail these

changes, as they also cause alterations in the electronic structure and affect the properties of thermoelectric material. Attention will be called to the character of change in $a(x)$ values in the area $0 \le x \le 0.03$ (Fig. 3*b*).

As shown by structural investigations, in the process of introducing *Ga* atoms into *ZrNiSn* structure, in the concentration area $0 \le x \le 0.01$ its ordering takes place by displacement of small *Ni* atoms ($r_{Ni} = 0.124$ nm) from 4*a* position by larger *Zr* atoms ($r_{Zr} = 0.160$ nm) (Fig. 3*b*). Alongside with displacement of *Ni* atoms, there is a process of substitution in 4*b* position of large *Sn* atoms by smaller *Ga* atoms. Taking into account that the difference in atomic radii of *Zr* and *Ni* is $(r_{Zr} - r_{Ni}) = 0.036$ nm, and *Sn* and *Ga* $(r_{Sn} - r_{Ga}) = 0.021$ nm, a change in $a(x)$ values at concentration site $0 \le x \le 0.01$ will determine the process of displacement of *Ni* from 4*a* position by large *Zr* atoms that will cause the growth of dependence $a(x)$ (Fig. 3*b*). After *Ni* atoms are displaced from *Zr* position (structure ordering), a change in $a(x)$ values will determine occupancy by *Ga* atoms of *Sn* (4*b*) position, and they will decrease in concentration area $0.02 \le x \le 0.15$. Note that ordering of the structure of $ZrNiSn_{1-x}Ga_x$ thermoelectric material makes stable its operational characteristics during heating-cooling cycles.

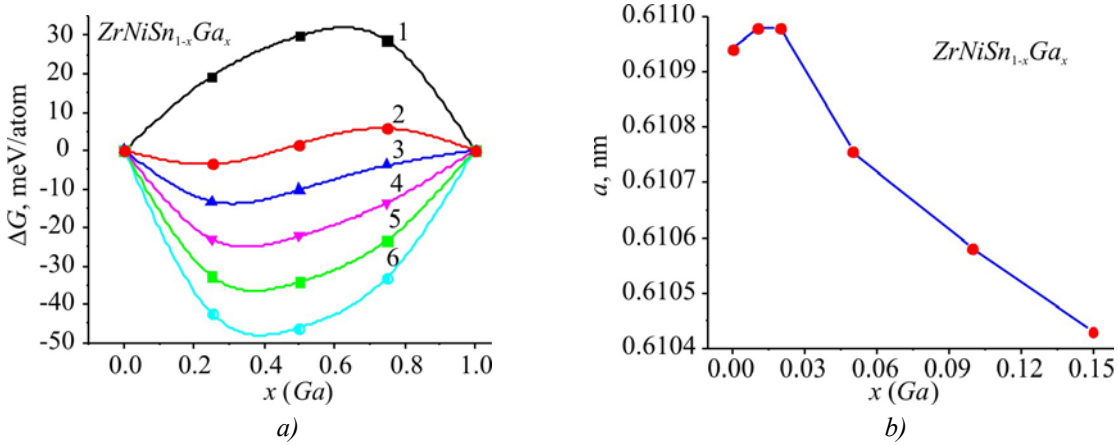

a) *b)*

Fig. 3. Change in the values of thermodynamic potential ΔG(x) at different temperatures (a): 1 – T = 0 K; 2 – T = 473 K; 3 – T = 673 K; 4 – T = 873 K; 5 – T= 1073 K; 5 – T = 1273 K and unit cell period a(x) (b) for $ZrNiSn_{1-x}Ga_x$.

Changes in crystalline structure of $ZrNiSn_{1-x}Ga_x$ in the process will necessarily lead to a respective transformation of electronic structure. In particular, if in *n-ZrNiSn* in the energy gap there are donor states ε_D^1 formed due to displacement of ~ 1 % of *Zr* atoms by *Ni* atoms [16], then structure ordering (displacement of *Ni* from *Zr* position (4*a*)) can lead to reduction in the number of structural defects of donor nature, and donor states ε_D^1 must disappear.

On the other hand, since *Ga* atom possesses one *p*-electron less than *Sn*, substitution of *Sn* atom by *Ga* generates in 4*b* position a defect of acceptor nature, which will cause the emergence in the energy gap of impurity acceptor states ε_A. The presence of a large number of acceptors and donors will affect the band structure of $ZrNiSn_{1-x}Ga_x$ which is bound to appear in the investigation of electrokinetic and energy characteristics.

Research on the electronic structure of $ZrNiSn_{1-x}Ga_x$

To predict the behaviour of the Fermi level ε_F, the energy gap ε_g and the kinetic characteristics of $ZrNiSn_{1-x}Ga_x$, the electronic density of states (DOS) was calculated (Fig. 4). Taking into account that according to the results of structural investigations the crystalline structure of $ZrNiSn_{1-x}Ga_x$, $x \ge 0.01$ is ordered, calculation of DOS was performed for the case of ordered structure version. As is

evident from Fig. 4, on introducing into *n-ZrNiSn* the lowest attainable in the experiment concentrations of *Ga* acceptor impurity, the Fermi level ε_F (dashed line) starts drifting from the bottom of the conduction band ε_C, spaced ~ 97.6 meV from it [3], toward the midgap ε_g and then to valence band ε_V, to cross it at certain concentrations of *Ga*.

Crossing of the midgap ($x \approx 0.025$) by the Fermi level ε_F and further motion toward the valence band will cause a change in semiconductor conduction type, and holes will become majority carriers. Note that apart from drift of the Fermi level ε_F due to a change in semiconductor compensation degree, there is also a reduction in the energy gap values.

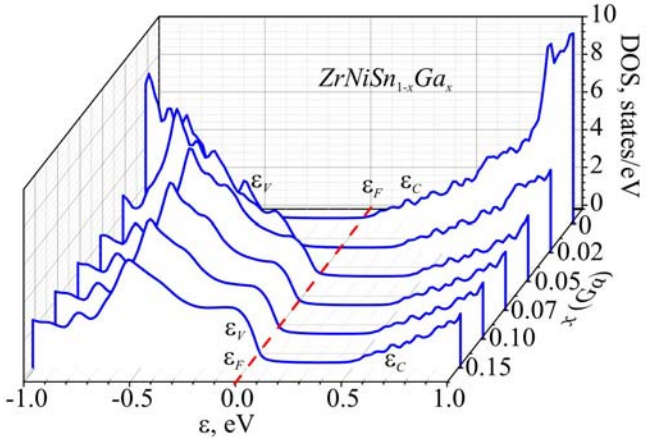

Fig. 4. Calculation of the electronic density of states for $ZrNiSn_{1-x}Ga_x$.

Thus, the results of calculation of the electronic density of states for $ZrNiSn_{1-x}Ga_x$, based on structural research data, prove the predicted acceptor nature of structural defects. The results of experimental research given below will show the conformity of calculated results to real processes occurring in thermoelectric material.

Research on the electrokinetic, energy and magnetic characteristics of $ZrNiSn_{1-x}Ga_x$

The temperature and concentration dependences of the electric resistivity ρ and the Seebeck coefficient α of $ZrNiSn_{1-x}Ga_x$ are presented in Fig. 5, 6. The dependences $\ln\rho(1/T)$ and $\alpha(1/T)$ $ZrNiSn_{1-x}Ga_x$ (Fig. 5) are typical for HDSC semiconductors, and the available activation areas point to several mechanisms of charge carrier transport [3, 7, 8]. The dependences $\ln\rho(1/T)$ are approximated using the known relationship [8]:

$$\rho^{-1}(T) = \rho_1^{-1} \exp\left(-\frac{\varepsilon_1^{\rho}}{k_B T}\right) + \rho_3^{-1}\left(-\frac{\varepsilon_3^{\rho}}{k_B T}\right), \quad (1)$$

where the first, high-temperature, summand describes activation of current carriers ε_1^{ρ} from the Fermi level ε_F to percolation level of continuous energy bands, and the second, low-temperature summand, – hopping conductivity ε_3^{ρ}. In turn, the temperature dependences of the Seebeck coefficient $\alpha(1/T)$ of $ZrNiSn_{1-x}Ga_x$ can be approximated using the following relationship [7]:

$$\alpha = \frac{k_B}{e}\left(\frac{\varepsilon_i^{\alpha}}{k_B T} - \gamma + 1\right), \quad (2)$$

where γ is parameter that depends on the nature of scattering. From the high-temperature area of the dependence $\alpha(1/T)$ the values of activation energy ε_1^{α} were calculated which, as shown in [3], are proportional to the amplitude of large-scale fluctuation of continuous energy bands (Fig. 1), and from the low-temperature area – the value of activation energy ε_3^{α} proportional to modulation amplitude of small-scale fluctuation of HDSC semiconductors [8 – 10].

The presence on the dependences lnρ(1/*T*) for all compositions of $ZrNiSn_{1-x}Ga_x$ of high-temperature activation areas testifies that the Fermi level ε_F is located in the forbidden zone from where thermal activation of current carriers occurs at percolation level. However, the obtained result contradicts the results of calculation of DOS for $ZrNiSn_{1-x}Ga_x$ (Fig. 4) which predicted crossing of the valence band at *Ga* concentration $x \approx 0.04$ by the Fermi level ε_F and by dielectric-metal transition which is the Anderson transition [7].

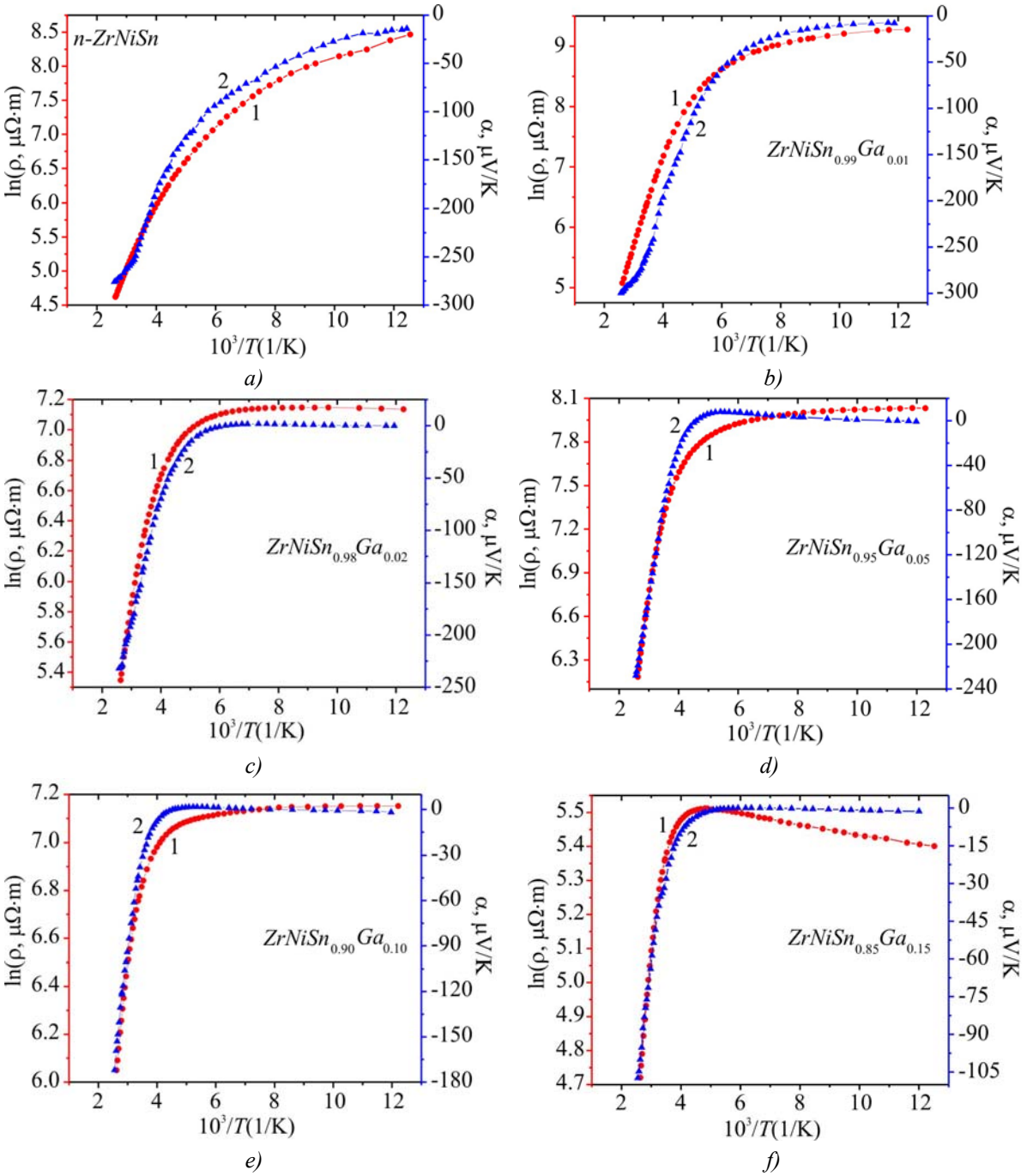

Fig. 5. Temperature dependences of resistivity lnρ(1/T) (1) and the Seebeck coefficient α(1/T) (2) of $ZrNiSn_{1-x}Ga_x$.

Assuming that in $ZrNiSn_{1-x}Ga_x$, as expected, only acceptor defects are generated, then at *Ga* concentration, for instance, $x = 0.15$ ($N_A^{Ga} \approx 3 \cdot 10^{21}$ cm^{-3}), the Fermi level ε_F must have long crossed the valence band. However, at high temperatures no conduction metallization takes place, which is

possible only on condition of simultaneous generation, along with acceptors, of donors of unknown origin which compensate acceptors, which will force the Fermi level ε_F to remain in the forbidden energy band, reflecting compensation ratio of $ZrNiSn_{1-x}Ga_x$.

It was predicted that substitution of *Ga* atoms for *Sn* atoms will be accompanied by generation in position 4*b* of acceptor structural defects and the emergence of impurity acceptor states ε_A. At the concentration of *Ga* atoms, when the Fermi level ε_F will cross the midgap and start approaching the percolation level of valence band, free holes will be the majority carriers. Such assumptions are logical, since at *Ga* concentration $x > 0.01$ the number of generated acceptors ε_A already exceeds the number of donors with the energy ε_D^1 in *n-ZrNiSn* (the number of *Ni* atoms in position of *Zr* (4*a*)).

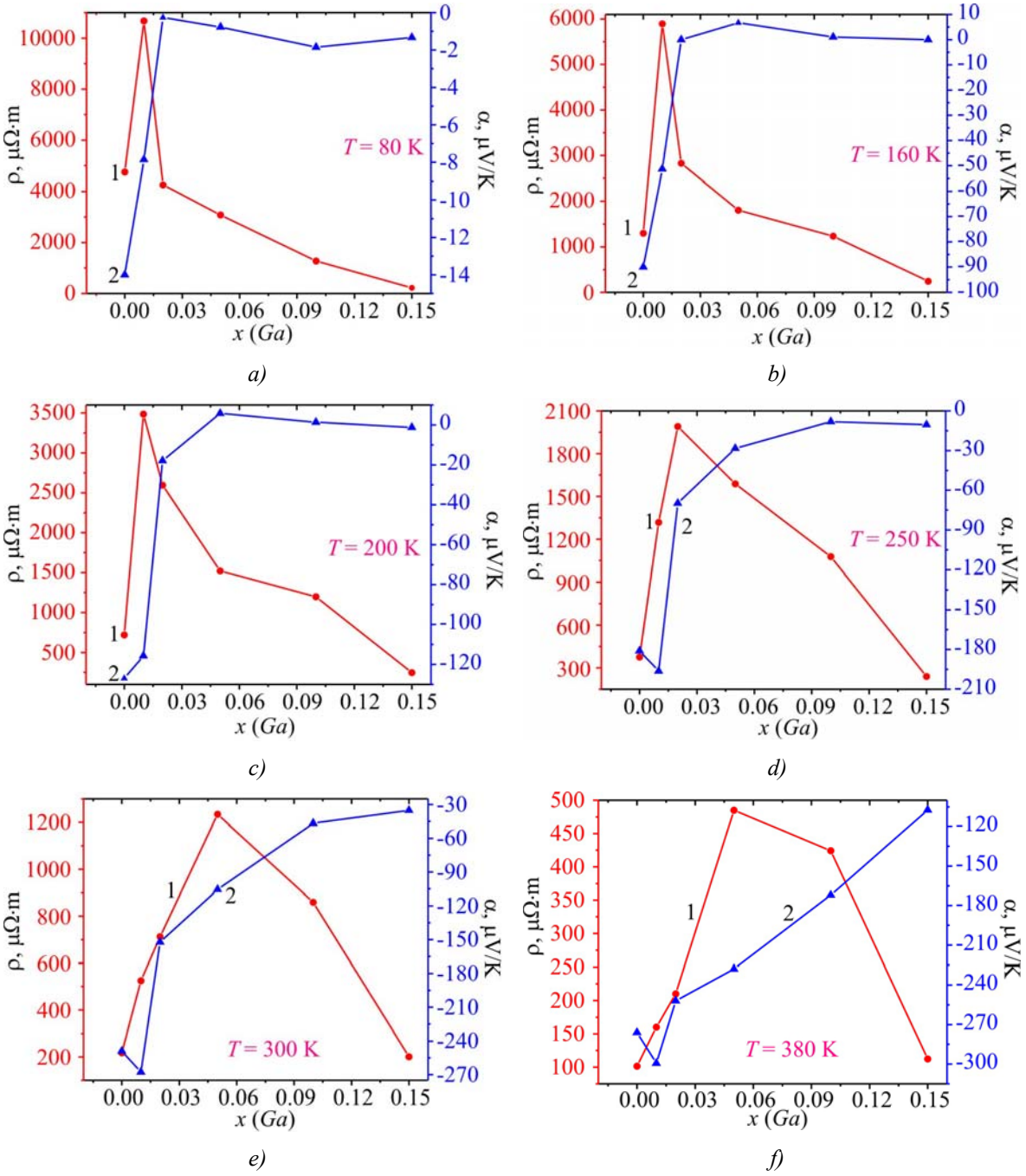

Fig. 6. Change in the values of resistivity ρ(x) and the Seebeck coefficient α(x) of $ZrNiSn_{1-x}Ga_x$ at different temperatures.

On the other hand, if we assume that *ZrNiSn* has no donor structural effects and the semiconductor is intrinsic (donor states ε_D^1 are absent), then with introduction of *Ga* atoms the values of electric resistivity $\rho(x)$ will decrease at all temperatures and concentrations due to the appearance and increase in the number of free holes in the valence band at ionization of acceptors ε_A. It is clear that the sign of the Seebeck coefficient in this case will be positive.

The fact that *Ga* atoms introduced into *n-ZrNiSn* generate structural defects of acceptor nature is demonstrated by the dependences of change in the values of resistivity $\rho(x, T)$ and the Seebeck coefficient $\alpha(x, T)$ over the entire concentration and temperature ranges (Fig. 6). To begin with, we will analyze the dependences $\rho(x)$ anda $\alpha(x)$ at temperature 80 K. Thus, introduction of the lowest in experiment *Ga* concentration drastically increases the value of resistivity $\rho(x)$ at $T = 80$ K from the values $\rho(x = 0) = 4751.1$ μΩ·m to $\rho(x = 0.01) = 10677.7$ μΩ·m. It can be assumed that a sample with concentration $x = 0.01$ is strongly compensated, as long as the number of generated acceptors is close to the number of donors in *n-ZrNiSn* [16]. Drastic growth of the dependence $\rho(x)$ in the area $x = 0 – 0.01$ is determined by two processes:

– decreasing the number of donor states ε_D^1 at ordering of $ZrNiSn_{1-x}Ga_x$ structure, when *Zr* atoms displace *Ni* atoms from 4*a* position, “healing” structural defects of donor nature;

– “freezing out” of free electrons toward energy gap to impurity acceptor states ε_A formed at substitution of *Sn* by *Ga*.

However, at concentration of $x > 0.01$ and $T = 80$ K, the values of resistivity $\rho(x)$ of $ZrNiSn_{1-x}Ga_x$ just as drastically decrease from $\rho(x = 0.02) = 4255.89$ μΩ·m to $\rho(x = 0.05) = 3079.7$ μΩ·m and $\rho(x = 0.10) = 1275.7$ μΩ·m, pointing to increase in the number of free current carriers. The maximum on the dependence $\rho(x)$ on introducing to *n*-type semiconductor of *Ga* acceptor impurity shows balancing of competing processes which determine conductivity mechanisms. Let us study the type and origin of current carriers which account for a decline in the dependence $\rho(x)$ (Fig. 6).

As is seen from Fig. 5 and 6, at temperature 80 K the sign of the Seebeck coefficient of $ZrNiSn_{1-x}Ga_x$ remains negative for all concentrations, and electrons are majority carriers. And this is despite the fact that concentration of generated structural defects of acceptor nature in a sample, for instance, $ZrNiSn_{1-x}Ga_x$, $x = 0.10$, exceeds by an order of magnitude the concentration of donors in *n-ZrNiSn*. This is possible only on condition of such depth of occurrence of acceptor states, that temperature 80 K is insufficient for the ionization of acceptors (overcoming by the hole of the energy barrier between the percolation level of valence band and the acceptor level ε_A).

With a rise in temperature ($T > 80$ K), the dependence $\rho(x)$ of $ZrNiSn_{1-x}Ga_x$ is transformed, showing changes in semiconductor electron structure. On the dependence $\rho(x)$ at temperature $T = 160$ K in the concentration range of $x \approx 0.06$ at first there appears a step which gradually grows into an extremum ($T = 300$ K) which with a rise in temperature $T = 380$ K is displaced into the region of higher concentrations $x \approx 0.08$. In so doing, the maximum on the dependence $\rho(x)$ in the range of $x \approx 0.01$ disappears.

Thus, at low concentrations of *Ga* acceptor impurity, the maximum on the dependence $\rho(x)$ of $ZrNiSn_{1-x}Ga_x$ at a concentration of $x \approx 0.01$ (Fig. 6) is related to the existence in the energy gap of donor states ε_D^1 (*Ni* atoms in 4*a* position of *Zr* atoms). At the concentration of acceptors which corresponds to the concentration of generated donors ($x \approx 0.01$) there is a depletion of donors, the values of electric resistivity are maximum, and semiconductor is strongly compensated. As long as the values of the Seebeck coefficient at temperature 80 K remain negative for all concentrations, this temperature is insufficient for complete ionization of acceptors.

Note that in $ZrNiSn_{1-x}Ga_x$, $x = 0.01$, the concentration of donors with the energy ε_D^1 in fact will be much lower than the number of generated acceptors with the energy ε_A, since at the lowest concentrations of *Ga* the structure is put into order, reducing the number of donors with the energy ε_D^1.

At the concentrations $x \geq 0.02$, when the number of generated acceptors exceeds the number of donors in *n-ZrNiSn*, with a rise in temperature from $T = 80$ K to $T = T_1^{inv}$ the sign of the Seebeck coefficient changes from negative to positive (Fig. 7). That is, for the samples of $ZrNiSn_{1-x}Ga_x$, $x \approx 0.02$ and $x \approx 0.05$, the temperature ~ 93 K is sufficient for the ionization of acceptors ε_A.

However, with a further rise in temperature, in the samples of $ZrNiSn_{1-x}Ga_x$, $x \approx 0.02$ and $x \approx 0.05$, 0, 10, at temperatures $T \approx 156$ K and $T \approx 216$ K, respectively, the sign of the Seebeck coefficient is unexpectedly changed from positive to negative at T_2^{inv} (Fig. 7), and electrons again become majority carriers. And this is despite the fact that concentration of generated acceptors in $ZrNiSn_{1-x}Ga_x$, $x > 0.01$, exceeds the number of donors with the energy ε_D^1 in *n-ZrNiSn* (the number of *Ni* in *Zr* position (4*a*)). Such a behaviour of the Seebeck coefficient in $ZrNiSn_{1-x}Ga_x$ at $T = T_2^{inv.}$ is possible under condition that in semiconductor, alongside with impurity acceptor states ε_A, donor states ε_D^2 are generated with their energy levels deeper than ε_D^1, and ionization of ε_D^2 donors and overcoming of a barrier to the percolation level of conduction band requires larger energies. It seems that in a semiconductor there are s*imultaneously* generated donor-acceptors pairs whose energy levels are arranged in the forbidden energy band.

The same conclusion is arrived at by analyzing the behaviour of $\rho(x)$ of $ZrNiSn_{1-x}Ga_x$ at different temperatures. As long as the extremum on the dependence $\rho(x)$ of $ZrNiSn_{1-x}Ga_x$ is a result of balancing of competing processes in semiconductor electronic structure, with a rise in temperature the disappearance of maximum $\rho(x)$ at low concentrations of *Ga* ($x \approx 0.01$) and the emergence of a new extremum $\rho(x)$ in the range of concentrations $x \approx 0.06$ unambiguously points to the existence of donor states ε_D^2 whose depth of occurrence is larger than ε_D^1. Indeed, at concentrations $x \geq 0.02$ and temperatures whose values are insufficient for ionization of donor ε_D^2, the concentration of acceptors in $ZrNiSn_{1-x}Ga_x$ exceeds the concentration of donors, and the sign of the Seebeck coefficient is predictably positive. However, with a rise in temperature at $T \geq T^{inv.}$ there begins ionization of donors ε_D^2, drastically increases the number of free electrons which become majority carriers, which is indicated by the negative values of the Seebeck coefficient (Fig. 7).

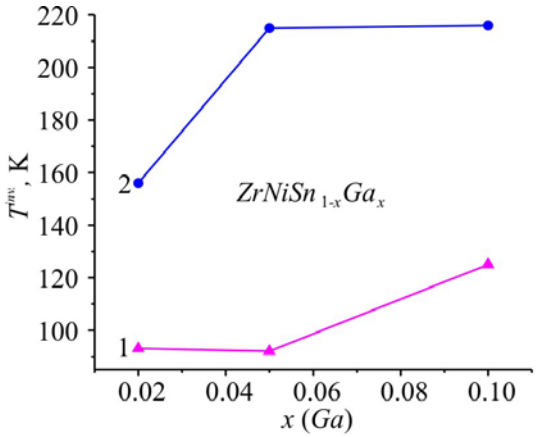

Fig. 7. Change in the values of inversion temperature $T^{inv.}$: 1 – $T_1^{inv.}$ (change of sign from negative to positive); 2 – $T_2^{inv.}$ (change of sign from positive to negative) $ZrNiSn_{1-x}Ga_x$.

On the other hand, the larger number of acceptors is generated in $ZrNiSn_{1-x}Ga_x$, the larger energies (higher temperatures) are needed for the number of ionized donors ε_D^2 to exceed the number of ionized acceptors ε_A. We can *assume* that in $ZrNiSn_{1-x}Ga_x$ to assure structural *stability* and electroneutrality *principle,* in 4*b* position structural defects of both acceptor and donor nature are *simultaneously* generated whose concentration grows with increasing *Ga* content. In this case the formula of semiconductor thermoelectric material is of the form $(Zr_{1-z}Ni_z)Ni\ Sn_{1-x-y}Ga_x$, where *y* is concentration of vacancies in 4*b* position of *Sn* atoms.

Analysis of behaviour of the energy characteristics of $ZrNiSn_{1-x}Ga_x$, in particular, a change in the values of activation energy $\varepsilon_1^{\rho}(x)$ and modulation amplitude of continuous energy bands ε_1^{α} also shows that acceptors and donors are simultaneously generated in semiconductor (Fig. 8). Thus, in *n-ZrNiSn* the value of energy $\varepsilon_1^{\rho}(x = 0) = 97.6$ meV shows the energy gap between the position of the Fermi level ε_F and percolation level of conduction band. Doping of *n*-type semiconductor with *Ga* acceptor impurity increases compensation ratio, and the Fermi level ε_F goes deeply into forbidden band at the distance of $\varepsilon_1^{\rho}(x = 0.01) = 138.8$ meV and $\varepsilon_1^{\rho}(x = 0.02) = 153.2$ meV. Taking into account that at high temperatures the sign of the Seebeck coefficient remains negative, we can conclude that the values of activation energies $\varepsilon_1^{\rho}(x = 0.01)$ and $\varepsilon_1^{\rho}(x = 0.02)$ represent the energy barrier to percolation level of conduction band. Recall that the value of activation energy $\varepsilon_1^{\rho}(x)$ is calculated exactly from the high-temperature activation area of the dependence $\ln\rho(1/T)$ (Fig. 5).

The negative values of the Seebeck coefficient and decrease in the values of $\varepsilon_1^{\rho}(x)$ at concentrations $x > 0.02$ from $\varepsilon_1^{\rho}(x = 0.05) = 139.5$ meV to $\varepsilon_1^{\rho}(x = 0.10) = 111.2$ meV and $\varepsilon_1^{\rho}(x = 0.15) = 91.3$ meV testify that the Fermi level ε_F has been reversed and is again moving toward conduction band. It means that in $ZrNiSn_{1-x}Ga_x$ there appear electrons of unknown origin, and this on doping of *n*-type semiconductor with acceptor impurity is possible only on condition of a simultaneous generation of donors ε_D^2 whose concentration is not lower than that of acceptors.

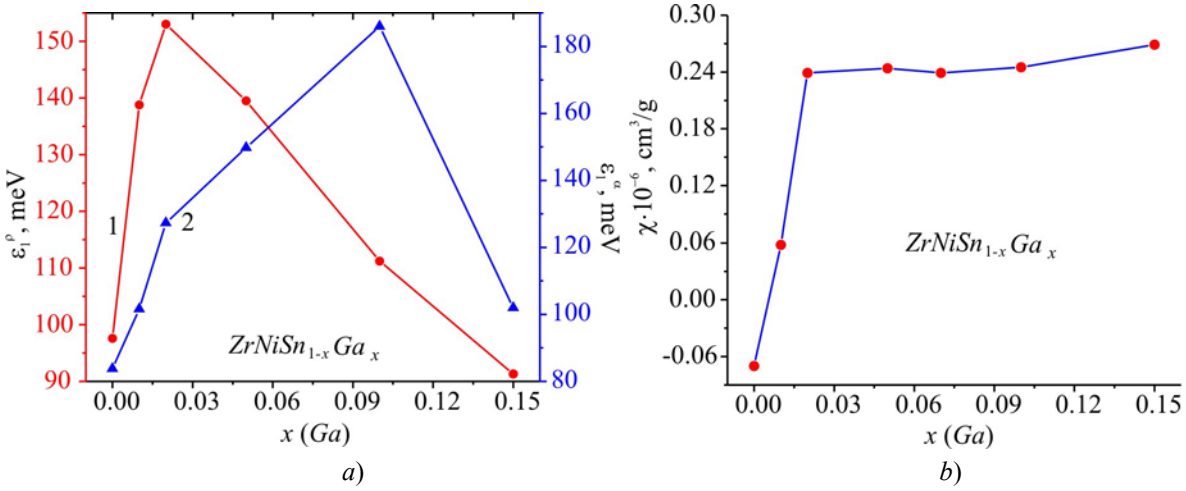

Fig. 8. Change in the values of activation energies $\varepsilon_1^{\rho}(x)$ (1) and $\varepsilon_1^{\alpha}(x)$ (2) (a) and magnetic susceptibility $\chi(x)$ (b) of $ZrNiSn_{1-x}Ga_x$.

On the other hand, simultaneous generation in $ZrNiSn_{1-x}Ga_x$ of donors and acceptors changes compensation ratio and the value of modulation energy of continuous energy bands of HDSC semiconductor [3, 8]. Fig. 8 shows a change in the values of activation energy $\varepsilon_1^{\alpha}(x)$ which is proportional to modulation amplitude of continuous energy bands of $ZrNiSn_{1-x}Ga_x$. We can see that in the case of *n-ZrNiSn* the modulation amplitude is $\varepsilon_1^{\alpha}(x = 0) = 83.8$ meV. Introduction into

n-type semiconductor of the lowest concentration of *Ga* acceptor impurity ($x = 0.01$) drastically increases compensation ratio, which is indicated by increase in the values of modulation amplitude to $\varepsilon_1^{\alpha}(x = 0.01) = 101.6$ meV.

Further increase in the concentration of acceptors in a semiconductor where electrons are majority carriers due to simultaneous generation of donors increases compensation ratio and modulation amplitude of continuous energy bands from $\varepsilon_1^{\alpha}(x = 0.02) = 127.3$ meV to $\varepsilon_1^{\alpha}(x = 0.05) = 149.8$ meV and $\varepsilon_1^{\alpha}(x = 0.10) = 186$ meV. A decline in the dependence $\varepsilon_1^{\alpha}(x)$ at concentrations of $ZrNiSn_{1-x}Ga_x$, $x > 0.10$ shows that the number of ionized donors increases faster than that of acceptors, so compensation ratio is reduced. At large concentrations of generated donor-acceptor pairs $ZrNiSn_{1-x}Ga_x$, $x = 0.15$, when wave functions of localized states ε_D^2 overlap, there is metallization of conductivity (absence of low-temperature activation area on the dependence $\ln\rho(1/T)$ (Fig. 5).

Of interest are the results of studies on magnetic susceptibility χ of $ZrNiSn_{1-x}Ga_x$ (Fig. 8*b*) which confirm the conclusion made on the simultaneous generation of acceptor and donor defects. Investigations showed that the samples of $ZrNiSn_{1-x}Ga_x$, $x>0.01$, are Pauli paramagnetics wherein magnetic susceptibility χ is determined exceptionally by electronic gas and is proportional to density of states at the Fermi level $g(\varepsilon_F)$. As is seen from Fig. 8*b*, the dependence $\chi(x)$ at $x > 0.03$ drastically changes the slope, achieves plateau and scarcely changes up to $x = 0.15$. That is, increase in the concentration of acceptor impurity and possible increase in the concentration of free holes scarcely changes the values $g(\varepsilon_F)$. Such a behaviour of $\chi(x)$ ($\chi \sim g(\varepsilon_F)$) is possible only on condition of appearance in $ZrNiSn_{1-x}Ga_x$ of opposite-sign current carriers of the concentration close to holes as a result of generation of donor-acceptor pairs which will account for density of states permanence at the Fermi level $g(\varepsilon_F)$. Note that *n-ZrNiSn* semiconductor is not Pauli paramagnetic, but a weak diamagnetic, which is evidenced by the negative values of magnetic susceptibility: $\chi(x = 0) = -0.07$ cm^3/g. Therefore, we cannot attribute growth of the dependence $\chi(x)$ in the concentration area $x = 0 - 0.01$ to increase in the values $g(\varepsilon_F)$.

Thus, the results of structural, electrokinetic, energy and magnetic investigations of $ZrNiSn_{1-x}Ga_x$ allow speaking about a complicated mechanism of simultaneous generation in a crystal of acceptor and donor structural defects and making assumptions regarding their nature. However, they cannot definitely prove the existence of this or other mechanism of generation of donor-acceptor pairs. The following mechanism will be proposed below.

Refinement of crystalline and electronic structures of $ZrNiSn_{1-x}Ga_x$

Based on the fact that the above results of research on $ZrNiSn_{1-x}Ga_x$ did not provide any answer concerning the mechanisms for generation of structural defects of various nature, let us solve the inverse problem. It is known that for the calculation of electron energy in the first Brillouin zone one should know spatial arrangement of atoms (or their absence – vacancies) in the sites of the unit cell. On the other hand, the slightest structural changes modify local symmetry and the electronic density of states. In this case the adequacy of the results of calculation of the electronic density of states distribution and the results of experimental research on the energy characteristics of semiconductor material specifies that the model of its crystalline structure is adequate to spatial arrangement of atoms in a real material. Exactly for this reason the results of electronic structure calculation as compared to the results, for instance, of electrokinetic or energy characteristics, yield information on the real structure of crystal which is beyond reach of X-ray methods.

Having the experimental results of the Fermi level drift velocity as activation energy $\varepsilon_1^{\rho}(x)$

$ZrNiSn_{1-x}Ga_x$ (Fig. 8*a*, curve 1), the compensation ratio (the ratio between donors and acceptors) was sought for, which will set the velocity of the Fermi level ε_F maximum close to $\varepsilon_1^{\rho}(x)$ (Fig. 9).

Calculations of the electronic density distribution DOS were performed almost for all variants of atoms arrangement in the unit cell sites, and the degree of occupancy of all positions by intrinsic and /or foreign atoms, as well as the presence of vacancies in them. It turned out that the most acceptable is the variant of atoms arrangement in the ordered but deformed structure, wherein the following changes took place:

a) crystalline structure of *n-ZrNiSn* is disordered (local amorphization) due to partial occupancy, up to ~ 1 % ($z \approx 0.01$), by *Ni* atoms of position 4*a* of *Zr* atoms, which generates in a semiconductor structural defects of donor nature (semiconductor formula $(Zr_{1-z}Ni_z)NiSn$);

b) introduction of *Ga* atoms puts structure into order and reduces the number of donor defects: *Ni* atoms leave position 4*a* of *Zr* atoms ($z \to 0$), and semiconductor formula acquires the form $(Zr_{1-z}Ni_z)Ni\ Sn_{1-x}Ga_x$;

c) occupancy by *Ga* impurity atoms of crystallographic position 4*b* of *Sn* atoms generates structural defects of acceptor nature;

d) generation and increase of the number of vacancies (*y*) in position 4*b* of *Sn* atoms (end formula is transformed into $(Zr_{1-z}Ni_z)Ni\ Sn_{1-x-y}Ga_x$).

Item *d*), being the result of formal mathematical calculations, has a profound physical meaning, as long as *simultaneous* generation of donor-acceptor pairs assures electroneutrality *principle* in position *4b* and *stability* of thermoelectric material structure.

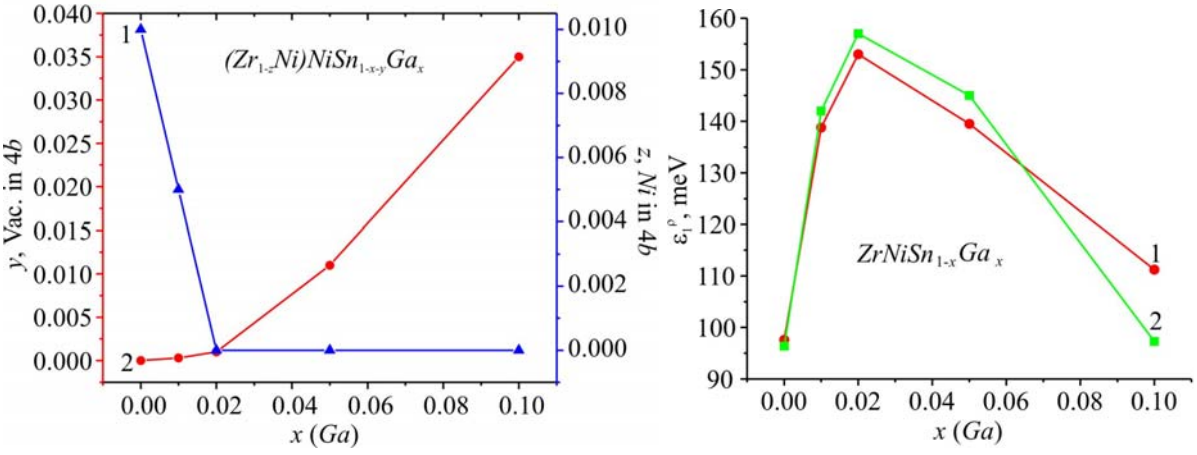

a) *b*)

Fig. 9. Dynamics of change in the concentration of Ni atoms (z) in position 4a of Zr atoms (1) and vacancies (y) in position 4b of Sn atoms (2) (a) and experimentally obtained (1) and calculated (2) dependence of activation energy ε_1^{ρ} (b) for $ZrNiSn_{1-x}Ga_x$.

Fig. 9*a* shows the results of calculation of the dynamics of change in all structural defects at heavy doping of *n-ZrNiSn* with *Ga* acceptor impurity, which provides within the error of calculations the proximity of calculated velocity of the Fermi level ε_F (Fig. 9*b*, curve 2) to that obtained from the high-temperature areas of dependences $\ln\rho(1/T)$ (Fig. 9*b*, curve 1).

Based on the obtained results of spatial arrangement of atoms in $ZrNiSn_{1-x}Ga_x$, the electronic density of states distribution DOS was calculated, which adequately shows the compensation ratio of semiconductor material (Fig. 10). In particular, we can see the distinctions in the energy gap and the

position of the Fermi level ε_F for the ordered version of *ZrNiSn* structure and in the presence of "local amorphization" in *n-ZrNiSn* semiconductor.

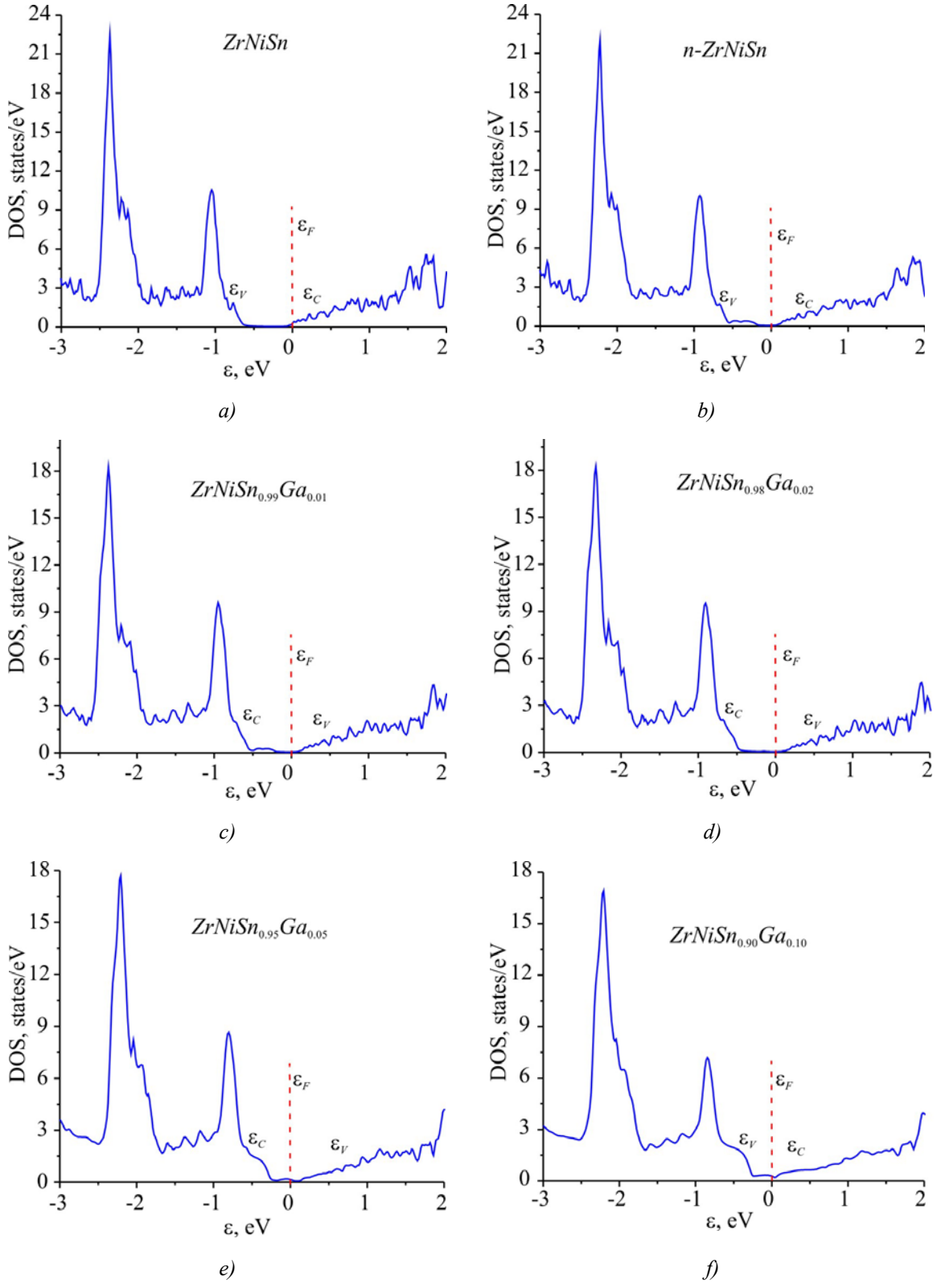

Fig. 10. Calculation of the electronic density of states DOS for different concentrations of $ZrNiSn_{1-x}Gax$.

From Fig. 10 it is also seen that the Fermi level ε_F of $ZrNiSn_{1-x}Ga_x$ for all concentrations of *Ga*

acceptor impurity changes its location with respect to percolation level of conduction band, which corresponds to negative values of the Seebeck coefficient (Fig. 5*b*) and is consistent with the results of electrokinetic characteristics of material.

Conclusions

Thus, as a result of integrated research on the crystalline and electronic structures, the kinetic and magnetic characteristics of $ZrNiSn_{1-x}Ga_x$ thermoelectric materials, the mechanisms for simultaneous generation of the acceptor and donor structural defects (donor-acceptor pairs) have been identified that change the compensation ratio and determine the electric conductivity mechanisms of material. The investigated $ZrNiSn_{1-x}Ga_x$ semiconductor is a promising thermoelectric material, and crystalline structure orderliness is key to stability and reproducibility of characteristics.

The work was performed in the framework of grants of Ministry of Education and Science of Ukraine, № 0115U003257 and № 0114U005464.

References

1. M. Gurth, G. Rogl, V.V. Romaka, E. Bauer, and P. Rogl, Thermoelectric High ZT Half-Heusler Alloys $Ti_{1-x-y}Zr_xHf_yNiSn$ ($0 \le x \le 1$; $0 \le y \le 1$), *Acta Materialia* 104, 210 – 222 (2016).
2. M. Schwall, B. Balke, Phase Separation as a Key to a Thermoelectric High Efficiency, *Phys. Chem. Chem. Phys* **15**(6), 1868 – 1872 (2013).
3. V.A. Romaka, V.V. Romaka, and Yu.V. Stadnyk, *Intermetallic Semiconductors: Properties and Application* (Lviv:Lvivska Polytechnika, 2011), 488 p.
4. V.A. Romaka, M.G. Shelyapina, Yu.K. Gorelenko, D. Fruchart, Yu.V. Stadnyk, L.P. Romaka, and V.F. Chekurin, Special Features of Conductivity Mechanisms in Heavily Doped *n-ZrNiSn* Intermetallic Semiconductors, *Semiconductors* **40**(6), 655 – 661(2006).
5. V.A. Romaka, Yu.V. Stadnyk, D. Fruchart, L.P. Romaka, A.M. Goryn, Yu.K Gorelenko, T.I. Dominuk Features of Structural, Electron-Transport, and Magnetic Properties of Heavily Doped *n-ZrNiSn* emiconductor: *Fe* Acceptor Impurity, *Semiconductors* **43**(3), 278 – 284 (2009).
6. V.A. Romaka, P. Rogl, L.P. Romaka, Yu.V. Stadnyk, V.Ya. Krayovskyy, D. Kaczorowski, and A.M. Horyn, Features of Structural, Energy and Kinetic Characteristics of $TiNiSn_{1-x}Ga_x$ Thermoelectric Material, *J.Thermoelectricity* 3, 24 – 33 (2016).
7. B.I. Shklovsky, *Electron Properties of Doped Semiconductors* (Moscow: Nauka, 1979), 416 p.
8. L.I. Anatychuk, *Thermoelements and Thermoelectric Devices* (Kyiv: Naukova Dumka, 1979), 768 p.
9. H. Mott, T.Davis, *Electronic Processes in Non-Crystalline Substances* (Moscow: Mir, 1982), 368p.
10. B.I. Shklovsky, A.L. Efros, Transition from Metallic to Activation Conduction in Compensated Semiconductors, *JETP* **61**(2), 816 – 825 (1971).
11. B.I. Shklovsky, A.L. Efros, Fully Compensated Crystalline Semiconductor as a Model of Amorphous Semiconductor, *JETP* **62**(3), 1156 – 1165 (1972).
12. T. Roisnel, J.Rodriguez-Carvajal, WinPLOTR: a Windows Tool for Powder Diffraction Patterns Analysis, *Mater. Sci. Forum, Proc. EPDIC7* 378-381, 118 – 123 (2001).

13. M. Schruter, H. Ebert, H. Akai, P. Entel, E. Hoffmann, and G.G. Reddy, First-Principles Investigations of Atomic Disorder Effects on Magnetic and Structural Instabilities in Transition-Metal Alloys, *Phys. Rev. B* **52**, 188 – 209 (1995).
14. V.L. Moruzzi, J.F. Janak, and A.R. Williams, *Calculated Electronic Properties of Metals* (NY: Pergamon Press, 1978), 348 p.
15. V.V. Romaka, L.P. Romaka, V.Ya. Krayovsky, and Yu.V. Stadnyk, *Stannides of Rare-Earth and Transition Metals* (Lviv: Lvivska Polytechnika Publ., 2015), 224 p.
16. V. Romaka, P. Rogl, L. Romaka, Yu. Stadnyk, A. Grytsiv, O. Lakh, and V. Krayovsky, Peculiarites of Structural Disorder in *Zr*- and *Hf*- Containing Heusler and Half-heusler Stannides, *Intermetallics* 35, 45 – 52 (2013).

Submitted 02.09.2016

V.P. Shafranyuk

V.P. Shafranyuk

Higher Educational Establishments of Ukraine
Bukovinian State Medical University, 2 Teatralna Square,
Chernivtsi, 58000, Ukraine

STUDY OF DAMAGED LAYER DEPTH IN THERMOELECTRIC MATERIALS BY X-RAY DIFFRACTION INTERFEROMETRY

The results of investigation of the damaged layer depth after machining of the surface of thermoelectric materials with diamond abrasive powders of different size are presented. A refined model of the damaged layer consisting of: a) a relief zone with polycrystalline structure, from which the kinematic scattering as large as (0.2 – 0.5 d, d – abrasive material grain size) is observed; b) a zone of microcracks, packing defects and dislocation ensembles of (3 – 4 d); c) an elastic deformation zone with an area of (4 – 5 d). This elastic deformation zone is quite long, even during the removal of the first two zones the residual stresses in the crystals still remain.
Key words: X-ray interferometer, moire patterns, X-ray topograms, thermoelement, damaged layer.

Introduction

One of the most important development trends of modern thermoelectricity is microminiaturization of thermoelectric modules which is related to essential reduction of the height of legs. To achieve high thermal and electric parameters of modules with a reduced height of legs, it is necessary to assure minimal contact resistance and high adhesion of metal coating on thermoelectric material. Therefore, the formation of silicon wafers with improved properties in a thin subsurface layer is a relevant task. The depth of the damaged surface (the defective layer depth) of semiconductor materials is an important parameter that needs to be controlled in process sizing. The knowledge of the damaged layer depth makes it possible to optimize processing of semiconductor materials and to choose the best of them, which in its turn will increase their yield. During the semiconductor crystal surface machining in the contact zone with the grains of the diamond abrasive material, the destruction of the original perfect structure and the formation of the damaged subsurface layer take place. Depending on the process conditions of processing, elastic and plastic deformations, microcracks, brittle fracture, local heat treatment and even polymorphic transformations may occur in the subsurface layer [1 – 6]. Naturally, the physical and mechanical properties of the damaged layer substantially differ from those of the original crystal. The study of the structure and depth of the damaged layer is usually performed using the X-ray topography, optical and electron microscopy methods.

As a result of the conducted researches, many models of the damaged layer were proposed, which generally could be reduced to the following: the damaged layer consists of a polycrystalline zone, a zone of microcracks and dislocation clusters, a dislocation zone and an elastic deformation area [1, 2]. It is worth noting that in many papers the dimensions of these zones significantly differ and usually depend on the accuracy of the research methods selected by the authors.

The X-ray diffraction moire (RDM) method, which is highly sensitive to the crystal lattice distortions [7 – 10], can greatly add and expand the information on the structure and level of sophistication of the damaged layer. It can also help to study the homogeneity of *Bi-Te* or *Ge-Si* based thermoelectric materials with the use of phase moiré topography. Therefore, the study of the damaged layer structure, which occurred during the *Si* surface machining, was conducted in this paper by RDM.

Research methods

The study was conducted on integral LLL-interferometers, made of perfect dislocation-free *Si* single crystals, grown by Czochralski method in the direction [111]. Input surfaces of the interferometers corresponded to crystallographic planes (111). The machining of surfaces of the interferometer analyzer (111), $(\bar{1}10)$, $(11\bar{2})$ was carried out using emery powders M5, M10, M28, and after the abrasive cutting - using an internal cutting edge of the disc. X-ray interferograms and topograms obtained in *CuKα* are radiation ones using reflection $(\bar{2}20)$. The annealing of interferometers was conducted in vacuum 10^{-2} Pa at the temperature of 700 – 1173 K.

Research results

It is known that during the surface machining with a free abrasive material, the structure and depth of the damaged layer are determined by physical and mechanical properties of the processed crystal and abrasive grains. The study of the structure defects, which occurred on different surfaces of semiconductor single crystals, was carried out repeatedly by optical and electron microscopy and X-ray diffraction topography methods [1 – 6]. It can be observed that the plastic deformation generally occurs during the surface polishing, and the brittle fracture takes place during cutting and polishing processes.

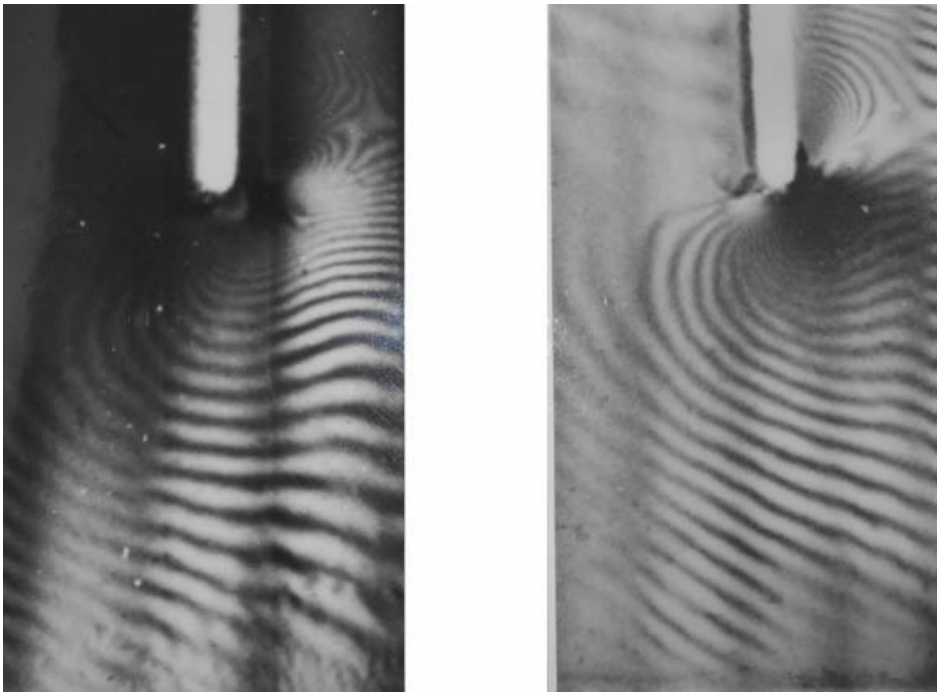

a) *b)*

Fig. 1. Moire pattern of analyzing crystal cut, reflection $(\bar{2}20)$: a) before etching; b) after etching ×12.

Interferometers were previously studied. The interferometer, which was used for the analyzing crystal cut and aperture, had a rotational moire, which corresponds to the lower part of Figure 1, 2*b*. Experimental diffraction moire patterns obtained with the interferometer cut and aperture made by an inner side of the diamond disc perpendicular to the analyzer plane (111), are shown in Fig. 1, 2, received in *CuK*α - radiation using reflections ($\bar{2}20$). The moire patterns represent predominantly rotational moire.

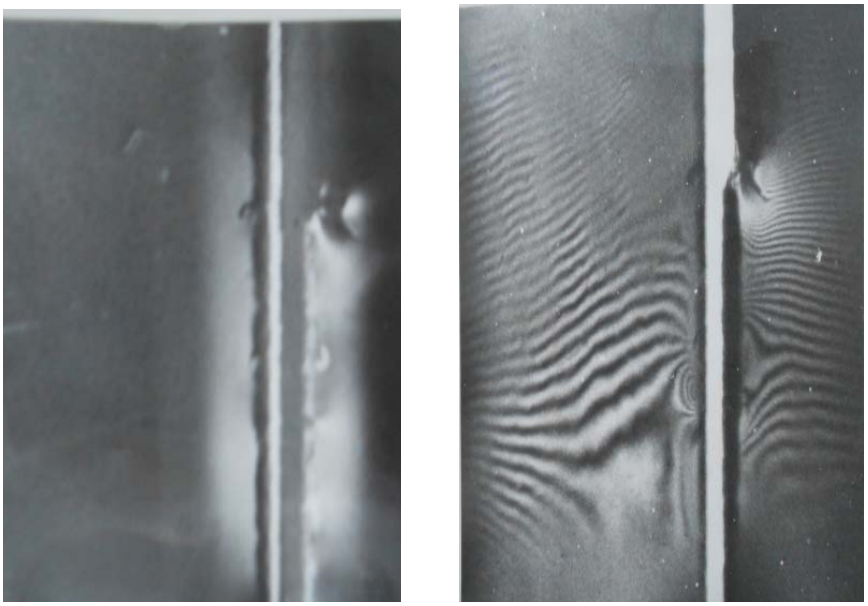

a) *b)*

Fig. 2. Topograms and moire pattern of analyzing crystal aperture. Reflection ($\bar{2}20$)
a) topograms from analyzing crystal aperture; b) moire pattern from analyzing crystal aperture ×12.

The cracks of 30 – 40 μm deep occur on the crystal surface after cutting. The aperture width was about 235 μm. The front cutting edge of the disc has sharp projections that will serve as concentrators of mechanical stresses and microcracks.

It is known that the largest damages to the surface of the crystal arise in the process of its cutting with a diamond disc. As a result of the impact stress that occurs in the cutting process, irregularities, traces of plastic deformation and brittle fracture are observed on the surface. Three specific dependences of the period of moire fringes on the deformation size can be differentiated in diffraction moire patterns: dilatation moire – $\Lambda_d = \frac{d_0 d}{|d - d_0|} = \frac{1}{\Delta g}$, rotating moire – $\Lambda_r = \frac{1}{\Delta g_r} = \frac{d_0}{\theta}$ and mixed moire – $\frac{1}{\Lambda} = \sqrt{(\frac{1}{\Lambda_d})^2 + (\frac{1}{\Lambda_r})^2}$, Δg_r – change in diffraction vector, g – diffraction vector, d_0 – interplane lattice distance, d – interplane distance of deformed lattice. By measuring the periods of moire fringes and their inclination relative to reflecting surfaces by means of relations:

$$d = \Lambda[1 + (\frac{\Lambda}{d_0})^2 + 2\frac{\Lambda}{d_0}\cos\varphi]^{\frac{1}{2}},\ \theta = \frac{\sin\varphi}{\frac{\Lambda}{d_0} + \cos\varphi}$$

the relative deformations $\Delta d/d_0$ and atomic plane turns θ in the analyzing crystal were calculated. The relative deformations vary from 3×10^{-6} to 0.17×10^{-6} and atomic plane changes – from 0.0032 to 0.25 arcsec.

It can be seen from the moire patterns and topograms (Fig. 1) that the area, in which moire fringes are not present, is 125 μm from the edge of the aperture, due to violation of the coherence of interfering waves. In the moire pattern at a distance of more than 125 μm, a large distortion area is observed, which includes dislocations and no moire fringes, because the distance between them is very small at the boundary of film resolution (Fig. 1, 2*b*). Beyond this zone, dislocations manifested in the form of additional moire fringes are observed.

It follows from the analysis of the relative deformations and atomic plane changes that the fields of elastic deformations expand at a distance of about 700 – 1000 μm. In addition to X-ray interferometric studies, X-ray topographic studies were conducted using three-crystal Laue spectrometer (one was made of interfering beams covered with an opaque screen). Fig. 2*a* shows a topogram obtained in a three-crystal Laue spectrometer circuit. It follows from interferograms and topograms that the defective structure, which occurs during crystal cutting, is generally composed of a strongly deformed area of the crystal matrix. These areas are manifested in the form of black and white lobes (Fig. 1, 2). These fields expand to a large depth – hundreds of microns.

The paper proposes a method for determining the sign of deformation. For this purpose a thermoelement was used, which made it possible to form the temperature gradient along the atomic planes ($\bar{1}10$) in the direction of [$11\bar{2}$], the value of which was 1.2 K/cm, as shown in [9].

The homogeneous temperature gradient proves the stability of thermoelement operation, since the exposure period of obtaining moiré patterns lasted almost 5 hours. The temperature gradient will increase interplanar distances in the analyzer. The analysis of interferograms shows that the deformation in the crystal aperture area is the tensile deformation. The increase in periods also testifies to the nonuniform distribution of elastic deformation fields.

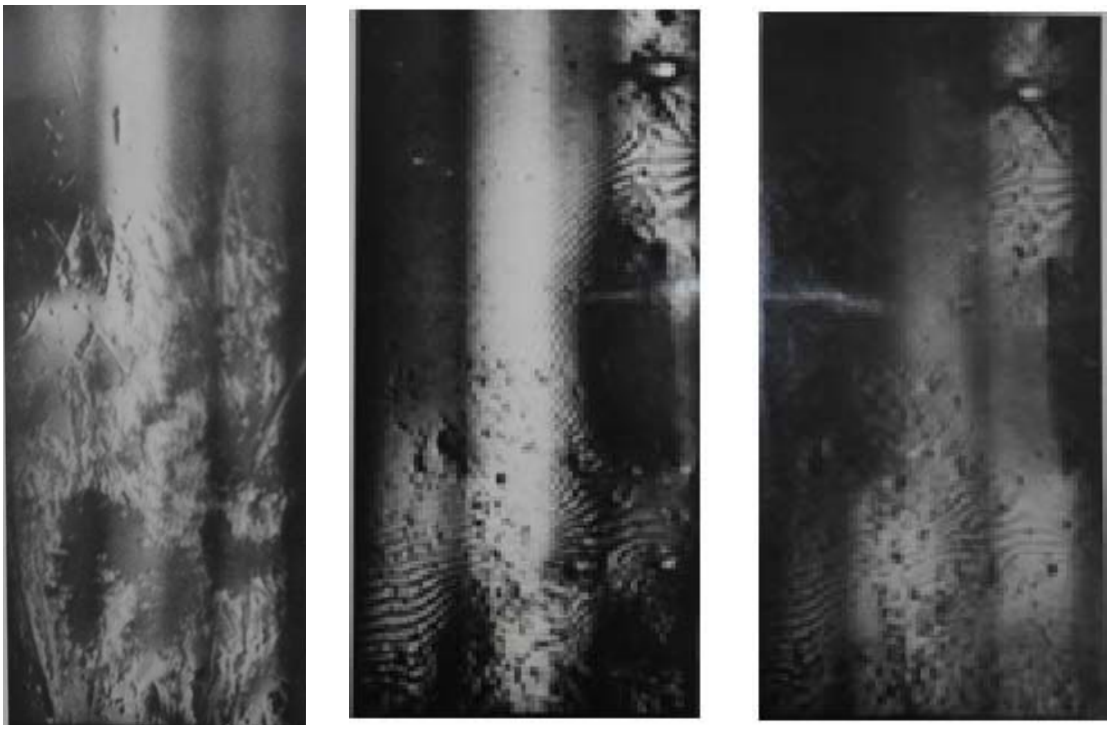

a) *b)* *c)*

Fig. 3. Interferograms and topograms of partially processed surface of analyzing crystal: a) topogram, reflection ($\bar{2}20$); b) interferogram in the direction of diffracted beam; c) in the direction of the incident beam ×12.

With the partial processing of the original surface (111) of the interferometer analyzer with emery powders with grain size of 5 μm, scratches, chips with sharp edges, microcracks, etc., are observed in the topogram (Fig.3*a*) (the topogram was obtained in three-crystal LLL-spectrometer circuit). In some places, where the surface is not damaged by abrasive materials, the areas with the reduced intensity are observed (in Fig. 3*a* an opposite contrast relative to a photoplate), which testify to the presence of nonrelaxing elastic distortions in the crystal.

It can be seen from the moire patterns (Fig. 3*b*, *c*) obtained using the three-crystal interferometer that the surface microdamage significantly distorts it. The periods and inclinations of the moire fringes vary in wide ranges, as well as their disappearance in some areas testify to nonuniform stress distribution across the wafer area. The reduced intensity areas occur in some places (Fig. 3*a*), where the deformation equals to 10^{-5}. These areas are characterized by contrast addition in the direction of the incident beams (Fig. 3*b*) and diffracted (Fig. 3*c*) beams.

With a uniform polishing of the analyzer surface (111), an attempt to obtain the moire pattern was unsuccessful. The high density of defects and large stresses in the crystal completely destroy the interference interaction of X waves. It is worth noting that the low-temperature annealing at 700 K had had no positive effect as well. After the annealing of the interferometer at 1123 K, the moire pattern shown in Fig. 4 was obtained.

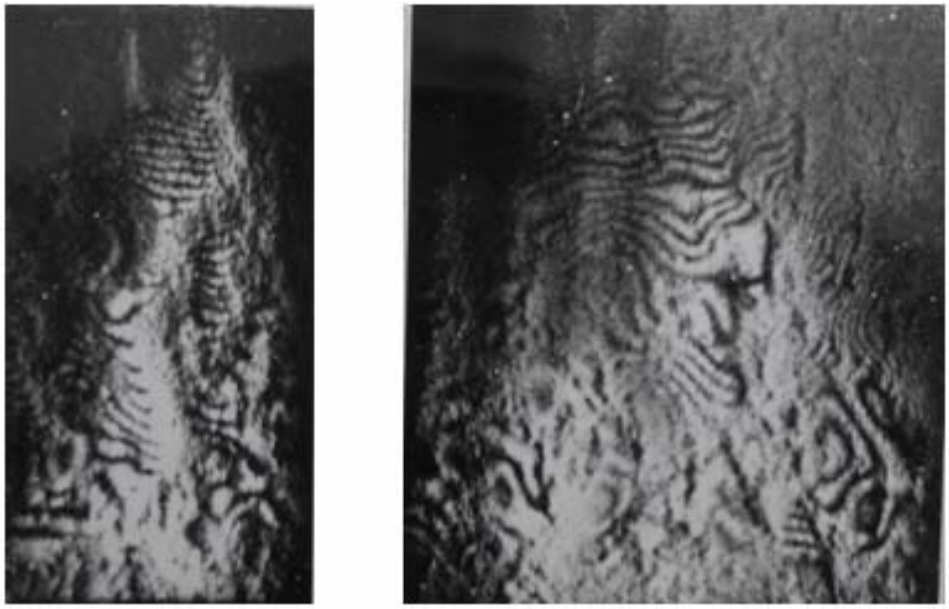

a) *b)*

Fig. 4. Moire patterns obtained from different parts of the crystal after annealing at 1123 K. *Reflection* $(\bar{2}20)$ *×12.*

The analysis of the moire patterns shows that the stress distribution becomes more uniform. The deformation in the crystal varies from 10^{-5} to 10^{-6}. Almost all irregularities in the periods of moire fringes are detected in the moire patterns: additional moire fringes, fork-like lines, crosslines between fringes, shifts of several fringes, etc. This is most likely associated with the reconstruction of the damaged layer and formation of dislocations, as evidenced by the presence of additional moire fringes. Most dislocations are straight-line, lying in {111} planes. The low-temperature stage of stress relaxation in mechanically damaged layers is accompanied by conservative movement of dislocations. Similar defects were observed earlier during the machining of crystals [6, 11]. After etching of the damaged layer 10 μm thick, more distinct moire fringes were observed. Therefore,

dislocation dipoles, packing and other defects are detected in the subsurface layer. Dashed lines of the diffraction contrast mostly oriented in the direction of $[11\bar{2}]$ (Fig. 4*a*, *b*), fields of elastic deformations lead to the bending of moire fringes. Obviously, dashed lines correspond to dislocations oriented along this direction $[11\bar{2}]$. The dislocations of this type were detected by electron microscopy in [1, 2, 11]. In the presented interferograms, individual microcracks are observed in the form of dark lines oriented in different directions, from which short moire fringes extend (the pattern is similar to the X-tree branches). The deformations located in close vicinity to residual microcracks can be defined from the moire patterns.

The study of the damaged layer depth, which greatly depends on the size of abrasive grains, is of particular interest. For this purpose, the polishing with various abrasive materials was carried on the end surface of the analyzer wafer that corresponded to the crystallographic plane $(11\bar{2})$. The assessments of the damaged layer depth were also conducted by optical microscopy. X-ray topograms and interferograms obtained during diffraction from the planes $(\bar{2}20)$, are shown in Fig. 5*a*, *b*, *c*, *d*, *e*, *f*. When polishing with abrasive material M-5 (Fig. 5*a*, *b*), some cracks and areas of high scattering intensity can be seen in topograms; interferograms along with usual topographic images show the change of the original moire pattern, indicating the emergence of the elastic deformation area. The depth of the damaged layer is 15 – 20 μm (together with an area of elastic deformations).

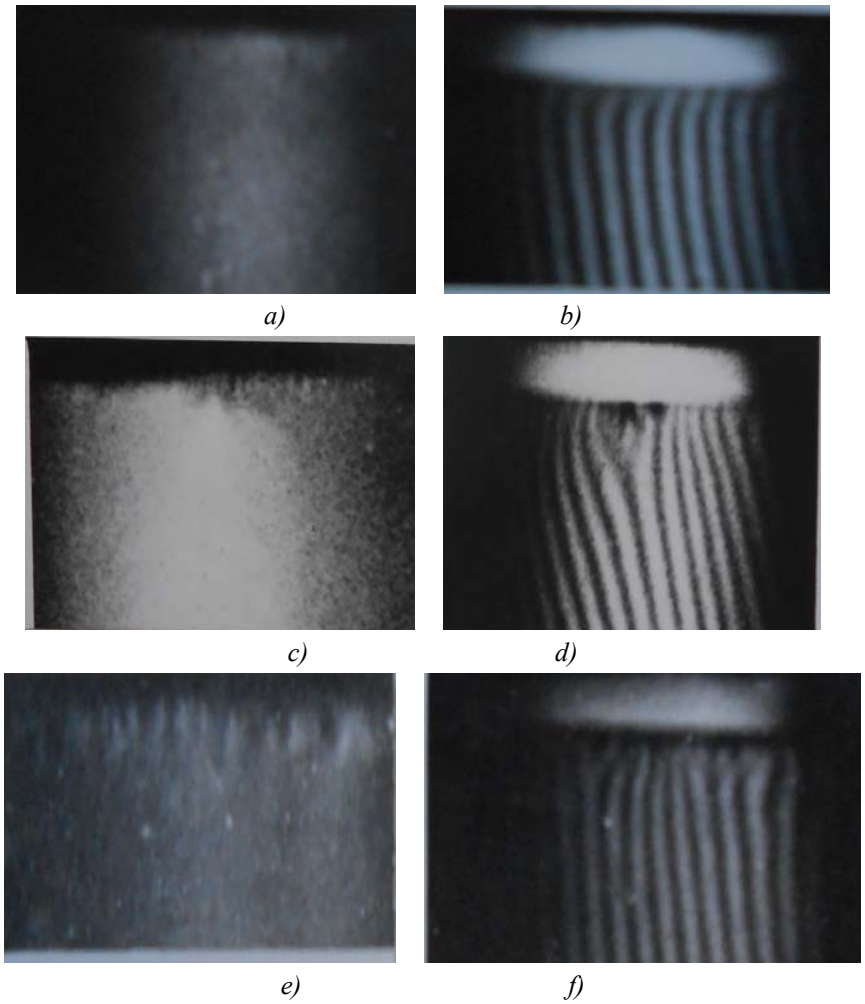

Fig. 5. Topographic and moire images of the damaged layer depth. Reflection $(\bar{2}20)$ a) b) surface machine processing $(11\bar{2})$ with M5 powder; c) d) with M10 powder; e) f) with M28 powder ×12.

If the abrasive material size is 10 μm (Fig. 5*c*, *d*) black and white lobes of deformation rosettes and a sufficiently large area of elastic deformations begin to appear in topograms, and additional fringes or their splits, as well as an essential region of elastic deformations over long distances, are observed in the moire patterns. The depth of the damaged layer is 35 – 40 μm. If the abrasive material size is 28 μm (Fig. 5*e*, *f*), the number of deformation rosettes and irregularities in the moire patterns increases. The damaged layer depth is approximately 120 – 140 μm. In terms of X-ray diffraction, the damaged layer can be divided into two zones: of kinematic and dynamic scattering. The kinematic scattering is observed from the polycrystalline part of the damaged layer - from the zones of dislocation ensembles and elastic deformations.

As a result of the studies conducted by the optical microscopy, X-ray topography and X-ray diffraction moire methods, the damaged layer model can be represented as follows: *a*) a relief zone with polycrystalline structure, from which the kinematic scattering is observed; this zone is best determined by the optical microscopy method, and its approximate dimensions are 0.2 – 0.5 *d* (*d* – abrasive material grain size); *b*) a zone of microcracks, packing defects and dislocation ensembles, which is well defined by the electron microscopy, X-ray diffraction moire and X-ray topography methods (optical microscopy methods are not used here), the zone depth varies in the range of 3 – 4 *d*; *c*) an elastic deformation zone; in this area, X-ray diffraction moire method has advantages over all other known methods, since the sensitivity of X-ray diffraction moire method to lattice distortion is 10 times higher than of the electron diffraction moire method, and the depth of the damaged area is 4 – 5 *d*. The values of deformations and stresses in the second and third zones can be reliably determined by the X-ray diffraction moire method. The discrepancy in the received data on determining the damaged layer depth in the latter zone is the most significant in comparison with known measurements reported in literature [1, 2].

Conclusions

A new method of determination of the damaged layer depth in the silicon single crystals using X-ray diffraction moire was proposed. A refined model of the damaged layer, consisting of: *a*) a relief zone with polycrystalline structure, from which the kinematic scattering as large as (0.2 – 0.5 *d*) is observed; *b*) a zone of microcracks, packing defects and dislocation ensembles of (3 – 4 *d*); *c*) an elastic deformation zone with an area of (4 – 5 *d*). This elastic deformation zone is quite long, even during the removal of the first two zones the residual stresses in the crystals still remain.

References

1. V.I. Karban, P. Koy, V.V. Rogov et al., *Machine Processing of Semiconductor Materials*, Ed.by N.V. Novikov, V. Berthold (Kyiv: Naukova Dumka, 1982).
2. O.A. Kontsevoy, Yu.M. Litvinov, and E.A. Fattakhov, *Plasticity and Strength of Semiconductor Materials and Structures* (Moscow: Radio i Sviaz, 1982), 240.
3. I.V. Kogut, V.I. Khrupa, I.V. Prokopenko, and L.I. Datsenko, The Influence of Defects Arising during Abrasive Machine Processing of Surface on X-Ray Scattering with Thin Crystals in Case of Laue Diffraction, *Physics of Metals* **7**(1), 81 – 84 (1985).
4. V.A. Solodukha, A.I. Belous, and G.G. Chigir', Measuring the Damaged Layer Depth on Silicon Wafer Surface by Auger Spectroscopy, *Science and Technology* 15(4), 329 – 334 (2016).
5. V.V. Nikolaev, V.I. Khrupa, M.Ya. Skorokhod, and D.O. Grigoriev, Influence of Surface Disturbances on the Structure of Reflective Thin Crystals, *Physics of Metals* **11**(2), 68 – 73 (1989)

6. M.G. Melvidskiy, V.G. Fomin, M.M. Hatckevich, H.M. Pavlov et al., Integrated X-Ray Diffraction Study of Disturbed Layers Caused by Silicon Cutting, *Fizika i Kmimiya Obrabotki Materialov* 2, 122 – 125 (1986).
7. N.D. Raransky, Ya.M. Struk, I.M. Fodchuk, V.P. Shafranyuk, and A.N. Raransky, Applied Possibilities of X-Ray Diffraction Interferometry, *Proc.SPIE -Bellingham* 2647, 457 – 467 (1995).
8. V.P. Shafranyuk, Potential of X-Ray Diffraction Interferometry in Studying the Relaxation of Local Mechanical Stresses in the Subsurface Layers of Single Crystals, *Scientific Bulletin of Chernivtsi National University, Physic*s, issue 32, 122 – 127 (1998).
9. V.P. Shafranyuk, Determination of Structural Changes and Temperature Distribution within Crystals, *J.Thermoelectricity* 3, 89 – 94 (1998).
10. N.D. Raransky, V.P. Shafranyuk, Illustration of Packing Defects in X-ray Diffraction Moire, *UFIS* **27**(6), 901 – 904 (1982).
11. N.I. Doronicheva, A.A. Ladochkin B.L. Meiler, M.G. Milvidskiy et al., Relaxation of Mechanical Stresses during Thermal Processing of Silicon Wafers, *Crystallography* **29**(2), 337 – 342 (1984).

Submitted 30.08.2016

R.R. Kobylianskyi

R.R. Kobylianskyi[1,2]

[1]Institute of Thermoelectricity, 1, Nauky str.,
Chernivtsi, 58029, Ukraine;
[2]Yu.Fedkovych Chernivtsi National University,
2, Kotsyubinsky str., Chernivtsi, 58012 Ukraine

COMPUTER SIMULATION OF MEDICAL-PURPOSE THERMOELECTRIC SENSOR READINGS

This paper presents the results of computer research on the impact of thermal medical insulation on the readings of thermoelectric heat flux sensor. A three-dimensional (3D) physical, mathematical and computer model of biological tissue having on its top a thermoelectric sensor with thermal insulation was constructed. It was established that the presence of medical thermal insulation on thermoelectric sensor and biological tissue can change sensor readings up to 75 %.

Key words: Thermoelectric sensor, heat flow and thermal insulation medical, computer modeling.

Introduction

General characterization of the problem. It is known that timely and quality diagnosis is critical to successful treatment of various human diseases [1 – 5]. For its performance it is important to have information on human heat release, as long as exactly heat flux density reflects most adequately the severity level of inflammatory processes in human organism [6, 7]. So, for early diagnosis of diseases it is efficient to measure human body heat flux. Promising for such measurements are thermoelectric sensors [8 – 11] which offer high sensitivity, precision, speed of response, parameter stability in a wide range of operating temperatures and are consistent with up-to-date recording equipment. A combination of miniature size and high sensitivity of semiconductor heat metering sensors yields high locality and precision of heat metering measurements during medico-biological investigations. The above advantages make it possible to use thermoelectric sensors for local diagnosis of human body, early detection of inflammatory processes, oncologic diseases, blood circulation anomalies and analysis of human body state under extreme conditions.

It is also important to control heat release on human body areas after operational intervention. With normal wound healing, heat release, though increased, is within corresponding limits. However, if healing is accompanied by essential inflammatory processes (for instance, due to breach of wound sterility), it is thermoelectric sensor in the first place that can inform of such processes by recording local thermal anomalies. Thus, monitoring of human body heat release is of exceptional importance, since it can yield information both on the disease recurrence and, on the contrary, on rehabilitation processes.

When investigating human heat release in the post-surgical period an important role is played by thermal insulation (for instance, medical bandage) on thermoelectric sensor which can essentially distort the temperature field of human body area under study and affect the readings of such sensor. The impact of such sensors on the object of investigation was analytically studied in [12] and for the

case of living objects with the aid of computer simulation for simplified physical models in [13 – 16].

Therefore, *the purpose of this work* is to create improved computer model and to determine the impact of medical thermal insulation on the readings of thermoelectric heat flux sensor.

A physical model of biological tissue with thermoelectric sensor and thermal medical insulation

According to a physical model (Fig. 1), an area of human biological tissue is a three-layered skin structure (epidermis 1, dermis 2, subcutis 3) with the internal tissue 4 as the fourth layer and is characterized by thermal conductivity κ_i, specific heat C_i, density ρ_i, blood perfusion rate ω_b, blood density ρ_b, blood heat capacity C_b and specific heat release q_{met} due to metabolic processes (Table). The respective biological tissue layers 1 – 4 are considered as the bulk sources of heat q_i, where:

$$q_i = q_{met} + \rho_b C_b \omega_i (T_b - T), \quad i = 1..4 . \tag{1}$$

The geometric dimensions of each such layer are a_i, b_i and l_i. The temperatures at the boundaries of respective biological tissue layers are T_1, T_2, T_3 and T_4.

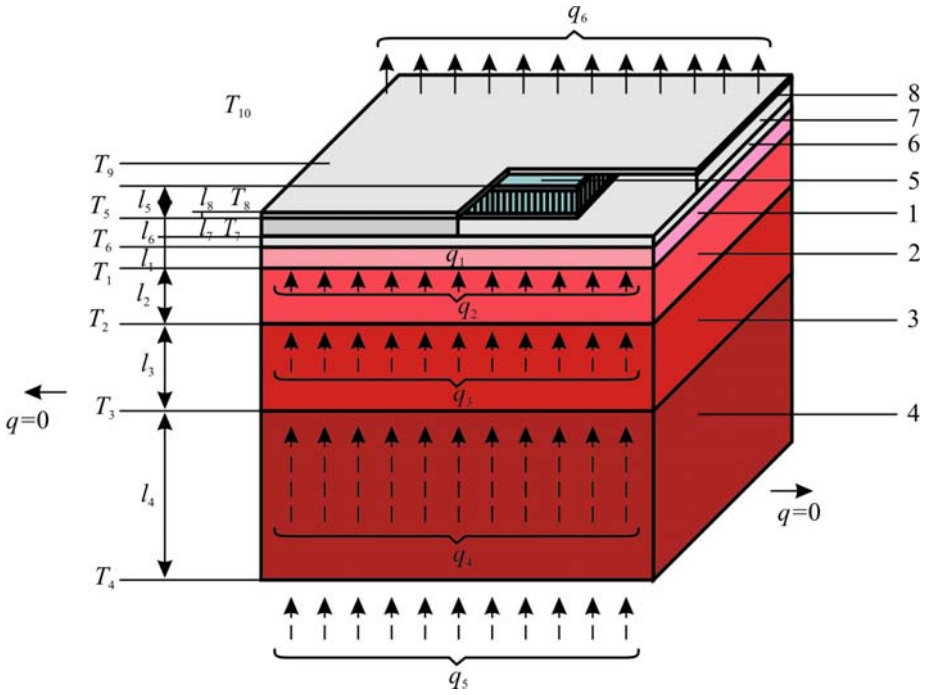

Fig. 1. A physical model of biological tissue with thermoelectric heat meter and thermal medical insulation: 1 – epidermis, 2 – dermis, 3 – subcutis, 4 – internal tissue, 5 – thermoelectric heat flux sensor, 6, 7, 8 – thermal medical insulation.

Thermoelectric heat flux sensor 5 is a rectangular bar of the geometric dimensions a_5, b_5 and l_5, which consists of a large number of *n*- and *p*-type crystals based on *Bi-Te* thermoelectric material. From the theory it is known [8, 12] that thermoelectromotive force (EMF) of thermoelectric gradient sensor is determined as follows:

$$E = \alpha N \Delta T , \tag{2}$$

where α is the Seebeck coefficient, N is the number of thermoelectric material legs, ΔT is temperature difference between the upper and lower surfaces of thermoelectric heat flux sensor.

Table

Thermophysical properties of human biological tissue [17 – 21]

Biological tissue layers	Epidermis	Dermis	Subcutis	Internal tissue
Thickness, l (mm)	0.08	2	10	30
Specific heat, C ($J \cdot kg^{-1} \cdot K^{-1}$)	3590	3300	2500	4000
Thermal conductivity, κ ($W \cdot m^{-1} \cdot K^{-1}$)	0.24	0.45	0.19	0.5
Density, ρ ($kg \cdot m^{-3}$)	1200	1200	1000	1000
Metabolic heat density, q_{met} ($W \cdot m^{-3}$)	368.1	368.1	368.3	368.3
Tissue blood perfusion rate, ω_b ($m^3 \cdot s^{-1} \cdot m^{-3}$)	0	0.00125	0.00125	0.00125
Blood temperature, T_b (K)	310	310	310	310
Blood density, ρ_b ($kg \cdot m^{-3}$)	1060	1060	1060	1060
Blood heat capacity, C_b ($J \cdot kg^{-1} \cdot K^{-1}$)	3770	3770	3770	3770

The skin surface layer (epidermis 1) of temperature T_6 is in the state of heat exchange with thermal medical insulation 6 of the geometric dimensions a_6, b_6, l_6 and contact surface temperature T_5. Located on the surface of thermal insulation 6 is thermoelectric heat flux sensor 5 of the geometric dimensions a_5, b_5, l_5 and contact surface temperature T_8. In the absence of thermal insulation 6, 7, 8 the heat exchange between skin surface and the environment of temperature T_{10} is taken into account by heat exchange coefficient α_1 and emissivity coefficient ε_1. Skin heat exchange due to perspiration is disregarded.

Additional thermal medical insulation 7, 8 of the geometric dimensions a_7, b_7, l_7 and a_8, b_8, l_8 is arranged on the surface and on the sides of thermoelectric sensor 5. Free surface of thermal insulation 8 of temperature T_9 is in the state of heat exchange with the environment of temperature T_{10} which is taken into account by heat exchange coefficient α_2 and emissivity coefficient ε_2. Specific heat flux from the surface of thermal insulation 8 to the environment is q_6, and specific heat flux from human internals – q_5.

As long as a physical model is an area of a four-layered biological tissue, with identical biochemical processes occurring in adjacent layers, it can be assumed that no heat overflow occurs along biological tissue ($q = 0$).

Mathematical description and a computer model

A general equation of heat exchange in biological tissue is as follows [17 – 21]:

$$\rho C \frac{\partial T}{\partial t} = \nabla(\kappa \nabla T) + \rho_b C_b \omega_b (T_b - T) + q_{met}, \quad (3)$$

where ρ is the density of corresponding biological tissue layer, C is specific heat of biological tissue layer, κ is thermal conductivity of biological tissue, ρ_b is blood density, C_b is specific heat of blood, ω_b is blood perfusion rate, T_b is human blood temperature, q_{met} is metabolic heat density.

The summand on the left-hand side of equation (3) is the rate of change in thermal energy comprised in the unit volume of biological tissue. Three summands on the right-hand side of this

equation are the rate of change in thermal energy due to thermal conductivity, blood perfusion and metabolic heat, respectively.

To solve the problem formulated in this paper, it is enough to consider a 3D steady-state model. Then Eq. (3) will acquire the form (4):

$$\kappa(\frac{\partial^2 T}{\partial x^2}+\frac{\partial^2 T}{\partial y^2}+\frac{\partial^2 T}{\partial z^2})+\rho_b C_b \omega_b (T_b - T)+q_{met}=0\,. \tag{4}$$

A steady-state equation of heat exchange for thermoelectric heat flux sensor with regard to the impact of thermoelectric phenomena and the temperature dependence of material is given by:

$$\kappa(T)(\frac{\partial^2 T}{\partial x^2}+\frac{\partial^2 T}{\partial y^2}+\frac{\partial^2 T}{\partial z^2})=-\alpha^2(T)\sigma(T)\left((\frac{\partial^2 T}{\partial x^2}+\frac{\partial^2 T}{\partial y^2}+\frac{\partial^2 T}{\partial z^2})\right)^2\,. \tag{5}$$

The corresponding steady-state equation of heat exchange for thermal medical insulation will be of the form (6):

$$\kappa(\frac{\partial^2 T}{\partial x^2}+\frac{\partial^2 T}{\partial y^2}+\frac{\partial^2 T}{\partial z^2})=0\,. \tag{6}$$

A steady-state system of equations (4) – (6) for the corresponding layers of physical model (Fig. 1) must be solved with the respective boundary conditions (7) – (8):

$$\begin{cases} q\big|_{x=0}=0, \\ q\big|_{x=a}=0, \end{cases} \qquad \begin{cases} q\big|_{y=0}=0, \\ q\big|_{y=a}=0, \end{cases} \tag{7}$$

$$\begin{cases} T\big|_{z=0}=310.15\ \text{K}, \\ q\big|_{z=b,c,d}=\alpha(T_0-T)+\varepsilon\sigma(T_0^4-T^4), \end{cases} \qquad \begin{cases} q\big|_{x=e,f}=0, \\ q\big|_{y=e,f}=0, \end{cases} \tag{8}$$

where q is heat flux density, T is absolute temperature, T_0 is ambient temperature, α is heat exchange coefficient, ε is emissivity factor, σ is the Boltzmann constant.

In order to determine the impact of thermal medical insulation on the readings of thermoelectric heat flux sensor, a 3D computer model of biological tissue was created having on its surface a thermoelectric sensor with thermal insulation. For this purpose Comsol Multiphysics applied program package was used [22] allowing simulation of thermophysical processes in biological tissue with account of blood circulation and metabolism.

The distribution of temperature and heat flux density in biological tissue and thermoelectric sensor was calculated by the finite element method (Fig. 2). According to this method, an object under study is split into a large number of finite elements, and in each of them the value of function is sought which satisfies given differential equations of second kind with the respective boundary conditions. The accuracy of solving the formulated problem depends on the level of splitting and is assured by using a large number of finite elements [22].

Computer simulation results

With the aid of computer simulation the distributions of temperature and heat flux density lines in human biological tissue and thermoelectric heat flux sensor were obtained (Fig. 3 – 5), as well as isothermal surfaces in biological tissue were constructed (Fig. 6, 7) with regard to boundary effects in a 3D computer model.

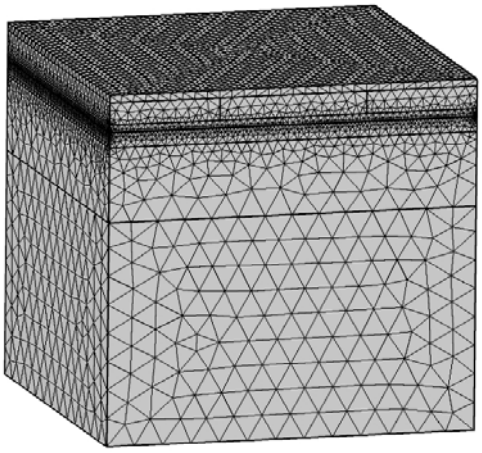

Fig. 2. Finite element method mesh.

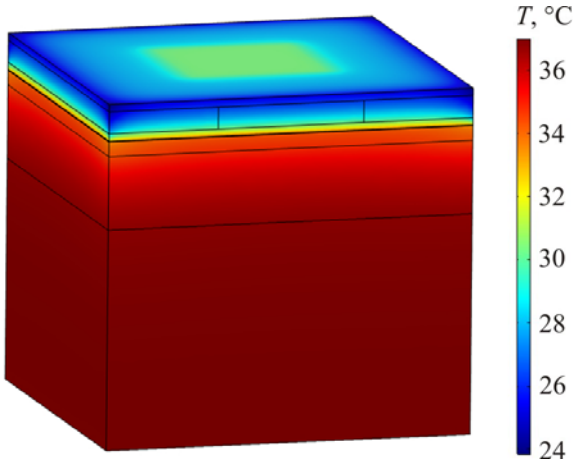

Fig. 3. Temperature distribution in biological tissue having on its top a thermoelectric sensor with thermal medical insulation.

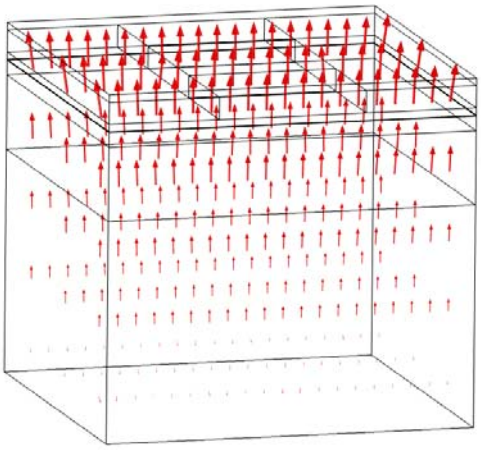

Fig. 4. Distribution of heat flux density lines in biological tissue having on its top a thermo-electric sensor with thermal medical insulation.

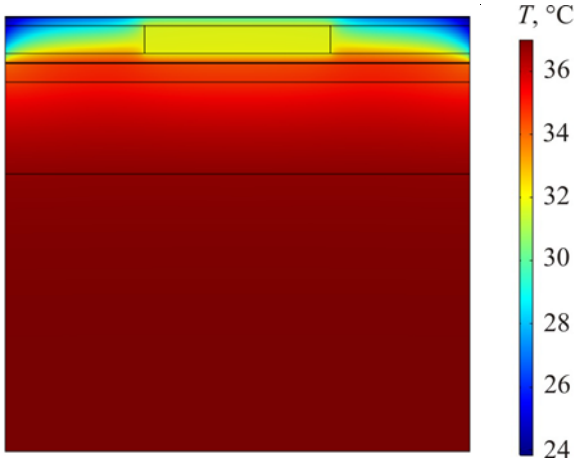

Fig. 5. Temperature distribution in the section of biological tissue having on its top a thermoelectric sensor with thermal medical insulation.

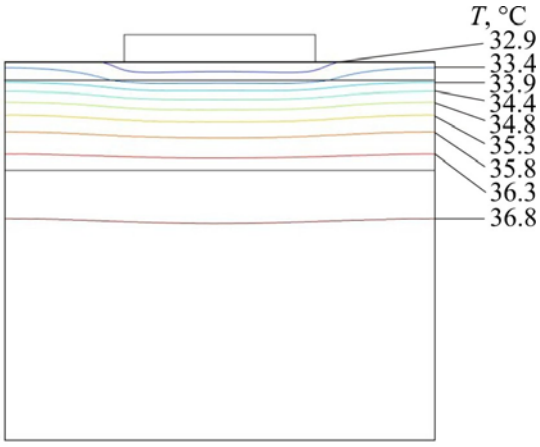

Fig. 6. Isothermal surfaces in biological tissue having on its top a thermoelectric sensor without thermal medical insulation.

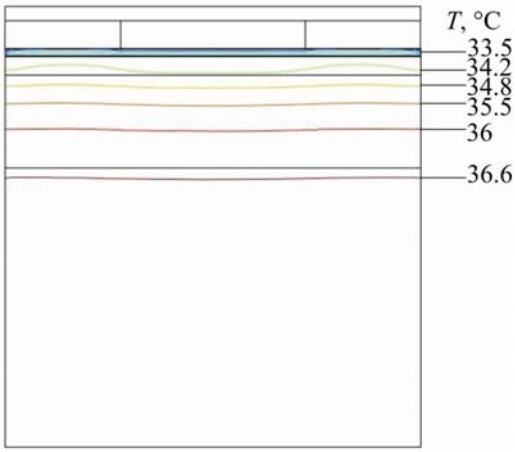

Fig. 7. Isothermal surfaces in biological tissue having on its top a thermoelectric sensor with thermal medical insulation.

To determine temperature difference between the surfaces of thermoelectric sensor, averaging of the obtained temperature distributions on the upper and lower sensor surfaces was obtained, as long as such distributions are irregular. As an example, the distributions of temperature along the line in the centre of the lower (Fig. 8*a*) and upper (Fig. 8*b*) surfaces of thermoelectric sensor are shown.

Fig. 8*c* shows temperature distribution on the surface of biological tissue having on its top a thermoelectric sensor with thermal medical insulation. Temperature distribution on the surface of external thermal insulation is shown in Fig. 8*d*.

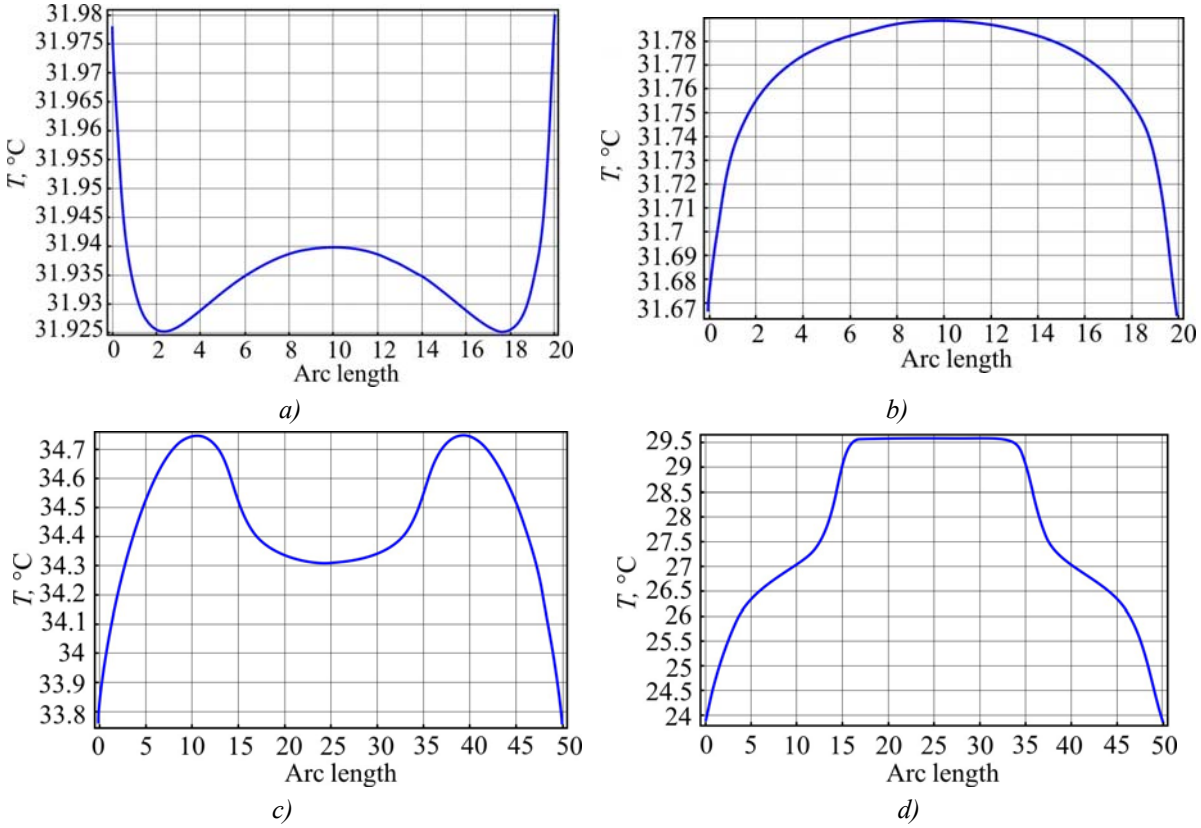

Fig. 8. Temperature distribution of thermoelectric sensor with thermal insulation exceeding the limits of sensor. a) on the lower surface, b) on the upper surface, c) on the surface of biological tissue, d) on the surface of thermal insulation.

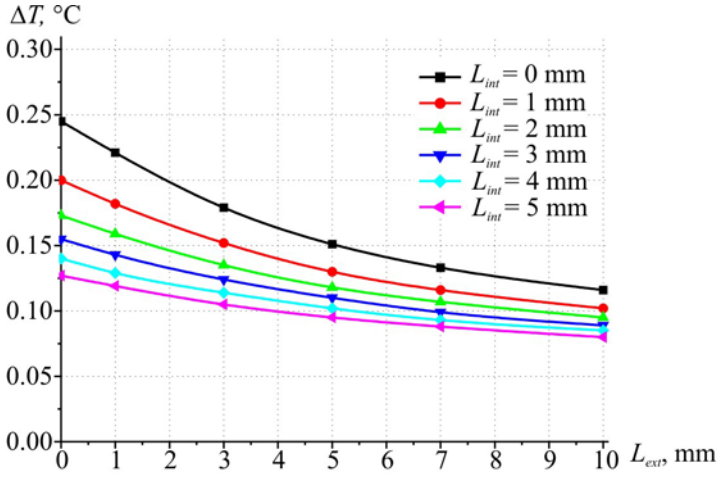

Fig. 9. Dependence of temperature difference on thermoelectric heat flux sensor on the thickness if thermal medical insulation on the sensor (external bandage layer L_{ext}) with different thickness of thermal insulation between biological tissue and the sensor (internal bandage layer L_{int}).

Computer simulation was used to determine the impact of thermal medical insulation on the readings of thermoelectric heat flux sensor. A dependence of temperature difference on thermoelectric sensor on the thickness of thermal medical insulation on the sensor (external bandage layer L_{ext}) was determined with different thickness of thermal insulation between biological tissue and the sensor (internal bandage layer L_{int}) for the case when external thermal insulation does not exceed the sensor limits (Fig. 9).

From Fig. 9 it is seen that increasing the thickness of thermal insulation between biological tissue and thermoelectric heat flux sensor, as well as increasing the thickness of external insulation on the sensor definitely results in decreasing temperature difference between the sides of such sensor. Reduction of heat flux thermoelectric sensor readings can reach 75 % as compared to the case without thermal medical insulation. This, in turn, must be taken into account for the diagnosis of post-surgical inflammatory processes in human organism by creating identical conditions with repeated measurements of heat release.

Conclusions

1. Computer methods were developed for simulation of thermal and temperature processes in "thermoelectric sensor- human body surface" system with regard to thermophysical properties of biological tissue, blood circulation and metabolism. It was established that proposed methods are much more efficient as compared to known analytical methods that are based on solving approximate boundary problems.
2. Computer simulation was used to study the impact of thermal medical insulation on the readings of medical-purpose thermoelectric sensor. It was established that the presence of thermal insulation on thermoelectric heat flux sensor and biological tissue can change sensor readings up to 75 %. This factor must be taken into account when measuring human body heat fluxes by creating identical conditions during repeated measurements.

The author is sincerely grateful to NASU academician L.I. Anatychuk for the formulation of relevant problem and constructive discussion of the results.

References

1. L.I. Anatychuk, O.I. Ivaschuk, R.R. Kobylianskyi, I.D. Postevka, V.Yu. Bodiaka, I.Ya. Gushul, Thermoelectric Device for Temperature and Heat Flux Density Measurement "ALTEC-10008", *J.Thermoelectricity* 1,76 – 84(2016).
2. V.S. Gischuk, R.R. Kobylianskyi, and R.G. Cherkez, Multi-Channel Device for Temperature and Heat Flux Density Measurement, *Scientific Bulletin of Chernivtsi University: Collected Scientific Works. Physics. Electronics, **3**, issue 1* (Chernivtsi: Chernivtsi National University, 2014), p. 96 – 100.
3. R.R. Kobylianskyi, V.V. Boichuk, The Use of Thermoelectric Heat Meters in Medical Diagnostics, *Scientific Bulletin of Chernivtsi University: Collected Scientific Works. Physics. Electronics, **4**, issue 1* (Chernivtsi: Chernivtsi National University, 2015), p. 90 – 96.
4. B.M. Demchuk, L.Ya. Kushneryk, and I.M. Rublenyk, Thermoelectric Sensors for Orthopedics, *J.Thermoelectricity* **4**, 80 – 85 (2002).
5. A.A. Ascheulov, L.Ya. Kushneryk, Thermoelectric Device for Medico-Biological Express-Diagnostics, *Tekhnologiya i Konstruirovaniye v Elektronnoi Apparature* **4**, 38 – 39 (2004).

6. R.B. Ladyka, D.N. Moskal and V.D. Didukh, Semiconductor Heat Meters in Arthropathy Diagnostics and Treatment, *Meditsinskaya Tekhnika* **6**, 34 – 35 (1992).
7. R.B. Ladyka, O.N. Dakalyuk, L.P. Bulat and A.P. Myagkota, Use of Semiconductor Heat Meters in the Diagnostics and Treatment, *Meditsinskaya Tekhnika* **6**, 36 – 37 (1996).
8. L.I. Anatychuk, *Thermoelements and Thermoelectric Devices: Reference Book* (Kyiv:Naukova Dumka, 1979), 768 p.
9. L.I. Anatychuk, N.G. Lozinsky, P.D. Mykytyuk and Yu.Yu. Rozver, Thermoelectric Semiconductor Heat Meter, *Instruments and Experimental Techniques* **5**, 236 (1983).
10. L.I. Anatychuk, L.P. Bulat, D.D. Gutsal and A.P. Myagkota, Thermoelectric Heat Meter, *Instruments and Experimental Techniques* **4**, 248 (1989).
11. L.I. Anatychuk, R.R. Kobylianskyi, and I.A. Konstantinovich, Calibration of Thermoelectric Heat Flux Sensors, *Proc. of XV International Research and Practical Conference "Current Information and Electronic Technologies", Vol.2* (Odessa, Ukraine, May 26-30, 2014), P. 30 – 31.
12. O.A. Geraschenko, *Foundations of Heat Flux Measurement* (Kyiv: Naukova Dumka, 1971), p.192.
13. L.I. Anatychuk, R.R. Kobylianskyi, Research into the Effect of Thermoelectric Heat Meter on Human Heat Release Measurement, *J.Thermoelectricity* 4, 60 – 66 (2012).
14. L.I. Anatychuk, R.R. Kobylyanskii, 3D-Model for Determination of Thermoelectric Heat Meter Effect on the Accuracy of Human Heat Release Measurement, *Scientific Bulletin of Chernivtsi University: Collected Scientific Works. Physics. Electronics, **2**, issue 1* (Chernivtsi: Chernivtsi National University, 2012), p. 15 – 20.
15. L.I. Anatychuk, R.R. Kobylianskyi, Computer Design of Thermoelectric Heat Meter Readings under Real-Service Conditions, *J.Thermoelectricity* 1, 53 – 60 (2013).
16. L.I. Anatychuk, R.G. Giba, and R.R. Kobylianskyi, Some Peculiarities of Using Medical Heat Meters in the Investigation of Local Human Heat Release, *J.Thermoelectricity* 2, 67 – 73 (2013).
17. S.C. Jiang, N. Ma, H.J. Li, and X.X. Zhang, Effects of Thermal Properties and Geometrical Dimensions on Skin Burn Injuries, *Burns* **28**, 713 – 717 (2002).
18. M.P. Cetingul, C. Herman, Identification of Skin Lesions from the Transient Thermal Response Using Infrared Imaging Technique, *IEEE*, 1219 – 1222 (2008).
19. M. Ciesielski, B. Mochnacki, and R. Szopa, Numerical Modeling of Biological Tissue Heating. Admissible Thermal Dose, *Scientific Research of the Institute of Mathematics and Computer Science* **1**(10), 11 – 20 (2011).
20. Florin Filipoiu, Andrei Ioan Bogdan and Iulia Maria Carstea, Computer-Aided Analysis of the Heat Transfer in Skin Tissue, *Proceedings of the 3rd WSEAS Int. Conference on Finite Differences - Finite Elements - Finite Volumes - Boundary Elements*, 2010, p. 53 – 59.
21. Daniela Carstea, Ion Carstea, and Iulia Maria Carstea, Interdisciplinarity in Computer-Aided Analysis of Thermal Therapies, *WSEAS Transactions on Systems and Control* **6**(4), 115 – 124 (2011).
22. COMSOL Multiphysics User's Guide, COMSOLAB, 2010, 804 p.

Submitted 11.08.2016

A.V. Prybyla

A.V. Prybyla

Institute of Thermoelectricity of the NAS and MES of Ukraine,
1, Nauky Str., Chernivtsi, 58029, Ukraine

THERMOELECTRIC CONDITIONER WITH UNIFORMLY DISTRIBUTED MODULES FOR A HUMAN

The results of computations of a thermoelectric (TE) conditioner with the uniformly distributed modules design are presented in this paper. The physical, mathematical and computer models of the TE conditioner were developed. Its efficiency for different thermal resistance values and conditions for its exploitation were determined.

Key words: thermoelectric module, computer simulation, clothing TE conditioning.

Introduction

General characteristics of the problem. When humans undergo various ambient temperature conditions they often suffer either from overheating or overcooling that influences their physiological state but negatively [1]. It firstly concerns the people who have to remain under such conditions for a long period of time because of their professional duties. To this group military servants, hot shop workers, sportsmen and alike belong in particular.

The problem of provision a human with comfortable functioning under different conditions can be solved, though, by creating some special TE conditioners for clothing. In [2] their detailed classification is given and the most prospective physical models of such conditioners to be implemented are highlighted. Of special interest are TE conditioners for clothing where thermoelectric cooling and heating are used [3]. It is connected with their advantages, such as cooling and heating provision, reliability, environmental friendliness (harmful cooling agents absence), high efficiency and low mass dimensions [4, 5].

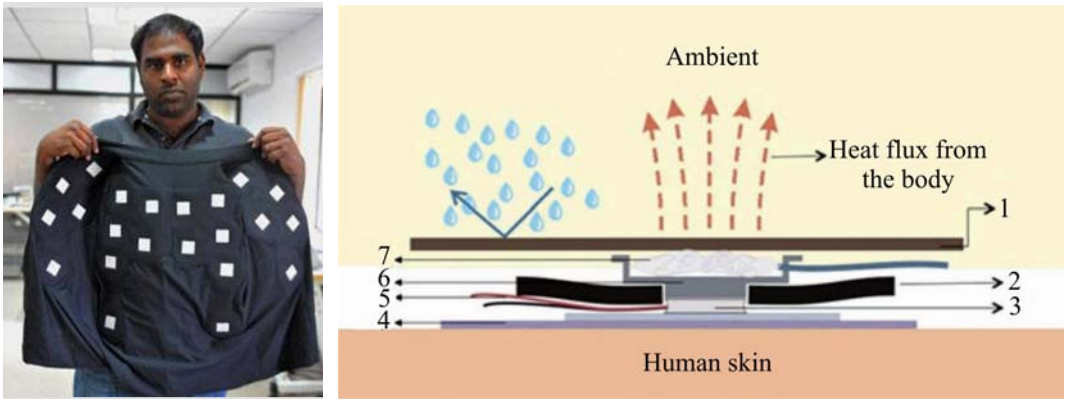

a) *b)*

Fig. 1. Appearance a) and physical model b) of a thermoelectric conditioner for the Dhama Innovations clothing [7]: 1 – heat-scattering fabric; 2 – insulation; 3 – thermoelectric modules; 4 – heat-conducting fabric; 5 – wires; 6 – heat concentrators; 7 – heat-conducting material.

The simplest and most demonstrative model of a thermoelectric conditioner for humans is a model with thermoelectric modules uniformly distributed over the surface of the clothing. However, as the modules sizes are significantly smaller than the heat-exchanging surface, heat supplies and heat diffusers should be used in such conditioners. [4] (Fig. 1). As it is clear from Fig. 1*a*, a TE conditioner contains 22 TE modules, whereas the schematic from Fig. 1*b* makes it clear that heat supplies and heat diffusing plates are used in it. Unfortunately, no energy characteristics of such a conditioner are given in [4, 6]. Therefore, computer research to determine the efficiency of such a model, being the objective of the present work, was performed.

Consequently, *the objective of the present work* is to examine the possibilities of implementation of a TE conditioner for the clothing with the uniformly distributed modules by way of computer simulation of its design.

Physical model of a thermoelectric conditioner for clothing

A physical model, presented in Fig. 2, was applied to compute an individual conditioner for a bullet-proof vest.

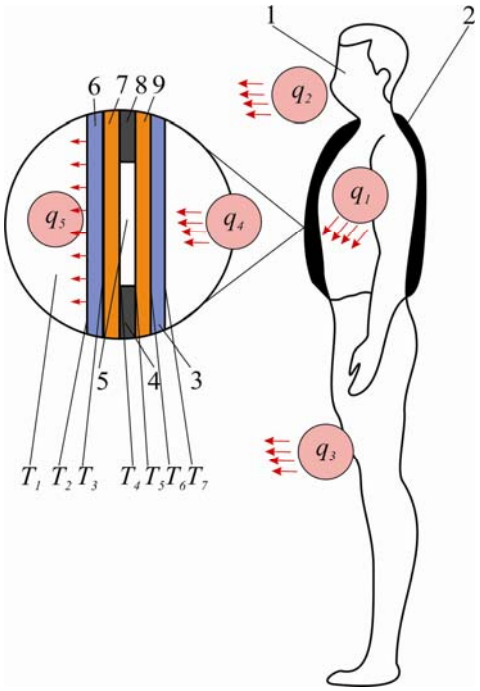

Fig. 2. Physical model of a thermoelectric conditioner for clothing with uniformly distributed modules: 1 – human body; 2 – vest with a conditioner; 3 – fabric, conducting heat from human body, and heat collector 9; 4, 8 – heat-insulation layers; 5 – thermoelectric module; 6 – fabric, conducting heat into the ambient, 7 – heat-conducting plate

It is built on the basis of the model depicted in Fig. 1*b* and presents a human body 1 that emits a heat flux q_1. Depending on the state the body is in (rest, physical loads of varying intensity, etc.) it produces a heat flux from 100 to 800 W [7]. This flux is rejected into the ambient with the help of thermal regulation mechanisms (thermal conductivity, convection, emittance and water evaporation (from skin and mucosal tunics)) via breathing (q_2), thermal insulation (clothing) (q_4) and unprotected parts of the human organism (q_3). Due to the ambient conditions and thermal resistance of the clothing, the said mechanisms add different percentage to the heat exchange (Fig. 3) [8].

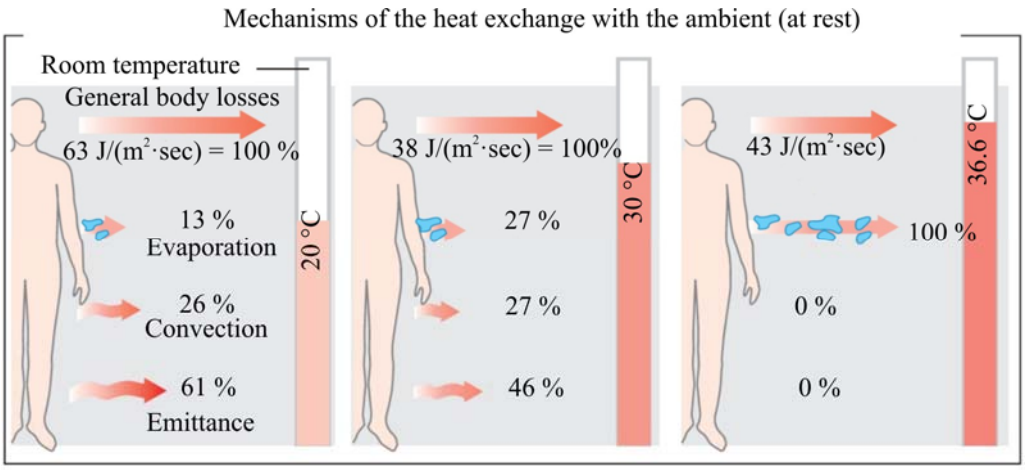

Fig. 3. Typical dependence of the correlation between human heat exchange mechanisms on the ambient temperature [7].

A vest with the TE conditioner 2 is put on the body wearing the underwear 3, through which the heat flux q_4 is transferred to the heat collector 9, and, subsequently, to TE modules 5. The part of the collector surface that is not covered with TE modules is thermally insulated 4, 8. The heat flux from the TE modules q_5 is rejected into the ambient via a metallic heat conducting plate 7 and fabric 6. It is clear that the heat resistance of the material of the vest influences the energy characteristics of the TE conditioner and thermal conditions inside it. Therefore, the computation of the TE conditioner energy characteristics due to the thermal resistance of the vest material and ambient conditions present a significant problem to solve.

Mathematical and computer models of a thermoelectric conditioner for a bullet-proof vest

The system of computation of TE conditioner energy characteristics as a function of physical model elements parameters is defined from the heat balance equation:

$$\begin{cases} Q_c = \chi_1 (T_7 - T_6) \\ Q_c = \chi_2 (T_6 - T_5) \end{cases}, \tag{1}$$

$$\begin{cases} Q_h = \chi_3 (T_3 - T_4), \\ Q_h = \chi_4 (T_2 - T_3), , \\ Q_h = hS(T_1 - T_2), \end{cases} \tag{2}$$

$$Q_h = Q_c + W_{TE}. \tag{3}$$

Here χ_1 is the thermal resistance of the vest material 6, χ_2 is the thermal resistance of the plate 7, χ_3 is the thermal resistance of the of the material 9, χ_4 is the thermal resistance of the material 3, Q_c is the cooling capacity of the TE conditioner, Q_h is its heating capacity, W_{TE} is the electric power of TE power supply 5, h is the heat-transfer coefficient, S is the area from which heat transfer is performed.

Taking into consideration (1) – (3), the following expression for the TE conditioner coefficient of performance (COP) is obtained:

$$\varepsilon = \frac{Q_c}{W_{TE}} = \frac{\alpha I (T_c + Q_c N_1) - 0.5 I^2 R - \lambda (T_h - T_c - (Q_h N_2 + Q_c N_1))}{W_{TE}}, \tag{4}$$

where $N_1 = \frac{(\chi_1 + \chi_2)}{\chi_1 \chi_2}$, $N_2 = \frac{(\chi_3 + \chi_4 + hS)}{\chi_3 \chi_4 hS}$, I – current strength, R – electric resistance, α – Seebeck coefficient of thermoelement, λ – thermal conductivity coefficient of thermoelement.

The heating coefficient for such a case will have the form of:

$$\mu = \frac{Q_h}{W_{TE}} = \frac{\alpha I(T_h + Q_h N_2) + 0.5 I^2 R - \lambda(T_h - T_c - (Q_h N_2 + Q_c N_1))}{W_{TE}}. \quad (5)$$

The computer methods of object-oriented simulation together with numeric methods for determination of the purpose-oriented functions, namely, COP and heating coefficient of the TE conditioner, were applied for computing in the present work. These functions are nonlinear and depend on the totality of parameters which are expressed implicitly with the help of the plurality of empiric equalities. Therefore, there exists no possibility of applying any methods of determining either the first or second order extremum (due to impossibility of the derivatives definition). To ensure the search for the optimal COP value, the non-gradient method of the zero order, namely, the modified Hooke-Jeeves method, was applied [9].

A system of non-linear equations (1 – 3) is being solved in each iteration of the main cycle of the programme, and cooling capacity is determined. The approximating polynoms coefficients which help determine the empirical correlations between the physical parameters of the optimization problem are computed in the programme. The details of the modelling technique are given in [10].

Simulation results

Hence, the initial parameters of the model are the following: thermal power to be rejected from a human body through TE modules, the power itself being the function of the ambient temperature (Fig. 3), and the organism physiological state (the value of human heat emittance of $Q = 100$ W is used that corresponds to the state of a human at rest); the ambient temperature of $T_1 = 20$, 30, 36.6, 40 ºC; the external surface area of the vest to provide heat-exchange of $S = 0.5$ m^2; *Bi-Te* TE heat converters parameters [11] are 20 × 20 mm with the crystal size of 2.0 × 2.0 × 1.5 mm and the number of TE modules being equal to 50 pcs.

As a result of modelling, the dependence of the electric power required for provision of the human body constant temperature ($T = 36.6$ ºC) on the ambient temperature and heat resistance of the vest materials (Fig. 4) was computed.

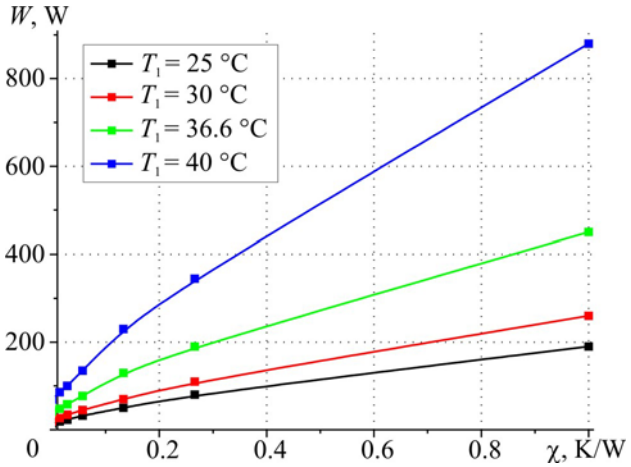

Fig. 4. Electric power of thermoelectric modules as a function of thermal resistance of the vest fabrics and for different ambient temperatures.

As it is evident from Fig. 4, the power required for provision of the human body constant temperature (T = 36.6 ºC) is strongly dependent on the heat resistance of the clothing fabric. For example, to supply the TE conditioner with the vest fabric heat resistance of about χ = 0.4 K/W, which corresponds to the use of cotton-based fabrics (thermal conductivity coefficient $\kappa \approx 0.05$ W/m·K) and at the ambient temperature of T_1 = 36.6 ºC, which corresponds to the human body surface normal temperature, the power of W = 250 W is required. If the thermal resistance of the vest is reduced fivefold, which corresponds to the use of the fabric with the increased thermal conductivity ($\kappa \approx 0.01$ W/m·K) [12], it leads to the increase in its efficiency by the factor of 2.5 and decrease in TE modules power down to W = 100 W.

However, from the research performed it is clear that the model of a TE conditioner with uniformly distributed modules for humans is not efficient enough and requires further improvements, especially by way of intensifying of the heat exchange by blowing with air fans, etc. Moreover, to diminish energy expenditures when using individual conditioners for humans, the search for and development of novel materials with the increased thermal conductivity remains essential.

Conclusions

1. The possibility of development of a thermoelectric conditioner for humans based on the model with the uniformly distributed modules was confirmed but its application is not efficient enough and requires further improvements. The dependence of the electric power needed for provision of the human body constant temperature (T = 36.6 ºC) on the ambient temperature and the vest fabric thermal resistance was computed.
2. The dependence of the electric power necessary for the human body constant temperature (T = 36.6 ºC) provision on the ambient temperature and the vest fabric thermal resistance was computed.
3. It was determined that the electric power of W = 250 W is required to supply the conditioner for humans at the thermal resistance of about χ = 0.4 K/W, which corresponds to the use of cotton-based fabric, whereas the ambient temperature is T_1 = 36.6 ºC.
4. If the thermal resistance of the vest is reduced f ivefold, which corresponds to the use of the fabric with the increased thermal conductivity ($\kappa \approx 0.01$ W/m·K) [11], it leads to the increase in its efficiency by the factor of 2.5.

References

1. S.V. Belov, A.V. Ilnitskaya, A.F. Kozyakov, et al, *Life Safety. College Textbook* (Moscow: Vysschaya, Shkola, 1999).
2. A.V. Prybyla, Physical Models of Personal Air-Conditioners (Part One), *J.Thermoelectricity* 1, 16 – 39 (2016).
3. L.I. Anatychuk, A.V. Prybyla, Comparative Analysis of Thermoelectric and Compression Heat Pumps for Individual Air-Conditioners, *J.Thermoelectricity* 2, 31 – 39 (2016).
4. *Pat. US 2010/0107657 A1*, Apparel with Heating and Cooling Capabilities, Kranthi K. Vistakula.- Pub. Date: May. 6, 2010.
5. *Pat. US 2002/0156509 A1*, Thermal Control Suit, John A. Baker.- Pub. Date: Oct. 24, 2002.
6. http://dhamainnovations.com.

7. N.K. Vitte, *Human Heat Exchange and Its Hygienic Importance* (Kyiv: Gosmedizdat, 1956), 148 p.
8. A. Despopoulos, S. Silbernagl, Color Atlas of Physiology (Stuttgart: Georg Thieme Verlag, 1986), 356 p.
9. V.M. Verzhbitsky, Numerical Methods (Linear Algebra and Nonlinear Equations): Manual for Higher Educational Institutions (Moscow: "Oniks 21 Century" Publ.House, 2005), 432 p.
10. L.I. Anatychuk, R.V. Kuz, and A.V. Prybyla, The Effect of Heat Exchange System on the Efficiency of Thermoelectric Air Conditioner, *J.Thermoelectricity* 1, 75 – 81 (2013).
11. http://www.ite.inst.cv.ua.
12. M.V. Nazarova, S.Yu. Boiko, Study of Cold-Resisting Properties of Terry-Pile Two Ply Fabric, *Sovremennye Problemy Nauki i Obrazovaniya* 5, 113 – 117 (2009).

Submitted 05.09.2016

L.I. Anatychuk[1,2], V.Ya. Mykhailovsky[1], M.V. Maksymuk[1], I.S. Andrusiak[1,2]

[1]Institute of Thermoelectricity of the NAS and MES of Ukraine,
1, Nauky Str., Chernivtsi, 58029, Ukraine;
[2]Yu.Fedkovych Chernivtsi National University
2, Kotsyubinsky str., Chernivtsi, 58012 Ukraine

EXPERIMENTAL RESEARCH ON THERMOELECTRIC AUTOMOBILE STARTING PRE-HEATER OPERATED WITH DIESEL FUEL

The results of experimental research on the energy characteristics of 75 – 90 W thermoelectric automobile heater operated with diesel fuel for start heating of engine under low ambient temperatures are presented.

Key words: starting pre-heater, thermoelectric generator.

Introduction

Today the problem of internal combustion engines start-up under low ambient temperatures is solved by using starting pre-heaters commercially produced by a number of companies – Eberspecher, Webasto, Truma (Germany), Ateso (Czeck Republic), Teplostar (Russia), Mikuni (Japan). Such heaters run on different fuels and are used in the cars, trucks, buses, yachts and boats.

Many years' experience of vehicles operation shows that start heating not only assures reliable engine start, but also allows increasing its service life by 50 – 60 thousand kilometers per year and reducing toxic discharge by a factor of 5, while saving 90 – 150 l of fuel during one winter season. Moreover, comfortable conditions provided by start heating eliminate completely the possibility of accident due to cold impact on the driver [1].

However, despite ample opportunities, starting pre-heaters have not found mass application yet. One of the main reasons for this is electric energy requirement for power supply to heater components, namely fuel pump, fan for air delivery to combustion chamber, circulation pump for liquid heat carrier pumping. Preliminary investigations have shown that during operation of liquid heater of thermal power 4 kW and electric power requirement 40 W, a battery of capacity 60 A·hour within 4.5 hours loses 50 % of capacity. This causes battery discharge and creates significant difficulties at engine start. To avoid battery discharge during start heating, it is reasonable to use thermoelectric generator as a source of electricity for such heaters [2 – 4].

In [5], analysis of technical characteristics of starting pre-heaters for various transport means is made and electrical parameters of thermal generators are determined which are necessary for autonomous operation of such heaters and additional power supply to other automobile equipment, including re-charging of batteries.

Based on computer calculations performed in [6], a sample of thermoelectric heater operated with diesel fuel of electric power output 70 – 90 W has been created at the Institute of Thermoelectricity for start heating of transport means with engine displacement up to 4 l.

The purpose of this work is to study thermal and electrical characteristics of the developed heater design and to test its operation in the automobile.

Structure and operating principle of thermoelectric starting pre-heater

Fig. 1 shows a layout of an automobile starting pre-heater with a thermoelectric power supply.

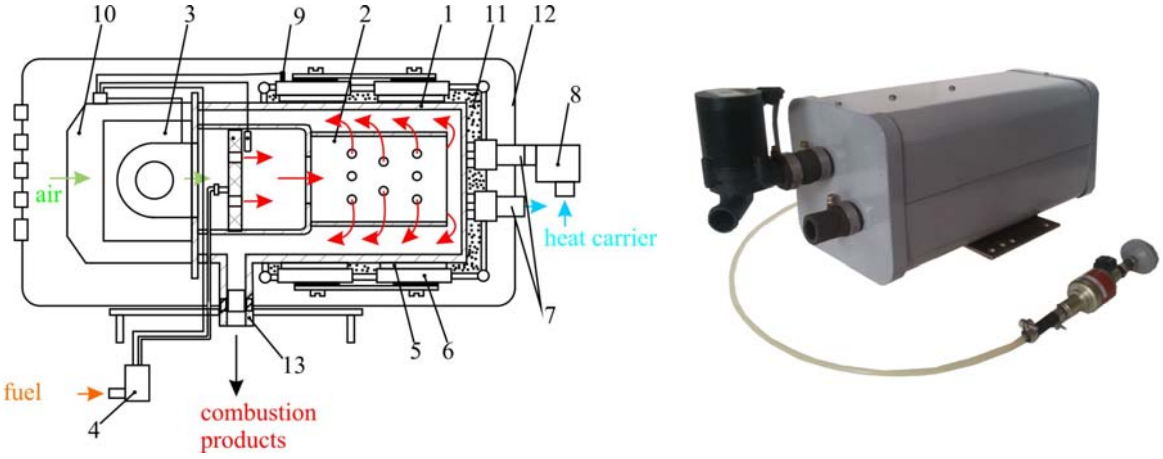

a) *б)*

Fig. 1. Layout (a) and exterior view (b) of an automobile starting pre-heater with a thermoelectric power supply: 1 – hot heat exchanger; 2 – source of heat; 3 – fan; 4 – fuel pump; 5 – thermoelectric pile; 6 – cold heat exchanger; 7 – input and output connecting pipes; 8 – circulating pump; 9 – overheat sensor; 10 – electronic unit; 11 – thermal insulation; 12 – case; 13 – exhaust pipe.

This thermoelectric heater is composed of a hot side heat exchanger **1**, which holds the source of heat **2** in its interior space. Fuel and air delivery to the source of heat is carried out by a fan **3** and fuel pump **4**. A thermoelectric pile **5** is located on the exterior surface of the hot heat exchanger the heat from which is removed by heat exchangers **6**.

Cold heat exchangers are combined into one hydraulic loop connected to the engine cooling system by the connecting pipes **7**. Circulation of the liquid heat carrier in the "heater-engine" loop is realized with the circulating pump **8**. An overheat sensor **9** is located on one of the cold heat exchangers to control the temperature of the heat carrier.

The start-up and operation control of all heater devices (fan, fuel and circulating pumps) is done by an electronic unit **10**.

Free space between the hot and cold heat exchangers is filled up with thermal insulation **11**. An automobile heater with a fan, electronic unit, heat exchangers and thermoelectric pile is placed within a case **12**. The end products of the fuel combustion are released by an exhaust pipe **13** into the environment.

A thermoelectric pile is composed of 12 standard generator modules ALTEC-1061 [7] which are electrically connected in series/in parallel. Modules connection was adjusted so that the output voltage of the heater matched the voltage of the automotive storage battery.

A diesel burner Ersatzbrenner D TT-C MB was used as a source of heat in the structure of the heater, pulse pump BTL.DP30.02.12V DAEMPFLER E-TEIL and liquid pump 12V U4847 TT C/E of the starting pre-heater "Thermo Top Evo 4» (Webasto) [8]" were used as fuel and circulating pumps.

The heater works as follows. Thermal energy from fuel combustion heats up the hot heat exchanger, passes through the thermoelectric converter and is diverted by the liquid heat carrier circulating in the heat exchangers of the heater and engine cooling system. Due to the temperature difference between the hot and cold sides, the thermal converter generates electric current. Therefore, thermal energy diverted from the thermal converter is used for the engine warm-up and heating of the car interior, while electric power is used to supply heater components and recharge the automobile storage battery.

Test stand for thermoelectric heater analysis

The analysis of energy characteristics of the designed thermoelectric diesel heater was made on test stands, the layout of which is shown in Fig. 2 and 3.

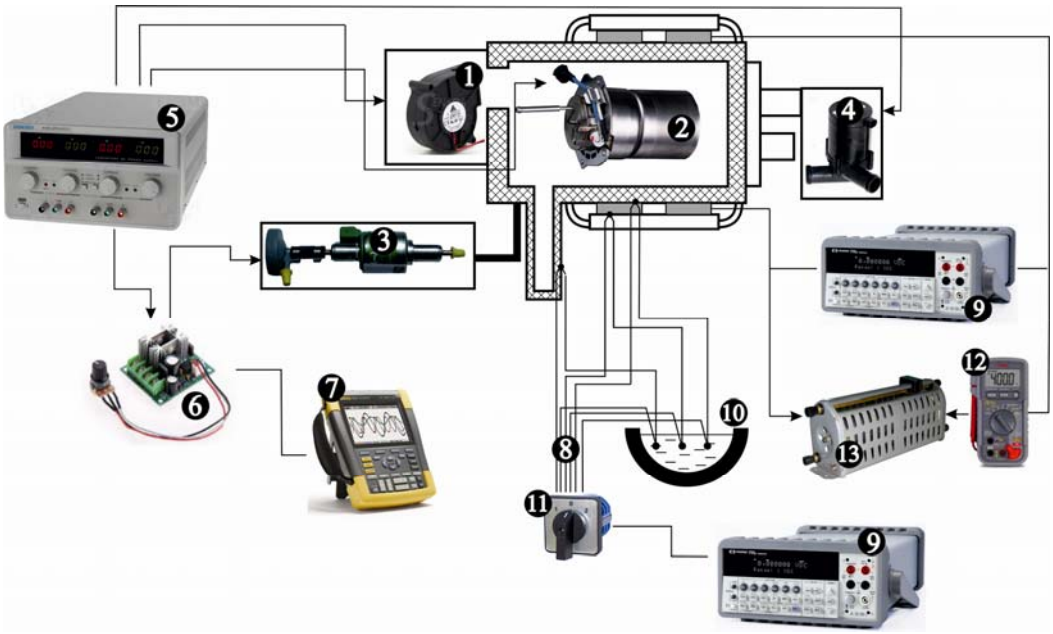

Fig. 2. Layout of test stand №1: 1 – air fan; 2 – diesel burner; 3 – fuel pump; 4 – circulating pump; 5 – electronic control unit; 6 – pulse controller; 7 – oscillograph; 8 – thermocouples; 9 – multimeter; 10 – Dewar flask with ice; 11 – rotary switch; 12 – digital ammeter; 13 – rheostat.

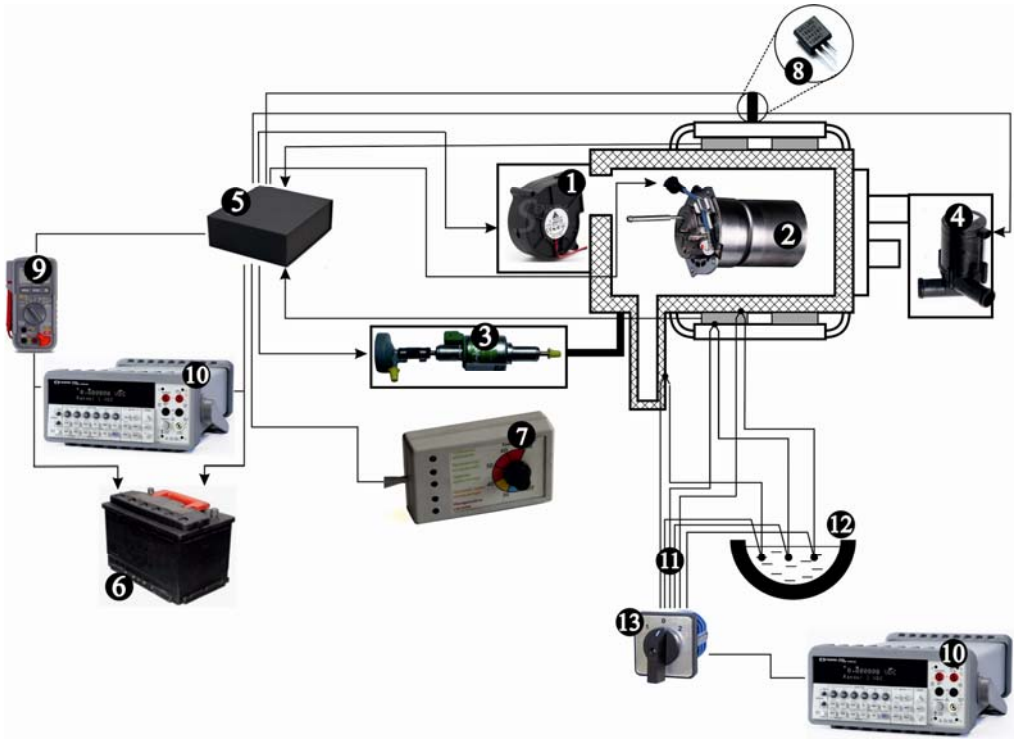

Fig. 3. Layout of the test stand №2: 1 – air fan; 2 – diesel burner; 3 – fuel pump; 4 – circulating pump 5 – electronic control unit; 6 – storage battery; 7 – control panel; 8 – overheat sensor; 9 – digital ammeter; 10 – multimeter; 11 – thermocouples; 12 – Dewar flask with ice; 13 – switch.

Power supply of components (air fan **1**, spark plug of diesel burner **2**, fuel pump **3**, circulating pump **4)** was done from a separate power source to obtain the optimum performance of the heater, improve the algorithm of its start-up and reach the maximum power. Fuel consumption was adjusted by the pulse controller **6** measuring the pulse period with the oscillograph **7**. Temperatures on the hot and cold heat exchangers, as well as the temperature of the gas at the outlet of the exhaust pipe, were measured by differential thermocouples **8**. External load was set by the rheostat **13** removing the voltage and electrical current from thermoelectric modules.

The testing of the thermoelectric heater paired up with the automobile battery was performed on the test stand No.2 (Fig. 3). In this case, the operation of components was not controlled manually by power supply units, but by the electronic control unit **5**.

The storage battery charge level was determined by determining the electric current in the "storage battery - generator" system and the storage battery voltage. The heat carrier temperature was set in the control panel **7** and the set temperature was controlled by the overheat sensor **8**.

The heat removal system of the heater was combined in one hydraulic loop with the thermostat to estimate the heating velocity of the heat carrier.

Test stand results

The research results of the parameters of the automobile starting pre-heater and thermoelectric generator are shown in Fig. 4.

The presented data show that within two hours of the heater operation the cold heat carrier, in this case it is water, is heated to 70 °C (the heat carrier temperature was considered to be equal to the temperature of the cold heat exchanger T_{cold}). In so doing, after 20 minutes of operation the temperatures of the hot heat exchanger T_{hot} and exhaust gases T_{gas} are at 280 °C and 300 °C and do not vary afterwards, therefore the generator reaches the stationary mode. Under such circumstances, the electrical voltage U of the thermoelectric converter under maximum power conditions is within 13 – 12 V at T_{cold} = 30 – 70 °C.

The stationary mode of the heater (mode IV) is sustained when the heat power of the heat source Q is 2.3 kW and the cold heat carrier consumption g_T = 0.3 m^3/hour. However, for the reliable start and steady operation of the heater in the electronic control unit, the gradual increase of heat power of the burner and aerofuel mixture was implemented (Table).

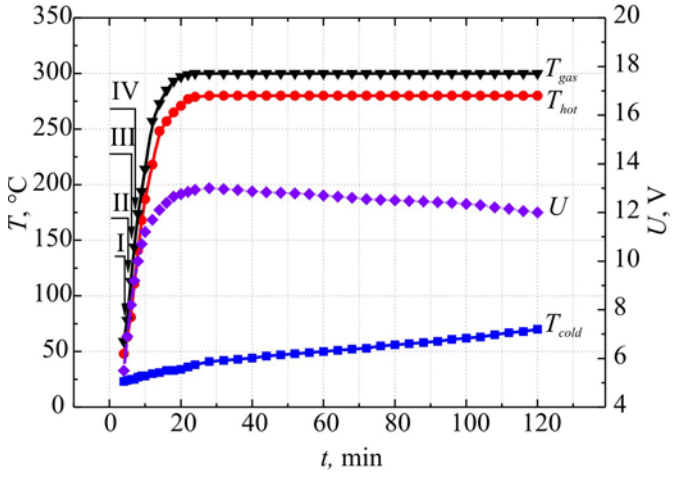

Fig. 4. Temperature dependence of cold T_{cold}, hot heat exchangers T_{hot}, combustion products T_{gas} and output electric voltage U of the heater on the operation time.

Table

Operating mode of thermoelectric starting pre-heater

Mode	Heat power Q, W	Fuel consumption g_n, g/hour	Air consumption g_{air}, m^3/hour	Heat carrier consumption g_T, m^3/hour
I	935	79	3.26	0.3
II	1190	100	3.5	
III	1570	132	3.65	
IV	2330	195	4.57	

Note that further increment of the burner heat power leads to overheating of the hot side of the modules (T_p ~ 350 °C) and therefore such modes are not used for the heater operation.

Fig. 5 shows dependencies of the maximum electric power P and coefficient of efficiency η of the heater on the temperature of the cold heat carrier.

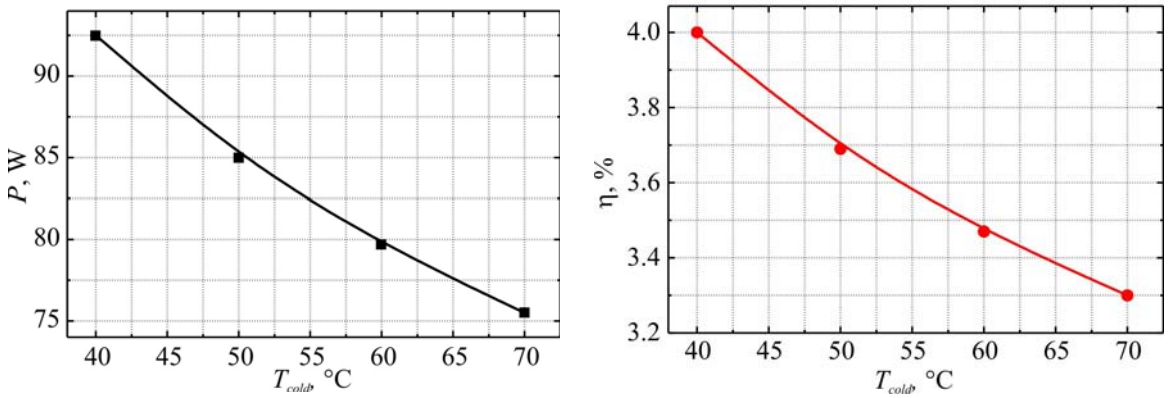

a) *b)*

Fig. 5. Dependence of maximum electric power P (a) and coefficient of efficiency η (b) on the temperature of the cold heat carrier.

From Fig. 5 it follows that the output electric power of the thermoelectric starting pre-heater is 90 to75 W within the temperature range of the circulating heat carrier 40 – 70 °C. The efficiency of thermoelectric conversion comes to 4 % at T_{cold} = 40 °C and decreases to 3.3 % at T_{cold} = 70 °C as the heat carrier warms up.

The research results of the operation of the thermoelectric starting pre-heater paired with the automobile storage battery are shown in Fig. 6.

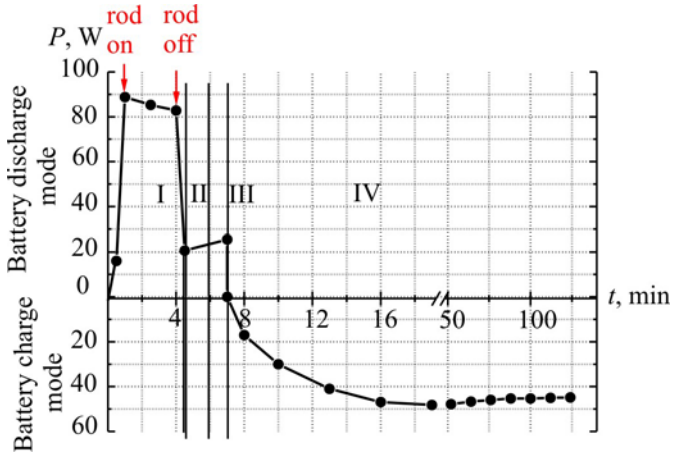

Fig. 6. Dependence of charge and discharge power of storage battery on the time of thermoelectric heater operation. Roman numerals denote the modes of heater operation (Tabl.).

As shown in Fig. 6, after the heater start-up the supply of its components is done with the storage battery (0 – 7 minutes). At the same time, 15 – 25 W is used for the circulating pump, fuel pump and fan depending on the operating mode and 60 – 70 W for the burner spark plug supply. The discharge mode of the storage battery lasts until the time when the output power of the generator is equal to the consumed power of the components. Afterwards, the electronic control unit cuts off supply of the components from the storage battery and the heater switches to off-line mode. With the increase of the output electric power of the generator, the electronic unit reroutes the excess of the electric energy to charge the storage battery (7 – 120 minutes). Data presented in Fig. 6 show that the maximum power used for charging is 50 W and thereafter decreases slightly to 45 W due to the cold heat carrier warming-up.

Observation results made in automobile

The layout of the heater connection to the hydraulic loop of the automobile is shown in Fig. 7.

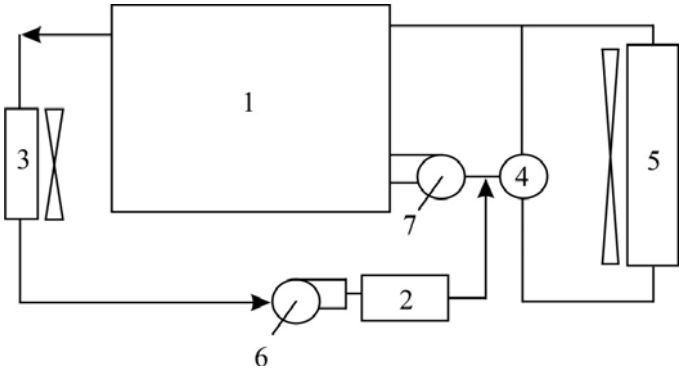

Fig. 7. Layout of the heater connection to the hydraulic loop of the automobile:
1 – engine; 2 – thermoelectric heater; 3 – furnace; 4 – thermostat; 5 – radiator;
6 – circulating pump of heater; 7 – standard pump of automobile.

It is advisable to place the thermoelectric heater **2** in the hydraulic loop of the automobile between the engine **1** and furnace **3** in such a way that the liquid heat carrier which moves along the minor cooling circuit ("engine-furnace-standard pump) reached the engine entry upon exiting the heater.

The operation of the thermoelectric starting pre-heater was analyzed in a "Mercedes" automobile with the engine volume of 2.8 liters (Fig. 8).

Fig. 8. Thermoelectric starting preheater in the
"Mercedes" automobile.

Diesel fuel was delivered to the heater from the separate tank located with the fuel pump in the trunk of the automobile (Fig. 9*a*). The fuel pump was connected to the heater mounted under the automobile hood with the electricity cable and fuel pipe (Fig. 9*b*).

a) *b)*

Fig. 9. Location of fuel tank and fuel pump (a), electricity cables and fuel pipe (b).

The results of the experimental analysis of the starting pre-heater in the automobile are presented in Fig. 10.

The data above show that the thermoelectric heater provides the engine pre-heating up to 50 °C within the time of its operation (Fig. 10*a*), even if the temperature is nonoptimal, it is sufficient for the automobile start-up. Turning on the standard heating system leads to the engine temperature fall T_{engine} down to 30 °C and the car interior temperature rise $T_{car\ interior}$ up to 10 °C (Fig. 10*b*). Under such conditions, the amount of fuel m_{fuel} used by the heater is ~ 400 g in both cases.

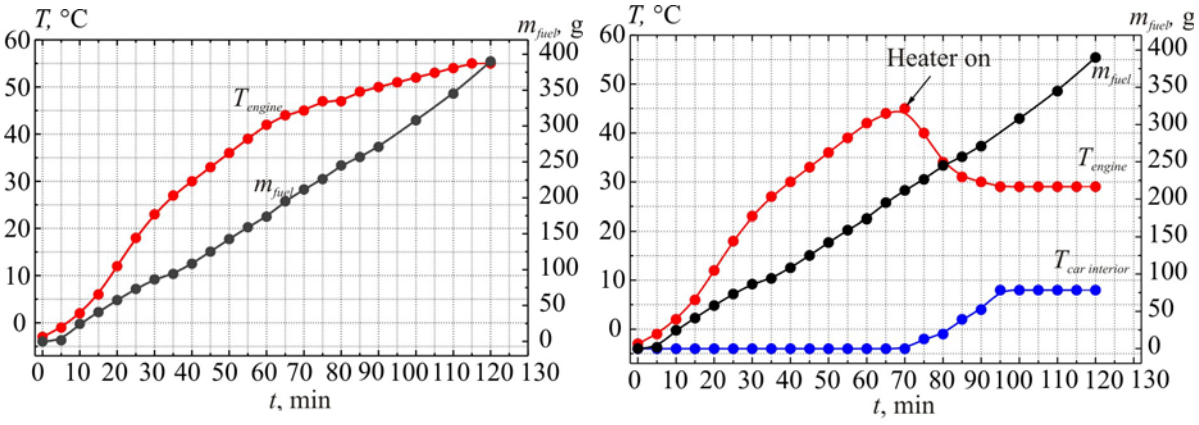

a) *б)*

Fig. 10. Results of experimental investigations of thermoelectric heater in the automobile: a) engine preheating; b) engine pre-heating and car interior heating. Ambient temperature T_o = – 5 °C.

The storage battery charging mode (Fig. 11) was turned on on the 7th minute of the heater operation, while the charging rate I reached its peak 1.9 A on the 20th minute of operation and actually did not change afterwards. At the same time, the voltage level of the storage battery $U_{battery}$ was 13 V from the moment the heater reached its off-line operation mode until the fan of the standard heating system turns on, whereupon it declined rapidly to 12 V.

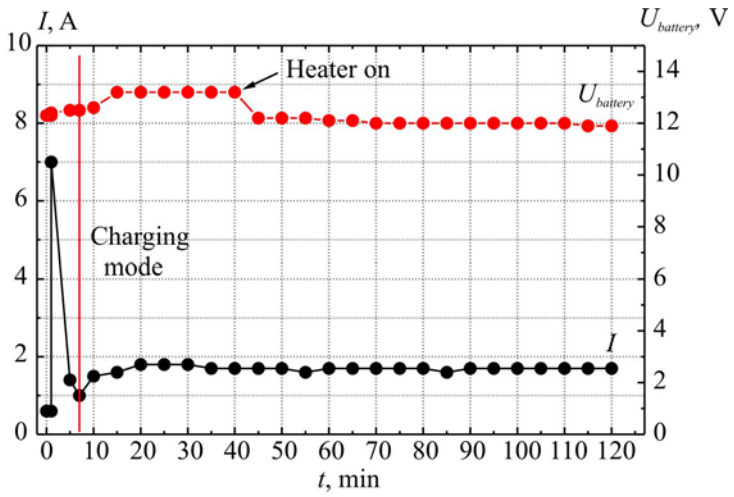

Fig. 11. Dependence of storage battery voltage and charging rate on the time of heater operation.

Thus, within the period of the heater operation in the automobile, the excess of the electric power of the thermal generator used for recharging storage battery is 20 – 25 W.

It should be noted that such discrepancy in the automobile measurement results and test units (Fig. 6) was due to the fact that the storage batteries were charged differently in both cases. Therefore, the charging rate shall be determined first and foremost by the storage battery charge level in each individual case [9].

Similar research aimed at the determination of the fuel consumption, car interior and engine temperatures was performed when the engine was warmed-up at idle. The results of these measurements are shown in Fig. 12.

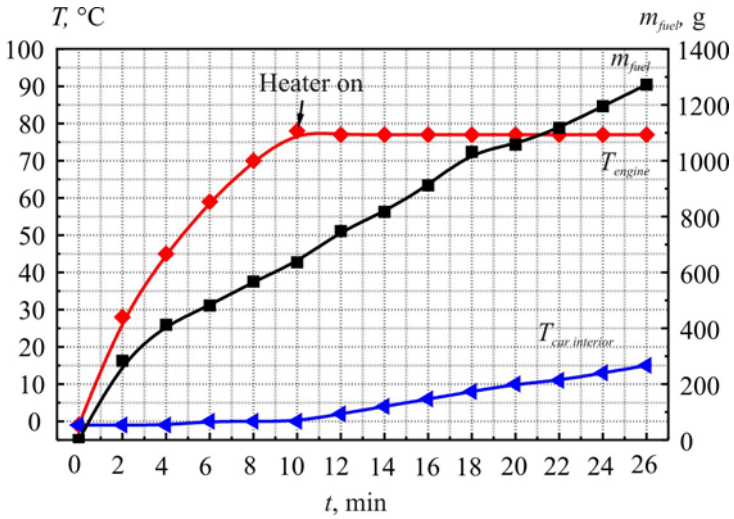

Fig. 12. Results of experimental investigations of automobile warm-up at idle. Ambient temperature T_o = – 5 °C.

As compared with the warming-up by the thermoelectric heater, the idle running provides optimal engine temperature 80 °C for the automobile start-up on the 10th minute of operation and allows the car interior temperature to rise to 15 °C. But in this case, the burned fuel mass m_{fuel} is 700 g at the moment when the standard heating system switches on, which is nearly twice as large as the consumed fuel at the pre-start heating.

Therefore, considering that in average an automobile does 4 cold starts per day during only one winter season (90 – 110 days), the diesel fuel saving for the automobile with the engine volume of 2.8 liters shall be 120 – 150 litres (~ 40 %).

Conclusions

1. It is established that the output electric power of the developed thermoelectric starting pre-heater is 75 – 90 W at the hot heat exchanger temperature 280 °C and cold heat carrier temperature within 70 – 40 °C. The maximum efficiency of the generator is 4 % under such conditions.
2. It is stated that the maximum power mode of the heater is reached when the heat power of the heat source is 2.3 kW, fuel consumption 195 g/hour and air consumption 4.57 m^3/hour. Meanwhile, the cold heat carrier consumption is 0.3 m^3/hour.
3. It is established that nearly 90 W of the storage battery electric power is used to supply the heater components. When the heater switches to off-line mode, the electronic control unit cuts off the supply of the components from the storage battery and with the increase of the output electric power of the generator reroutes the excess of the electric energy to charge the storage battery. Meanwhile, the charging rate is determined by the individual storage battery charge level.
4. It is established that the thermoelectric heater provides the automobile engine pre-heating up to 50 °C within two hours of operation. Switching on the standard heating system of the automobile leads to decrease of the engine temperature to 30 °C, whereas the car interior temperature increases to 10 °C.
5. It is shown that the application of the thermoelectric starting pre-heater in automobiles with engine volume of 2.8 liters allows saving fuel by ~ 40 % during only one winter season as compared with warming-up at idle.

References

1. V.S. Naiman, *All about Starting Pre-Heaters* (Moscow: ACT, 2007), p. 213.
2. V.Ya. Mykhailovsky, M.V. Maksymuk, Automobile Operating Conditions at Low Temperatures. The Necessity of Applying Heaters and the Rationality of Using Thermal Generators for their Operation, *J.Thermoelectricity* 3, 20 – 31 (2014).
3. *Patent UA № 72304*, InCl: F01N 5/00; H01L35/00. Automobile Heater with Thermoelectric Power Source /L.I. Anatychuk, V.Ya. Mykhailovsky. Publ.10.08.2012, Bul. № 15, Application u2012 02055 of 23.02.2012.
4. *Patent UA for Invention № 102303*, InCl F01N 5/00 H01L 35/00. Thermoelectric Power Source for Automobile / L.I. Anatychuk, V.Ya. Mykhailovsky. Publ. 25.06.2013, Bul. № 12, Application u2011 13957 of 28.11.2011.
5. V.Ya. Mykhailovsky, M.V. Maksymuk, Rational Powers of Thermal Generators for Starting Pre-Heaters of Vehicles, *J.Thermoelectricity* 4, 69 – 77 (2015).

6. V.Ya. Mykhailovsky, M.V. Maksymuk, Computer Design of Thermoelectric Automobile Starting Pre-Heater Operated with Diese Fuel, *J.Thermoelectricity* 1, 52 – 66 (2016).
7. http://www.inst.cv.ua.
8. http://www.webasto.com.ua.
9. Yu.I. Bubnov, S.B. Orlov, *Hermetically Sealed Chemical Sources of Current: Cells and Storages, Testing and Operation Equipment, Reference Book* (Saint-Petersburg, KHIMIZDAT, 2005).

Submitted 16.08.2016

ARTICLE PREPARATION RULES

The article shall conform to the journal profile. The article content shall be legible, concise and have no repetitions.

The article shall be submitted to the editorial board in electronic version.

The text shall be typed in text editor not lower than MS Word 6.0/7.0.

Page setup: "mirror margins"- top margin – 2.5 cm, bottom margin – 2.0 cm, inside – 2.0 cm, outside– 3.0 cm, from the edge to page header – 1.27 cm, page footer – 1.27 cm.

Graphic materials, pictures shall be submitted in color or, as an exception, black and white, in .opj or .cdr formats, .jpg or .tif formats being also permissible. According to author's choice, the tables and partially the text can be also in color.

The article shall be submitted in English on A4 paper sheets; the number of pages shall not exceed 12. By agreement with the editorial board, the number of pages can be increased.

To accelerate publication of the article, please adhere to the following rules:

- the authors' initials and names are arranged in the centre of the first page at the distance of 1 cm from the page header, font Times New Roman, size 12 pt, line spacing 1.2;
- the name of organization, address (street, city, postal code, country) – indent 1 cm below the authors' initials and names, font Times New Roman, size 11 pt, line spacing 1.2, center alignment;
- the title of the article is arranged 1 cm below the name of organization, in capital letters, semi-bold, font New Roman, size 12 pt, line spacing 1.2, center alignment. The title of the article shall be concrete and possibly concise;
- the abstract is arranged 1 cm below the title of the article, font Times New Roman, size 10 pt, in italics, line spacing 1.2 ,center alignment;
- key words are arranged below the abstract, font Times New Roman, size 10 pt, line spacing 1.2, justified alignment. The title "Key words" – font Times New Roman, size 10 pt, semi-bold;
- the main text of the article is arranged 1 cm below the abstract, indent 1 cm, font Times New Roman. size 11 pt, line spacing 1.2, justified alignment;
- formulae are typed in formula editor, fonts Symbol, Times New Roman. Font size is "normal" – 12 pt, "large index" – 7 pt, "small index" – 5 pt, "large symbol" – 18 pt, "small symbol" – 12 pt). The formula is arranged in the text, centre aligned and shall not occupy more than 5/6 of the line width, formulae are numbered in round brackets right;
- dimensions of all quantities used in the article are represented in the International System of Units (SI) with the explication of the symbols employed;
- figures are arranged in the text. The figures and pictures shall be clear and contrast; the plot axes – parallel to sheet edges, thus eliminating possible displacement of angles in scaling;
- tables are arranged in the text. The width of the table shall be 1 cm less than the line width. Above the table its ordinary number is indicated, right alignment. Continuous table numbering throughout the text. The title of the table is arranged below its number, center alignment;
- references should appear at the end of the manuscript. References within the text should be enclosed in square brackets. References should be numbered in order of first appearance in the text. Examples of various reference types are given below.

– L.I. Anatychuk, *Thermoelements and Thermoelectric Devices: Handbook* (Kyiv: Naukova Dumka, 1979), p.766. (Book)
– T.M. Tritt, Thermoelectric Phenomena, Materials, and Applications, *Annual Review of Materials Research* **41**, 433 (2011). (Journal paper)
– U. Ghoshal, *Proceedings of the XXI International Conference on Thermoelectrics* (N.Y., USA, 2002), p. 540. (Proceedings Conference)

The article should be supplemented by:

• letter from the organization where the work was performed or from the authors of the work applying for the publication of the article;

• information on the author (authors): last name and initials; full name and postal address of the institution where the author works; academic degree; position; telephone number; E-mail;

• author's (authors') photo in color or, as an exception, in black and white. With the number of authors more than two their photos are not given;

• author's application to the following effect:

We, the undersigned authors, … transfer to the founders and editors of "Journal of Thermoelectricity" the right to publish the article…in Ukrainian, Russian and English. This is to confirm that the present publication does not violate the copyright of other persons or organizations.

Date Signatures